3-D ADAPTIVE EULERIAN-LAGRANGIAN METHOD FOR MULTIPHASE FLOWS WITH SPACECRAFT APPLICATIONS

by

Jaeheon Sim

A dissertation submitted in partial fulfillment
of the requirements for the degree of
Doctor of Philosophy
(Aerospace Engineering)
in The University of Michigan
2010

Doctoral Committee:

Professor Wei Shyy, Chair
Professor Steven L. Ceccio
Professor Elaine S. Oran
Professor Kenneth G. Powell

DEDICATION

I dedicate this dissertation to my parents.

ACKNOWLEDGEMENTS

First of all, I would like to express my sincere gratitude to my adviser Prof. Wei Shyy for his guidance and encouragement. I could not thank him more. He has been so patient and gave me endless support and belief through my doctoral years. I appreciate his showing me the way in my life as well as in academia.

I would also like to thank Prof. Steven L. Ceccio, Prof. Elaine S. Oran, and Prof. Kenneth G. Powell for their valuable advice and for accepting being the member of my dissertation committee. I also deeply appreciate the warm support from Prof. Youngbin Yoon and Prof. In-Seuck Jeung in Korea.

It has been a great pleasure to be with my research group members, Aerowarriers members, and ksag.ae members and their families here at Ann Arbor. They stimulated interest in my research and helped me to stand up when I was in need.

Finally, I thank my parents. They have been behind me all the way and always inspired me with courage. Without their unconditional support, I could not start my doctoral study. This dissertation is gratefully dedicated to my parents.

TABLE OF CONTENTS

LIST OF FIGURES

LIST OF TABLES

ABSTRACT

3-D ADAPTIVE EULERIAN-LAGRANGIAN METHOD FOR MULTIPHASE FLOWS WITH SPACECRAFT APPLICATIONS

by

Jaeheon Sim

Chair: Wei Shyy

Understanding interfacial dynamics and fluid physics is important in many engineering applications, including spacecraft. Under microgravity, the moving boundaries and associated interfacial transport processes significantly impact the vehicle dynamics, design, and missions. However, it is difficult to mimic the micro-gravity condition experimentally. Numerical simulations of such problems are also challenging due to multiple time/length scales, large variations in fluid properties, moving boundaries, and phase changes.

A 3-D adaptive Eulerian-Lagrangian method is implemented for multiphase flow computations. The stationary (Eulerian) Cartesian grid is used to resolve the flow field, and the marker-based triangulated moving (Lagrangian) surface meshes are utilized to treat the phase boundaries. A main focus of the present study is to treat both fluid and solid phase boundaries in a unified framework with a contact line force model and a phase change model. The fluid interfaces are modeled using a continuous interface method which smoothes both the variations in material properties and the influences of

surface tension. The solid boundaries are treated by a ghost cell-based sharp interface method. A dynamic contact line force model is applied to calculate the position and movement of the solid-fluid-fluid interface. The energy and mass transfer due to phase change is computed using Stefan condition across the interfaces. A multi-level adaptive grid method is devised so that different length scales of the flow field can be resolved effectively.

Selected studies on the interfacial dynamics relevant to spacecraft fuel delivery applications are conducted and assessed with experimental measurements and scaling analysis. For liquid fuel draining under microgravity, depending on the relative influence between capillary force and inertia force, three different flow regimes are observed and liquid residuals are measured. The liquid fuel sloshing under varying acceleration results in a large shift in its center of mass and significant influence on the vehicle dynamics. For thrust oscillation studies, the liquid surface stability under vertically oscillating acceleration is investigated, and the threshold acceleration is correlated with the forcing frequency, surface tension, and viscosity. For thermo-fluid transport computations with phase changes, validation studies are conducted with natural convection flows, Stefan problems, and melting processes by convection/diffusion flows.

CHAPTER 1

INTRODUCTION

1.1 Motivation and Goals

Space missions – including rocket launchers, the space stations, and interplanetary space flights – require an understanding and managing of the cryogenic liquid dynamics under micro-gravity conditions. This understanding is crucial because cryogenic liquid dynamics under micro-gravity conditions have a significant impact on the engine operation, vehicle dynamics, spacecraft design, and even the overall mission. However, the limitation of experimental facility, especially short experimental time, makes experimental studies under micro-gravity difficult to perform. Figure 1.1 shows examples of zero-gravity facilities with a few seconds operational time on the ground. Furthermore, numerical simulations of such problems are also challenging due to multiple time/length scales, large variations in fluid properties, moving boundaries, and phase changes.

In this dissertation, a 3-D adaptive Eulerian-Lagrangian method is developed for complex multiphase flow computation with spacecraft applications. A main focus of the present study is to treat both fluid and solid phase boundaries in a unified framework with a contact line force model and a phase change model. Spacecraft fuel tank dynamics and fluid physics related to liquid fuel draining, sloshing, and surface stability are studied.

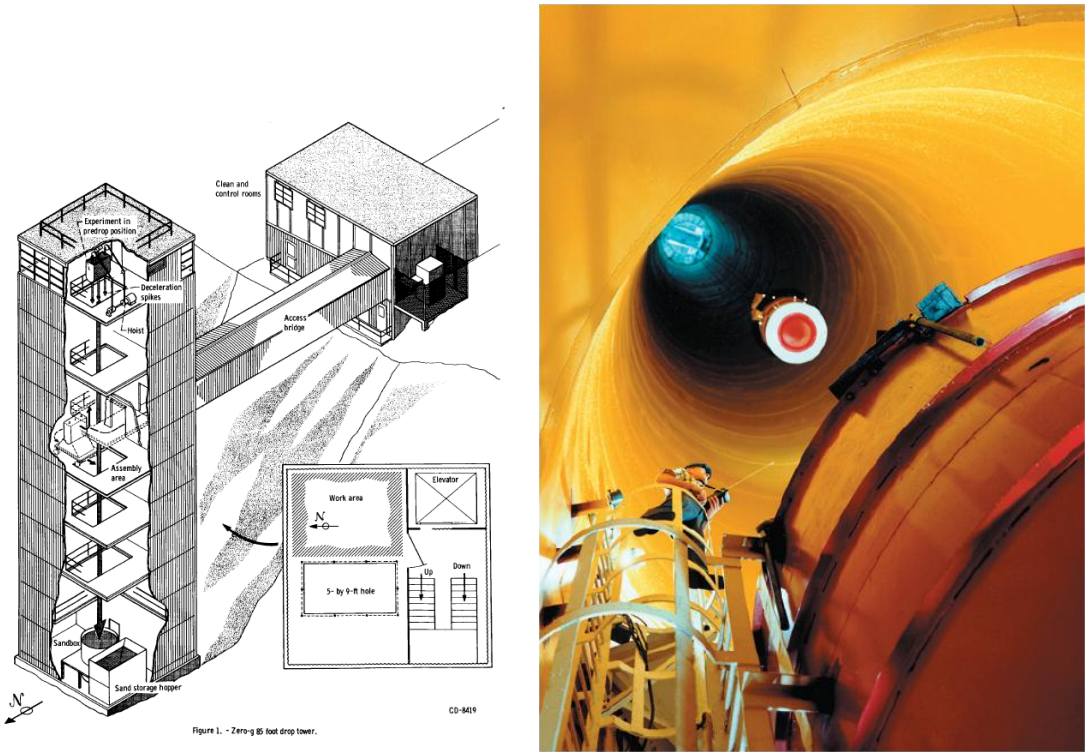

(a) **(b)**

Figure 1.1: Examples of zero-gravity research facilities on the ground. (a) 2.25 sec drop tower at the NASA Lewis zero-gravity research facility (Derdul *et al.* 1966). (b) 5.18 sec drop tower at the NASA Glen zero-gravity research facility.

1.2 Spacecraft Liquid Fuel Tank Dynamics Overview

When designing and operating a spacecraft, the dynamics and management of the cryogenic propellants is a major concern. The unoriented draining and sloshing motion under microgravity has a critical impact on the vehicle dynamics due to the shift in its center of mass. The variation of the amount of fuel delivered to the combustion chamber may result in engine operation failure and, consequently, in a mission failure. Furthermore, the thermal effect in a cryogenic propellant has huge influence on the spacecraft safety as well as fuel dynamics. Even a small amount of heat leaked from the incident solar radiation, the aerodynamics heating, or the spacecraft structure causes thermal stratification and fuel vaporization. This occurs because the boiling temperature of the cryogenic propellant is extremely low, and the space mission usually takes a long time. The fuel vaporization results in cryogenic propellant loss and self-pressurization in a fuel tank, and this determines the operational time and design safety of the fuel tank. Figure 1.2 illustrates these various phenomena related to liquid fuel dynamics in a spacecraft.

Contrary to the behavior of fluid on the ground, the fuel draining process under microgravity conditions can cause unexpected large interface distortion and slosh waves, resulting in fast vapor ingestion and large liquid residuals. Figure 1.3 shows an example of liquid fuel draining experiment at the micro-gravity facility, where large interface distortions is observed, and it may results in large liquid residuals at the moment of vapor ingestion.

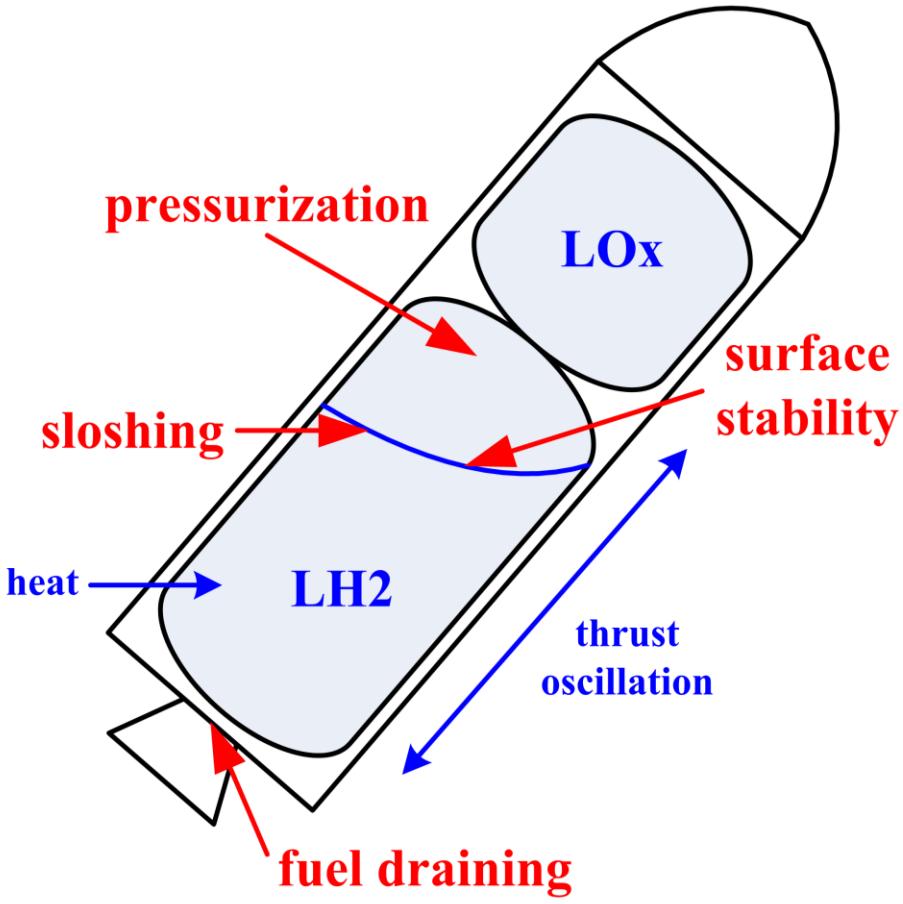

Figure 1.2: Illustration of spacecraft liquid fuel tank dynamics; fuel draining, sloshing, surface stability, and self-pressurization.

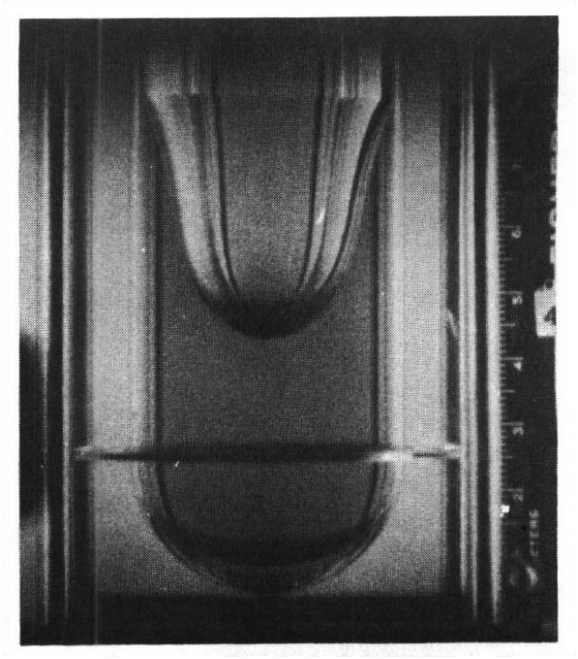

Figure 1.3: An example of liquid fuel draining experiment at the 2.25 sec micro-gravity facility of the NASA Lewis research center (Derdul *et al.* 1966). A huge interface distortion is observed and large amount of liquid fuel may not be used effectively due to the unoriented draining and vapor ingestion.

Petrash *et al*. experimentally studied the effect of weightlessness on the liquid-vapor interface in a spherical tank without draining (Petrash *et al.* 1962; Petrash *et al.* 1963). Various drop tower tests on the draining process under microgravity followed. They found that the shape of the tank bottom and the position of the outlet have little influence on the draining process while the pressuring gas diffuser and outlet baffle minimize the interface distortion (Derdul *et al.* 1966; Nussle *et al.* 1965). Typically, the Froude number, the ratio of inertia to gravitational forces, is correlated with the draining phenomena under normal gravity (Berenyi and Abdalla 1970). However, the Froude number has diminished influence on the draining process under microgravity; instead, the Weber number, which measures the ratio of inertia to surface tension forces, is found to

have a stronger influence on the draining procedure in weightlessness (Berenyi and Abdalla 1970; Derdul *et al.* 1966). Symons defined a draining parameter by grouping the Weber number and the Froude number to cover phenomena ranging from micro to normal gravity conditions, and he categorized three different draining flow regimes according to the flow characteristics of the draining process (Symons 1978).

Liquid propellant sloshing motion is another primary concern in a spacecraft since the movement of mass distribution imposes disturbances on the vehicle controls and interrupts engine operations. Under high acceleration, the sloshing motions are suppressed and are of no concern. However, low gravity orbital missions require accurate predictions and controls of propellants. For the Saturn V earth orbital flight prior to the lunar missions of the 1960's, Toole and Hastings conducted scale model ground experiments at the 4.3 sec drop tower facility at the NASA Marshall space flight center, in order to understand the behavior of a sloshing liquid subjected to a sudden reduction in acceleration (Toole and Hastings 1968). Engine shutdown converts the large potential energy at high acceleration into kinetic energy, and it results in a large sloshing motion. The amplitude and configuration of the liquid fuel interface and shift in the liquid center of gravity are investigated. In 1966, a full scale orbital test studying the design of the S-IVB propellant control was launched using a modified Saturn 1B, designated AS-203 (Ward *et al.* 1967). Recently, more studies have been conducted on the Sloshsat FLEVO (Facility for Liquid Experimentation and Verification in Orbit) mini satellite of Figure 1.4 to understand how sloshing affects the attitude and orbit control of space vehicles by monitoring the behavior of water in an instrumented tank (Prins 2000; Veldman *et al.* 2007).

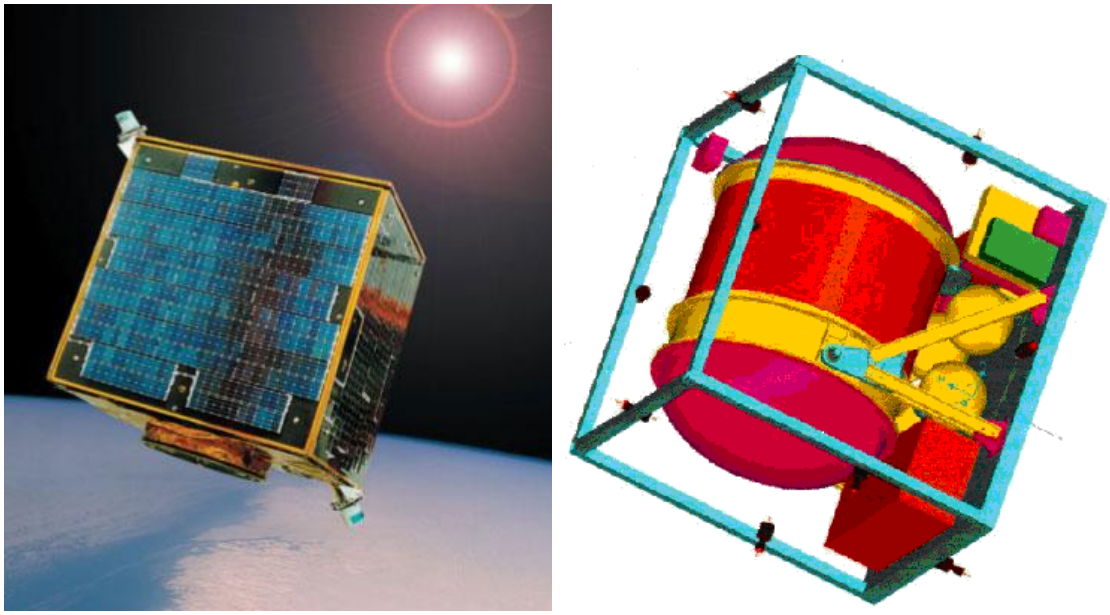

(a) **(b)**

Figure 1.4: Sloshsat FLEVO (Facility for Liquid Experimentation and Verification in Orbit) mini satellite for liquid fuel sloshing studies in a space environment. (Credits: NLR) (a) FLEVO satellite artwork (b) 3-D experiment tank integrated in the satellite

Thrust oscillation is also crucial in rocket designs since it has influence on the whole rocket system, including astronauts' safety, and might even result in a critical structural failure of the rocket. Active controls have been applied to reduce such a dangerous pogo oscillation and shock absorbers have been installed for the safety of astronauts and payloads by mitigating thrust oscillation (Yang and Andersen 1995). However, more detailed studies on the causes and influences of thrust oscillation are still required since it is related to engine pressure and fuel delivery systems, such as fuel/oxidizer pumps and injectors. Moreover, the bubble formations due to thrust oscillation may cause vapor ingestion into the combustor, resulting in engine failure. The enhanced heat transfer from droplets causes an ullage pressure rise and has a huge influence on the fuel tank structure. When focusing on the surface wave stability caused by thrust oscillation, it is clear that it has a very similar mechanism to the well-known Faraday wave, a parametrically excited surface wave. In 1831, Faraday found that a parametric vertical vibration generates subharmonic standing waves on the fluid surface (Faraday 1831). Since then, various surface wave modes and patterns and the influence of tank geometries have been studied (Das and Hopfinger 2008; Miles and Henderson 1990; Simonelli and Gollub 1989). A liquid depth to radius ratio is also an important parameter due to its influence on the nonlinear resonance. The standing surface wave becomes non-linear and unstable at certain specific conditions, and critical standing wave height and exciting frequency/magnitude level are proposed as a criteria for surface instability (Perlin and Schultz 2000). Goodridge *et al*. experimentally investigated the surface wave stability for fluids with different viscosity by measuring the exciting acceleration level where the surface becomes unstable, namely the threshold acceleration, in a cylindrical

container (Goodridge *et al.* 1996; Goodridge *et al.* 1997; Goodridge *et al.* 1999). They found that the threshold acceleration depends on surface tension and viscosity as well as forcing frequency.

Considering microgravity conditions in a typical spacecraft environment, the capillary effect becomes very important due to a small Bond number, the ratio of body (or gravitational) forces to surface tension forces. Thus, a study on the multiphase flow that includes interfacial dynamics is required in order to understand the liquid fuel dynamics in a spacecraft. However, experimental studies are limited because the microgravity conditions are hard to realize on the ground. Drop tower tests and in-flight tests have been conducted, but their short operational times prohibit simulating practical engineering problems. Thus, a high fidelity numerical simulation of such a multiphase flow in a space environment is crucial to compensate for the limitations of these experiments.

1.3 Multiphase Flow Computation Overview

Multiphase flows can be characterized by a system where two or more phases exist. This definition includes a wide range of cases, essentially all flows having moving/deforming surfaces that separate different fluids/phases. Figure 1.5 illustrates a multiphase flow separated by an interface between different fluids. Across the interface, fluid properties such as density, viscosity, and conductivity are discontinuous; and interfacial phenomena such as surface tension balancing normal stress variations and phase changes causing mass transport across phase boundaries exist (Prosperetti and Tryggvason 2007; Shyy *et al.* 1996).

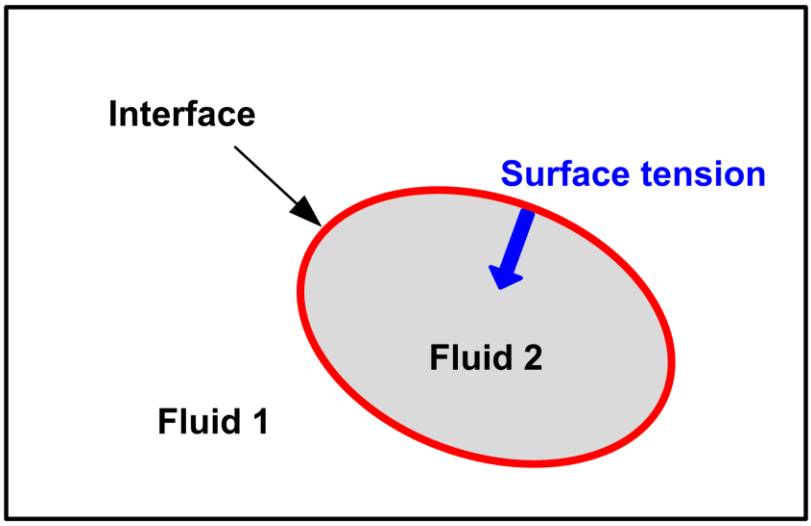

Figure 1.5: Illustration of a typical multiphase flow separated by an interface.

With the rapid progress made in computational techniques, a number of practically relevant fluid dynamic problems can now be computed with high accuracy. However, the multiphase flow computation still remains one of the most challenging problems due to the multiple time and length scales such as capillarity, diffusion/conduction, convection, and solid objects. Furthermore, the physical process involving moving/deforming interfaces with steep jumps in fluid properties, the interface topological changes along with merger/breakup, and the mass/heat transfer across phase boundary challenge the computational techniques.

The multiphase flow includes an interface between different phases having distinct physical properties; consequently, this involves identifying interface location and modeling interfacial dynamics, including a steep jump in fluid properties in response to surface tension effects. Various methods have been proposed and improved and each method has its own relative strengths and weaknesses (Osher and Fedkiw 2002;

Prosperetti and Tryggvason 2007; Scardovelli and Zaleski 1999; Shyy *et al.* 1996; Tryggvason *et al.* 2001).

1.3.1 Interface Representation

As reviewed in Shyy *et al.*, three main categories exist in representing and tracking the location and the shape of the moving boundaries, including Lagrangian (moving grid), Eulerian (stationary grid), and Eulerian-Lagrangian methods utilizing moving meshes with tags or markers in a stationary grid (Shyy *et al.* 1996).

Lagrangian methods

In Lagrangian (moving grid) methods, a body-fitted grid is used for tracking the interface in Figure 1.6(a). Thus, the interface location coincides with the computational grid, which is updated to match the moving interface location at every time instant in Figure 1.6(b). Ryskin and Leal implemented structured curvilinear body-fitted grids (Ryskin and Leal 1984), and Perot and Nallapati used unstructured tetrahedron grids for multiphase flow computations (Perot and Nallapati 2003). This method tracks the interface location explicitly, and it produces accurate results since the nature of a body-fitted grid guarantees the application of interfacial force and boundary conditions at the exact location. However, regenerating the whole grids for appropriate grid quality is required when large deformation and/or movement occur (Antaki et al. 2000). This is difficult and computationally expensive when large deformation/movements and/or topological changes take place, especially in 3-D computation (Johansen and Colella 1998).

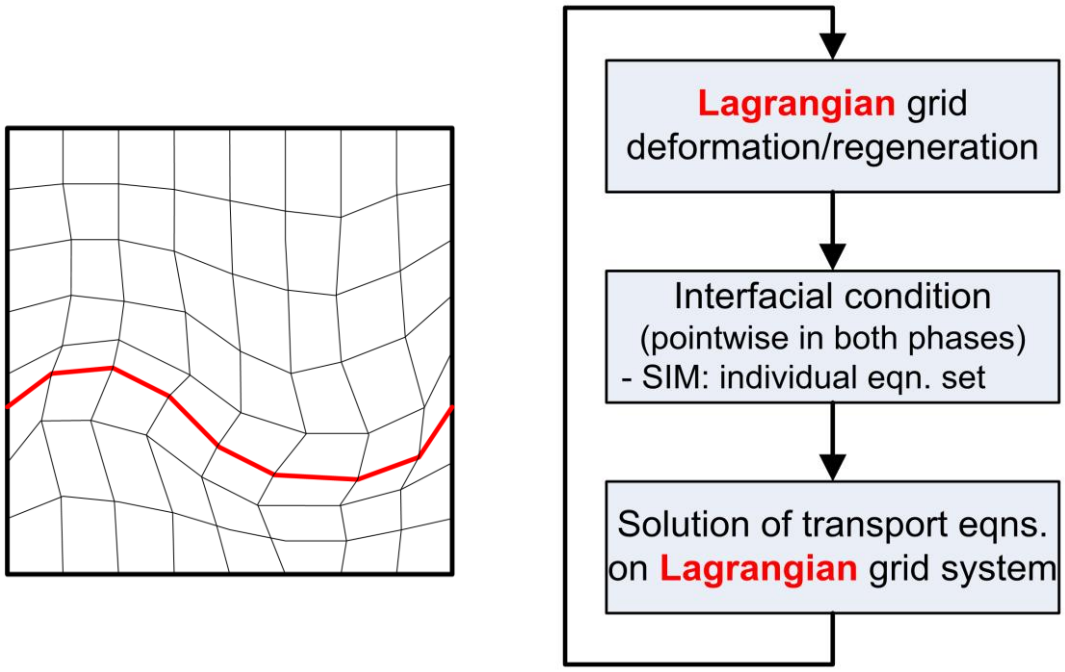

(a) **(b)**

Figure 1.6: Lagrangian methods. (a) Interface representation and tracking by body-fitted grids. (b) Solution procedure.

Eulerian methods

Unlike the Lagrangian methods, the Eulerian (stationary grid) methods extract the interface location with the help of a scalar function on a stationary computational grid in Figure 1.7(a). The interface is tracked implicitly via post processing of this scalar function. This category includes two popular methods, namely, the level-set (LS) method (Osher and Fedkiw 2001, 2002; Sethian and Smereka 2003) and the volume of fluids (VOF) method (Harlow and Welch 1965; Scardovelli and Zaleski 1999; Welch and Wilson 2000). The difference between these two methods is the choice of the scalar function, which is a signed-distance function in LS and volume fraction in VOF. Figure 1.7(b) shows the overall procedure of these Eulerian methods. Due to the implicit tracking of the interface, these methods can handle topological changes such as merger and break-up naturally (Shyy *et al.* 1996). However, it usually requires a fine grid to extract the interface location from Eulerian cells with the appropriate resolution. Moreover, an erroneous mass loss/gain and associated conservation laws' requirements in the LS method can cause loss of accuracy, and these are sometimes unacceptably large and detrimental (Enright *et al.* 2002). VOF methods track the volume explicitly, and thus there is no volume loss. However, it suffers from the difficulty of retrieving interface geometric properties from sharply changing volume fractions from cell to cell, and it is observed to produce spurious floatsam and jetsam in the region of the interface having a large curvature (Renardy and Renardy 2002; Scardovelli and Zaleski 1999).

Eulerian-Lagrangian methods

Eulerian-Lagrangian methods utilize a separate set of moving (Lagrangian) mesh and associated marker/tag system representing the interface on a stationary (Eulerian)

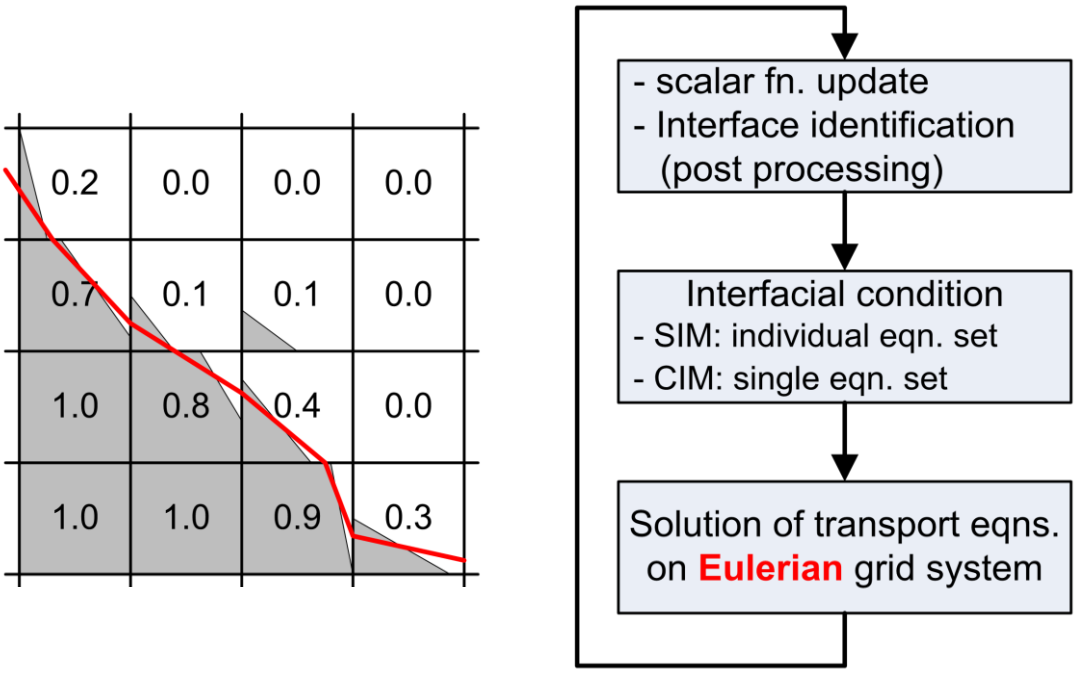

(a) **(b)**

Figure 1.7: Eulerian methods. (a) Interface representation and tracking in VOF method. (b) Solution procedure.

grid used to compute the flow fields in Figure 1.8(a). Thus, the interface can be tracked explicitly via Lagrangian meshes, which move freely on the stationary Eulerian grid by interpolating velocities from the Eulerian grid (Mittal and Iaccarino 2005; Peskin 1977; Peskin and McQueen 1989; Peskin 2003; Singh and Shyy 2007; Tryggvason *et al.* 2001). The conceptual framework is shown in Figure 1.8(b). These methods possess several desirable features when compared with Lagrangian or Eulerian methods. The interface representation does not require modifications to the computational grid for the field equations even for large deformation/moving as Lagrangian methods do. The explicit tracking of the interface generally presents finer resolution than computational grids, and thus, it requires a coarser grid than Eulerian methods (Glimm et al. 1998). Due to an explicit definition of the interface in the Lagrangian framework, the interface does not inaccurately diffuse in time and lose mass as the LS methods tend to do. An explicit definition of the interface also avoids inaccuracies caused by the errors in interface construction of VOF methods. The most serious concern about the Eulerian-Lagrangian methods is the complexity of the interface data, especially for topological changes. The source of difficulty lies in establishing valid connectivity information during surgical altering of the existing interface data (Shin and Juric 2002). Although such a procedure can be easily accomplished for two-dimensional interfaces, extension to three dimensions is a much more involved procedure. However, significant progress has been made and high accuracy computations for interfacial dynamics are reported in numerous publications (Shin and Juric 2002; Singh and Shyy 2007).

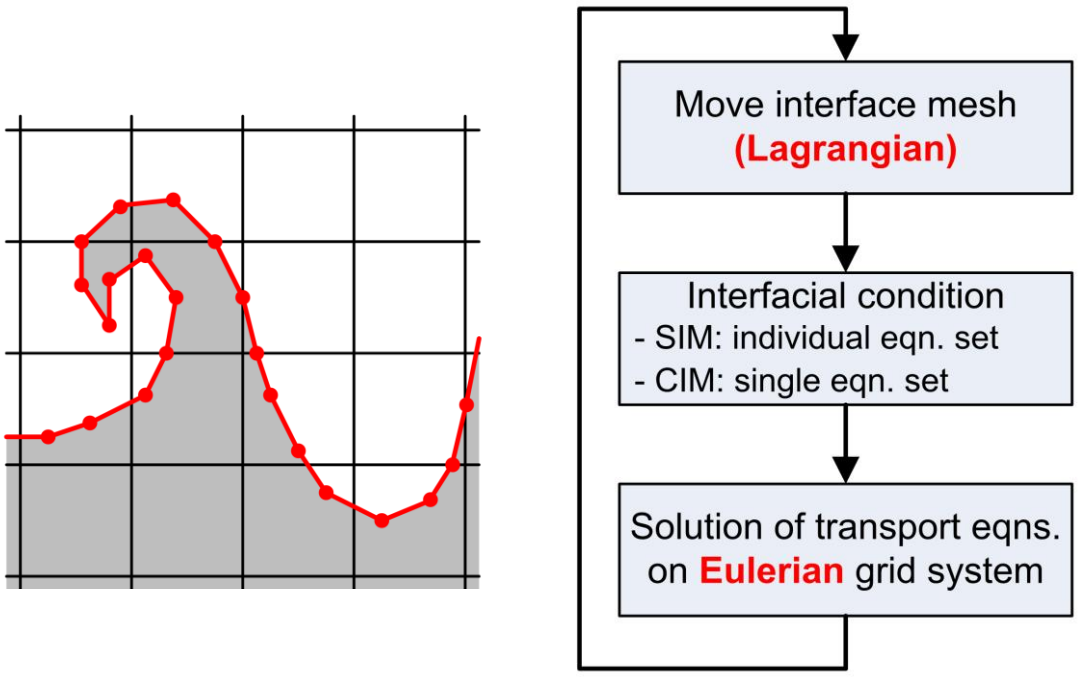

(a) **(b)**

Figure 1.8: Eulerian-Lagrangian methods. (a) Interface representation and tracking using moving meshes on the stationary Cartesian grid. (b) Solution procedure.

1.3.2 Interfacial Dynamics Modeling

Another challenging issue is the handling of the interfacial dynamics, even if the location and the shape of the interface are known at a given time. Across an interface, in general, the pressure and viscous stresses show discontinuities and fluid properties suddenly jump due to surface tension. Moreover, phase change includes mass and heat transfer across an interface. How to treat such a phase discontinuity and the associated capillary effects can be classified into two categories: the sharp interface method and the continuous interface method.

Sharp interface method (SIM)

The sharp interface method is a class of techniques that satisfy the jump condition between the flow fields on two sides of a phase boundary exactly on the interface of zero thickness in Figure 1.9(a). The interface is considered as a boundary separating two phases. The governing equations are solved separately for each phase with the boundary conditions of interfacial dynamics drawn from both sides. Eventually, these boundary conditions are required to match the required formulations explicitly in time and in space. A body-fitted grid in the Lagrangian method matches well with the sharp interface methods since the interface is aligned with the grid, and the interfacial dynamics can be applied exactly on the interface (Ryskin and Leal 1984). The cut-cell (Ingram *et al.* 2003; Udaykumar *et al.* 1996; Ye *et al.* 1999), ghost fluid (Kang *et al.* 2000; Liu *et al.* 2005), and some of the immersed interface methods (Leveque and Li 1994; Li and Lai 2001; Xu and Wang 2006) with Eulerian or Eulerian-Lagrangian methods are also under this category.

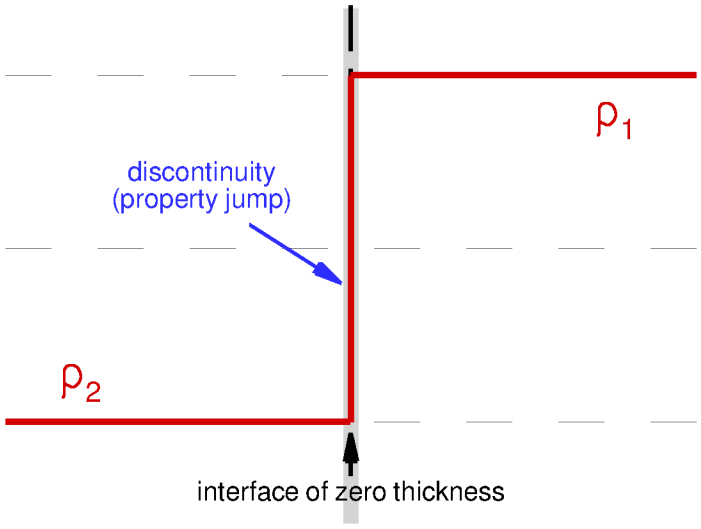

(a)

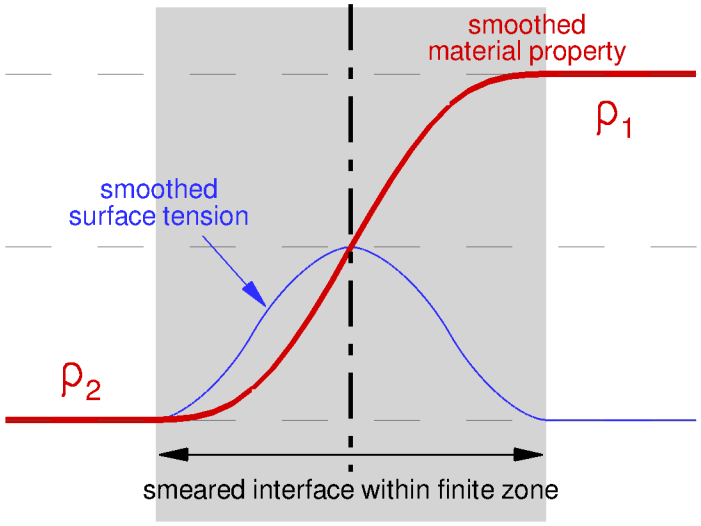

(b)

Figure 1.9: Interfacial dynamics modeling. (a) Sharp interface method with zero-thickness interface. (b) Continuous interface method with smeared interface within finite zone.

In general, the sharp interface method produces accurate results with less compromise of the interfacial conditions. However, it is more demanding computationally since the solution for each phase needs to be coupled with one another. For the Lagrangian method, accuracy issues related to mesh skewness can be challenging. While one can regenerate new meshes periodically, there is no guarantee that the quality of the flow solutions can be maintained between the different mesh systems. For both the moving mesh method and the cut-cell method, computational cost and numerical stability require special efforts for cases involving complex physics (phase change, heat/mass transfer, etc.) and substantial interface movement/deformation.

Continuous interface method (CIM)

Compared to the sharp interface method, the continuous interface method smoothes out the fluid property within a finite range and models the surface tension forces as a momentum source term within this range instead of as an interface of zero thickness in Figure 1.9(b). This facilitates a single fluid formulation for the entire domain with the flow/fluid properties varying gradually across the interface over a thin zone. This smeared/smoothed region contains usually three to four cells in thickness. The continuous interface method has been widely used with Eulerian-Lagrangian tracking (e.g., the immersed boundary method (Peskin 2003)) as well as Eulerian tracking such as level-set and volume-of-fluid because it is easier to implement. In general, the continuous interface method results in a lower order of accuracy than the sharp interface method due to the smearing of interfacial properties (Shyy 2004; Ye *et al.* 2004). However, this method is very effective and computationally more economical in handling various multiphase problems even with large deformation and moving interfaces. Effective treatments for

Table 1.1: Features of SIM and CIM

Interfacial dynamics	Sharp interface method (SIM)	Continuous interface method (CIM)
Equation sets	Separate set of equations for each phase	A single set of equations for all phases
Jump condition across interface	Explicit sharp jump within zero-thickness	Smooth changes within finite range
highlights	Higher order of accuracy (small spurious velocity current)	Effective in large deformation Easy to implement
issues	Computationally expensive and difficult (with large deformation in 3D)	Lower accuracy with smearing

handling large property changes between fluid domains across interfaces have also been proposed. Table 1.1 summarizes and compares the features of the sharp and continuous interface method.

1.3.3 Phase Change Modeling

The phase change and following mass transfer across phase boundary has not been well known due to its physical and numerical complexity. Son *et al*. solved the boiling bubbles problem using the level set method. They assumed the temperature inside the bubble to be constant and computed mass transfer with temperature gradient only at the liquid side (Son and Dhir 1998). This assumption is applied with the VOF method by Welch and Wilson (Welch and Wilson 2000). Juric and Tryggvason extended an immersed boundary method into a boiling problem by adding a smoothed latent heat

source term into the energy equation. They iterated the whole solution procedure estimating the amount of mass transfer (Juric and Tryggvason 1998). Shin and Juric simplify the method of computing the mass transfer from the known temperature gradient, but at both the liquid and the vapor sides (Shin and Juric 2002). However, continuous treatment with diffused material property of thermal conductivity limited the accuracy of heat transfer across the interface. Luo *et al*. implemented a hybrid method using sharp treatment for temperature computation with a standard continuous level-set method (Luo *et al.* 2005). Morgan improved accuracy in a phase change computation by correcting the temperature around the interface and directly using linear interpolation based on the interface temperature. This hybrid approach is very popular due to its simplicity and accuracy. However, the material properties are computed differently for momentum equations and the energy equation, and the sharp treatment is not appropriate for large deformable flows. Furthermore, Ferziger conducted an interesting study to demonstrate that the errors in continuous temperature treatment may be from the incorrect smoothed average of thermal conductivity around the interface in steady pure heat conduction problem with no phase change (Ferziger 2003).

1.3.4 Challenges and Recent Advances

Various methods have been proposed to represent and model the interface, each having strong and weak points. To represent the interface, a number of new developments have been proposed to compensate the existing methods. For example, Enright *et al.* implemented a particle level-set method, which utilizes Lagrangian markers around an interface with the Eulerian level-set method to ameliorate the mass loss observed in the original level-set method (Enright *et al.* 2002). The hybrid marker-VOF

method is proposed by Aulis *et al.*; it employs a Lagrangain marker-based tracking for better treatment of the interface (Aulisa *et al.* 2003). Sussman suggested the coupled LS-VOF method by combining the level-set method and the volume of fluid method (Sussman 2003). In the Eulerain-Lagrangian method, a topology change is the most challenging issue. Torres and Brackbill suggested unconnected point-set tracking methods for easy topology changes (Torres and Brackbill 2000). However, in this approach, it is difficult to control the interface resolution and compute geometry by spline-fitting. The marker-based triangle set tracking method is implemented by many researchers due to its easy geometric computation. This popular approach is utilized with connectivity information for easy topology changes and without connectivity information for easy control of resolution. Table 1.2 summarizes the recent advances in interface representation and tracking methods.

In the interfacial dynamics modeling, both sharp and continuous interface methods can be implemented with any interface representation and tracking method. However, the Lagrangian method is usually handled with a sharp interface method due to its body-fitted grids. In the Eulerian and Eulerian-Lagrangian method, the computational grid is non-boundary conforming, and the choice depends on the interface properties. The sharp interface method has a higher order of accuracy than the continuous interface method, and it is attractive when studying fixed or small deformation phase boundaries. The continuous interface method is generally adopted for moving interfacial flow.

Table 1.2: The summary of the recent advances in an interface representation and tracking method.

Base method	Improved method	Features
Level-set (LS)	particle level-set (Enright *et al.* 2002; Enright *et al.* 2005)	- cloud of markers around interface - ameliorates erroneous mass loss
Volume of fluid (VOF)	hybrid marker-VOF (Aulisa *et al.* 2003, 2004; Davis and Jones 1983)	- marker-based interface - avoids interface construction
LS and VOF	coupled LS-VOF (Sussman 2003)	- easy geometry computation in LS - excellent mass conservation in VOF
marker-based	point-set tracking (Torres and Brackbill 2000)	- set of unconnected points - easier handling of topology changes - geometry-computation by spline-fitting - difficult to control interface resolution
	connectivity free triangle-set tracking (Shin and Juric 2002)	- set of unconnected of triangles - easy geometry computation - level-contour reconstruction for topology changes - difficult to control interface resolution
	marker-based triangle-set tracking (Singh and Shyy 2007; Tryggvason *et al.* 2005)	- set of connected triangles - easy to control interface resolution - level-contour reconstruction for topology changes

1.4 The Present Approach

In the present study, a 3-D adaptive Eulerian-Lagrangian method is adopted for explicit tracking of Lagrangian grids and effective computation of a Eulerian frame in order to simulate a complex multiphase flow around irregular geometries. Both fluid and solid phase boundaries are implemented in a unified framework for practical engineering problems. The large-deformable fluid boundaries are modeled using a continuous interface method, and the surface tension between fluid interfaces is smeared within finite distance. The solid boundaries are treated by a sharp interface method along with the ghost cell method by reconstructing the solution on the ghost cell based on the known solid boundary condition. The contact line where the fluid interface meets the solid boundary is modeled using a contact line force model, which enforces the given contact angle dynamically. For the moving contact line treatment, a local slip condition is applied around the contact line. The multi-level adaptive Cartesian grid method is implemented to resolve the sufficient computation resolution locally and dynamically, especially around the interface with effective computation. The energy equation solver is added into the present incompressible flow solver with Boussinesq approximation for buoyancy force computation. The phase change model using continuous treatment for temperature is developed with modified smoothing of material properties. Figure 1.10 shows the schematic drawing of the present approach for multiphase flow computation.

1.5 Scope and Outline of the Dissertation

In chapter 2, the implemented 3-D adaptive Eulerian-Lagrangian method is described. First, the interface representation method is presented, and interfacial dynamics modeling is described for each continuous interface method for the fluid phase

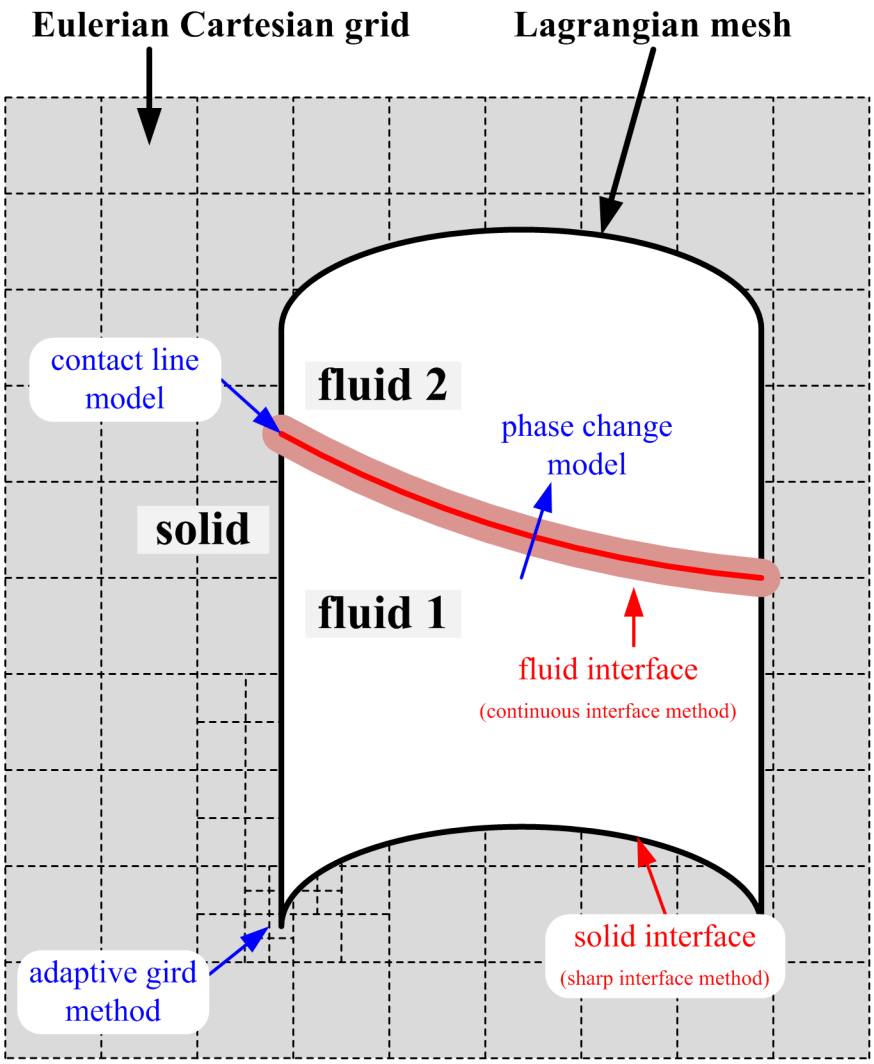

Figure 1.10: Illustration of the present approach.

boundary and the sharp interface method for the solid phase boundary. The dynamic contact line force model at the fluid-fluid-solid contact line and adaptive grid method is followed.

Chapter 3 discusses isothermal computation results. First, the present contact line force model is validated by simulating capillary tube cases with various contact angles, and three spacecraft fuel delivery applications are investigated via direct numerical simulations with experimental validation and scaling analysis: liquid fuel draining and different draining flow regimes under microgravity; liquid fuel sloshing and its influence on the vehicle dynamics under sudden reduction in acceleration; and liquid fuel surface stability under vertically oscillating gravitational acceleration like rocket thrust oscillation.

In chapter 4, thermo-fluid transport computations are conducted. The laminar natural convection flow driven by the buoyancy force in a cavity is computed for validation study for the present approaches including thermal effect. 1-D two-phase Stefan problems and 2-D melting case by convection/diffusion flow are presented for validation purposes of the implemented phase change model.

In chapter 5, the conclusions and future work for the present study are summarized.

CHAPTER 2

3-D ADAPTIVE EULERIAN-LAGRANGIAN METHOD

This chapter presents the key components of the implemented marker-based 3-D adaptive Eulerian-Lagrangian method. In section 2.1, the governing equations for incompressible flow and the numerical treatment of a single fluid formulation for all fluid phases are discussed. Section 0 shows how to represent and track the interface. In section 2.3, the interfacial dynamics of continuous treatment for the fluid interface are discussed, and in section 2.4, the sharp interface treatment for solid interface is discussed. Section 2.5 deals with the interaction between the fluid boundary and the solid boundary, and the contact line force model. The phase change model is discussed in section 2.6, and the adaptive grid is implemented for effective computation in section 2.7.

2.1 Governing Equations and Solution Procedure

Figure 2.1 shows a schematic drawing for general multiphase flow computation with solid interface ($\boldsymbol{\Gamma_s}$) and fluid interface ($\boldsymbol{\Gamma_f}$). In the fluid domain ($\boldsymbol{\Omega_f}$), the non-dimensionalized incompressible Navier-Stokes equations for mass, momentum, and energy conservation are given in Eqs. (2.1), (2.2), and (2.3), respectively, which account for the interfacial dynamics as source terms in the governing equations: surface tension effects of fluid interfaces as a momentum forcing term ($\boldsymbol{F_f}$), and the latent heat effects across fluid interfaces as an energy source term (Q_f). In the governing equations, $\boldsymbol{u}$ is the

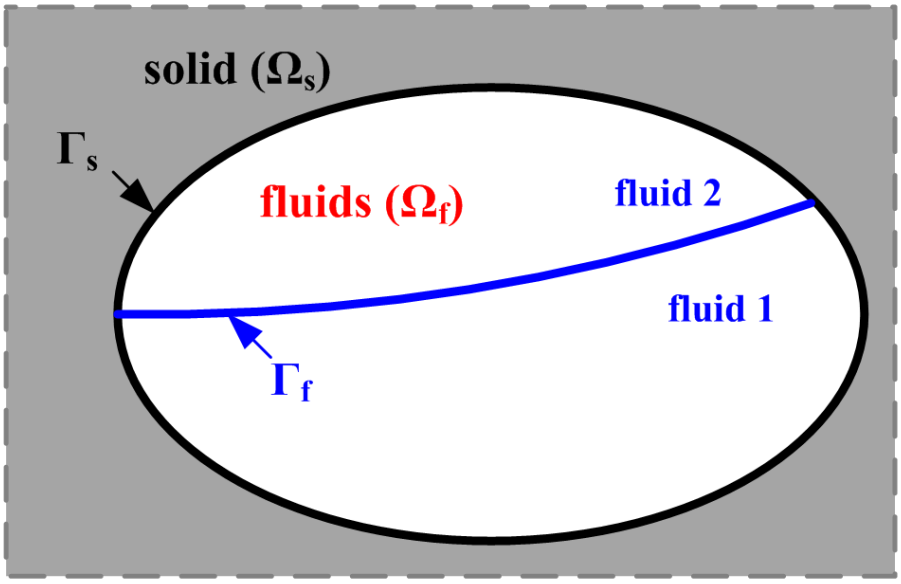

Figure 2.1: Schematic drawing for general multiphase flow computation. Fluid domain (Ω_f) and solid domain (Ω_s) are divided by solid interface (Γ_s). The fluid domain (Ω_f) is subdivided into multiphase fluids by fluid interface (Γ_f).

velocity vector, and ρ, μ, C, K, and p is the density, viscosity, heat capacity, thermal conductivity, and pressure, respectively.

$$\frac{\partial \rho}{\partial t} + \nabla \cdot (\rho \boldsymbol{u}) = 0 \tag{2.1}$$

$$\frac{\partial \rho \boldsymbol{u}}{\partial t} + \nabla \cdot (\rho \boldsymbol{u}\boldsymbol{u}) = -\nabla p + \frac{1}{Re}\nabla \cdot (\mu \nabla \boldsymbol{u} + \mu \nabla^T \boldsymbol{u}) + \frac{1}{Fr}\rho \boldsymbol{g} + \frac{1}{We}\boldsymbol{F}_f \tag{2.2}$$

$$\frac{\partial \rho CT}{\partial t} + \nabla \cdot (\rho CT \boldsymbol{u}) = \frac{1}{Re \cdot Pr}\nabla \cdot (K \nabla T) + Q_f \tag{2.3}$$

Here, all variables are non-dimensionalized by a characteristic velocity (U) and length scale (L), standard gravity (g_0), and liquid material properties (density ρ_l, viscosity μ_l, heat capacity C_l, thermal conductivity K_l, and surface tension σ). The non-

dimensional parameters of Reynolds, Froude, Weber, and Prandtl numbers in Eq. (2.2) and (2.3) are defined as, $\mathrm{Re} = \rho_l \mathrm{UL}/\mu_l$, $\mathrm{Fr} = \mathrm{U}^2/(\mathrm{g_0 L})$, $\mathrm{We} = \rho_l \mathrm{U}^2 \mathrm{L}/\sigma$, and $\mathrm{Pr} = \mu_l \mathrm{C_l}/\mathrm{K_l}$. In addition, the capillary number and bond number can be defined as $\mathrm{Ca} = \mathrm{We}/\mathrm{Re} = \mu_l \mathrm{U}/\sigma$ and $\mathrm{Bo} = \mathrm{We}/\mathrm{Fr} = \rho_l \mathrm{g_0 L}^2/\sigma$, respectively.

2.1.1 Smoothed Material Properties

A single set of equation formulations for all fluid phases in the whole domain is made possible by smoothing out the discontinuous material properties across the interface. This is achieved with the help of an approximate Dirac delta function (δ_h) and an indicator function (I). The approximate Dirac delta function, originally proposed by Peskin (Peskin and McQueen 1989), is implemented over a finite thickness of 4 cell width instead of the analytical form of the Dirac delta function, which has a non-zero value only at the zero-thickness interface. The indicator function is a scalar function in the stationary Eulerian frame varying from zero to one smoothly across the interface and has a value of 0.5 at the interface location.

The analytical form of the Dirac delta function is only non-zero at the exact interface location. However, this approach cannot be used along with a discretized set of equations because the discrete points on the Eulerian ($\boldsymbol{x}$) and Lagrangian ($\boldsymbol{X}$) frameworks do not necessarily coincide. For this reason, approximations to the Dirac delta function, which introduce a region that represents the interface over a finite thickness, have been studied for their properties (Engquist *et al.* 2005; Peskin 2003; Stockie 1997). In the present study, the discrete Dirac delta function approximation, which supports the conservation rules dictated by the zeroth, first, and second moments as described in

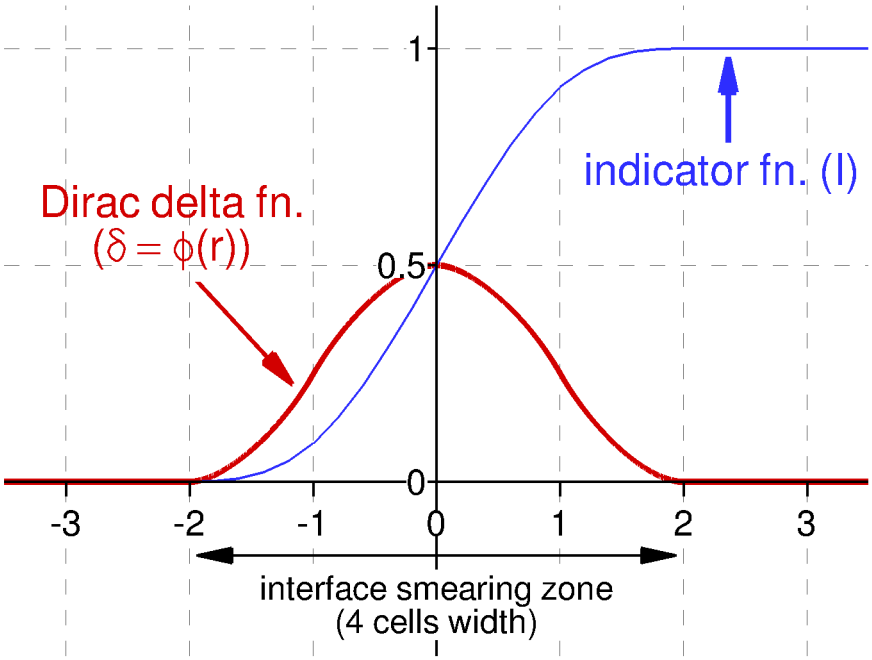

Figure 2.2: The discrete Dirac delta function and the indicator function around an interface.

Peskin (Peskin 2003), is employed as the base discrete form using the one-dimensional representation given in Eq. (2.4).

$$\phi(\boldsymbol{r}) = \begin{cases} \frac{1}{8}\left(5 - 2|\boldsymbol{r}| - \sqrt{-7 + 12|\boldsymbol{r}| - 4|\boldsymbol{r}|^2}\right) & 1 \le |\boldsymbol{r}| \le 2 \\ \frac{1}{8}\left(3 - 2|\boldsymbol{r}| - \sqrt{1 + 4|\boldsymbol{r}| - 4|\boldsymbol{r}|^2}\right) & 0 \le |\boldsymbol{r}| \le 1 \\ 0 & otherwise \end{cases} \quad \textbf{(2.4)}$$

In Eq. (2.4), $|\boldsymbol{r}|$ is the shortest distance between the cell-center to the interface location, and it is normalized by the cell spacing (h). Because $\phi(\boldsymbol{r})$ becomes zero when the distance is larger than two cells width, the smearing region becomes limited to two-cell widths on each side of the interface. Figure 2.2 shows the discrete Dirac delta

function approximation ($\phi(\boldsymbol{r})$) in Eq. (2.4) and the indicator function (I) around the interface.

One way to extend the one-dimensional representation of the discrete Dirac function to two- and three-dimensions is to use the multiplication rule as presented in Eq. (2.5) (Peskin 2003). This approach is attractive due to its low computational cost.

$$\delta_h(\boldsymbol{r}) = \frac{1}{h_x h_y h_z}\phi(r_x)\cdot\phi(r_y)\cdot\phi(r_z) \tag{2.5}$$

In Eq. (2.5), the distance vector ($\boldsymbol{r}$), is presented in Cartesian components, indicated by the subscripts. This results in a discrete Dirac delta function (δ_h), which is an approximation based on grid spacing (h).

On the other hand, when the information of the minimum distance is readily available, as in the case of the level-set methods, it is possible to directly utilize the distance function with the one-dimensional form of the discrete Dirac function, ϕ, as shown in Eq. (2.6).

$$\delta_h(r_x, r_y, r_z) = \frac{1}{\sqrt{h_x^2 + h_y^2 + h_z^2}}\phi\left(\sqrt{r_x^2 + r_y^2 + r_z^2}\right) \tag{2.6}$$

Obtaining the indicator function accurately is critical for numerically simulating multiphase flow problems. In the literature, two closely related but numerically distinct forms of computations can be found. One of these methods adopts the solution of a Poisson equation using the form in Eq. (2.7). The other utilizes a discrete form of the Heaviside step function from the analytical solution of Eq. (2.7) using 1-D form of the discrete Dirac delta function given in Eq. (2.8).

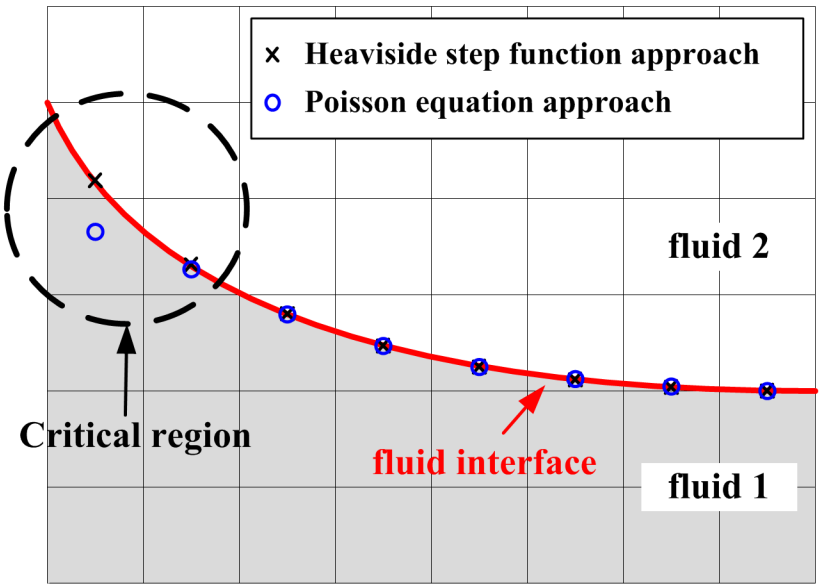

Figure 2.3: The comparison of two approaches for indicator function computation. The Poisson equation approach may misrepresent interface location near boundary.

$$\nabla^2 I = \nabla\left(\int_\Gamma \delta(\boldsymbol{x}-\boldsymbol{X})d\Gamma\right) \tag{2.7}$$

$$I(\boldsymbol{x}) = H\big(r = \boldsymbol{n}\cdot(\boldsymbol{x}-\boldsymbol{X})\big) = \int_{-\infty}^{r}\delta(h)dh \tag{2.8}$$

On dealing with contact line problems, in which the interface is on a solid surface, the above approach requires boundary conditions in the vicinity of the interface. Because the variation of the indicator function at this region depends on the normal direction, it is difficult to utilize an appropriate boundary condition. One possible condition is to assume zero variation in the indicator value at the normal direction to the boundary. However, this condition leads to an interface representation that makes a right angle to the domain boundary, which can result in a different interface shape on the Cartesian grid than the

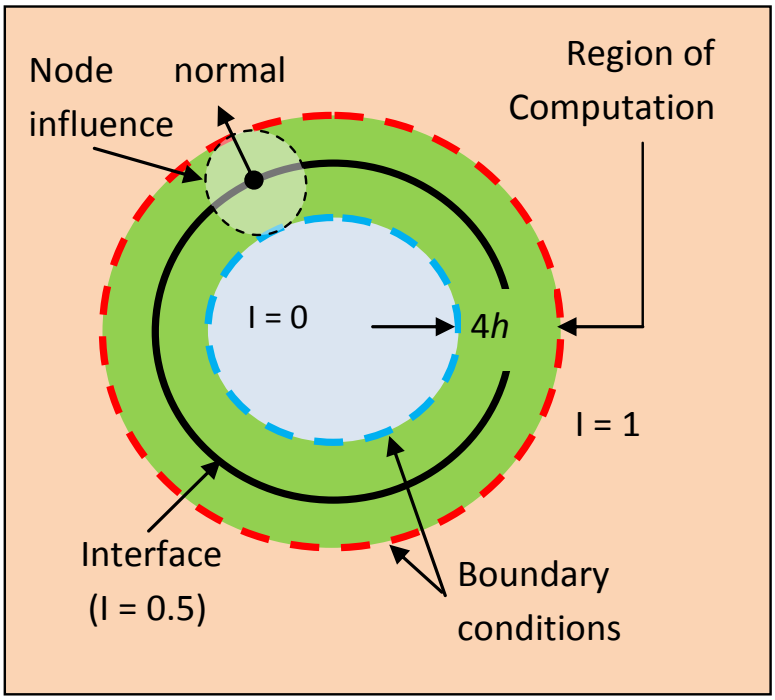

Figure 2.4: Region of computation and boundary conditions for Dirac delta function and indicator function.

actual interface at angles away from 90^o. Using linear extrapolation can also cause an incorrect interface line ($I = 0.5$) around this region. Figure 2.3 illustrates such a scenario.

This issue can be handled using an alternate way of computing the indicator function, which utilizes the shortest distance value between the cell-center to the interface location by integrating the one-dimensional form of the discrete Dirac function given in Eq. (2.8). This approach is known to be applicable more generally than the Poisson equation solver method since it requires only distance information from the interface without boundary conditions, and thus gives accurate values even at the boundaries (Uzgoren et al. 2009).

Considering the support of a discrete Delta function and an indicator function, the computations are only performed over the two-cell width region on each side of the interface to reduce the computational cost of the Poisson equation. Figure 2.4 illustrates this region for the computation. This region is obtained by determining the cells around each surface node with a two-cell width radius. The boundary conditions away from the interface are set to yield the desired variation, i.e. zero or one. This approach is computationally effective when these boundary conditions are away from the interface location.

Separate indicator functions for the fluid and solid interfaces are used to distinguish the solid interface (modeled by a sharp interface method) from the fluid interface (modeled by a continuous interface method) on the fixed Eulerian Cartesian grids. Such a feature of the indicator function enables handling the complex nature of geometric operations in a computationally efficient way.

The smoothed fluid properties such as density and viscosity are computed using Eqs. (2.9)-(2.12).

$$\rho = \rho_2 + (\rho_1 - \rho_2)I \tag{2.9}$$

$$\frac{\rho}{\mu} = \left(\frac{\rho}{\mu}\right)_2 + \left[\left(\frac{\rho}{\mu}\right)_1 - \left(\frac{\rho}{\mu}\right)_2\right] I \tag{2.10}$$

$$\rho C = (\rho C)_2 + [(\rho C)_1 - (\rho C)_2]\, I \tag{2.11}$$

$$\frac{\rho C}{k} = \left(\frac{\rho C}{k}\right)_2 + \left[\left(\frac{\rho C}{k}\right)_1 - \left(\frac{\rho C}{k}\right)_2\right] I \tag{2.12}$$

2.1.2 Solution Procedure: Projection Method

The governing equations Eqns. (2.1)-(2.3) are solved using a projection method with a staggered grid finite-volume formulation. The pressure and fluid properties are stored at the cell center and face-normal velocities are stored on the Cartesian cell faces. The convection term ($\boldsymbol{N}$) is discretized using a 3rd order ENO scheme in space and a 2nd order Runge-Kutta integration in time. The central difference scheme and Crank-Nicholson method is implemented for the viscous term ($\boldsymbol{L}$). The discretized solution procedures are summarized in Eqns. (2.13)-(2.16). In Eqn. (2.17), $\nabla \cdot \boldsymbol{u}^{n+1}$ term is zero if the phase change doesn't occur and mass is not transferred across the interface.

$$\frac{T^{n+1} - T^n}{\Delta t} = -\nabla \cdot (\boldsymbol{u}T)^{n+1/2} + \frac{1}{(\rho C)^{n+1}}\left[\nabla \cdot (K\nabla T)^{n+1} + Q_f^{n+1}\right] \tag{2.13}$$

$$\frac{\boldsymbol{u}^* - \boldsymbol{u}^n}{\Delta t} = -\boldsymbol{N}\left(\boldsymbol{u}^{n+1/2}\right) + \frac{1}{\rho^{n+1}}\left[-\nabla p^n + \boldsymbol{L}\left(\boldsymbol{u}^{n+1/2}\right) + \boldsymbol{F}^{n+1}\right] \tag{2.14}$$

$$\boldsymbol{u}^{**} = \boldsymbol{u}^* + \frac{\Delta t}{\rho^{n+1}}\nabla p^n \tag{2.15}$$

$$\boldsymbol{u}^{n+1} = \boldsymbol{u}^{**} - \frac{\Delta t}{\rho^{n+1}}\nabla p^{n+1} \tag{2.16}$$

with Pressure Poisson equation of Eq. (2.17) by taking divergence of Eq. (2.16).

$$\nabla^2(p^{n+1}) = -\frac{\Delta t}{\rho^{n+1}}(\nabla \cdot \boldsymbol{u}^{**} - \nabla \cdot \boldsymbol{u}^{n+1}) \tag{2.17}$$

2.2 Interface Representation and Tracking

2.2.1 Marker-based Interface with Connectivity Information

In this marker-based Eulerian-Lagrangian method, the interface is represented by massless markers in coordination with each other in order to maintain the interface connectivity information. The corresponding data structure is established via line-segments in two-dimensional domains and triangles in three-dimensional domains, as represented in Figure 2.5. Markers store the surrounding elements' indices, and elements store their neighboring elements based on the edge that they share. For boundary elements, a negative value is used to refer to the computational boundary or intersecting solid elements in Figure 2.6.

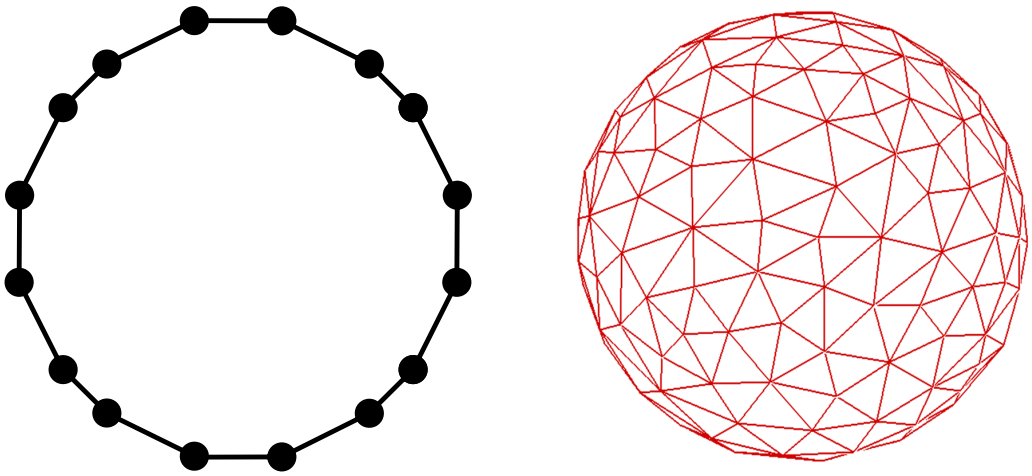

(a) **(b)**

Figure 2.5: Examples of interface surface represented by massless markers and elements. (a) Line-segments in 2-D. (b) Triangular elements in 3-D.

2.2.2 Interface Advection

The marker locations, denoted by $\boldsymbol{X}$ in the Lagrangian frame, are updated from the velocities at its location, $\boldsymbol{U}(\boldsymbol{X})$, in Eq. (2.18).

$$\frac{\partial \boldsymbol{X}}{\partial t} = \boldsymbol{U}(\boldsymbol{X}) \tag{2.18}$$

Fluid interfaces use the computed flow solution field to obtain the marker velocities as shown in Eq. (2.19). In this equation, the discrete Dirac delta function, $\delta_h(\boldsymbol{x} - \boldsymbol{X})$, is employed for converting the Eulerian velocity field, $\boldsymbol{u}(\boldsymbol{x})$, to Lagrangian form, $\boldsymbol{U}(\boldsymbol{X})$. The interface velocity is exactly the same as the fluid velocity at the interface location if there is no mass transfer ($\dot{m}$) in Eq. (2.19). However, with phase change, the velocity component from the mass transfer across the interface should be considered. On the other hand, the solid interfaces use the prescribed velocity field to

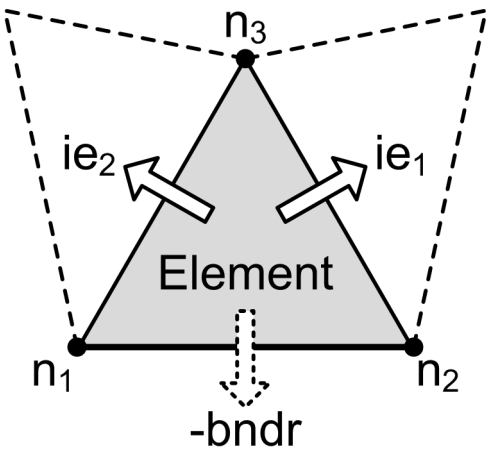

Figure 2.6: Connectivity information for an interface element. Each edge has information for two neighboring elements. Boundary information such as computational boundary and solid elements is stored using negative value for differentiating inner elements.

advance the marker points using Eq. (2.18).

$$\boldsymbol{U}(\boldsymbol{X}) = \int_{v} \boldsymbol{u}(\boldsymbol{x})\boldsymbol{\delta}(\boldsymbol{x} - \boldsymbol{X})dV - \frac{\dot{m}}{\rho_f} \cdot \boldsymbol{n} \tag{2.19}$$

2.2.3 Interface Grid Quality

As the marker points advance to a new position with time, the interface surface mesh can exhibit an uneven distribution of marker points. In order to maintain consistent computational accuracy, the spacing between marker points is rearranged by adding or deleting markers whenever two markers come too close to or too distant from each other. The criteria for the distance between the adjacent markers are estimated based on the requirements posed by the background grid and the function relating Eulerian quantities to Lagrangian. For fluid interfaces, each cell should contain at least one and at most two markers within its volume in order to achieve continuous representation for transferred quantities like surface tension. This constraint can be used to approximate the distance between a marker located at $\boldsymbol{X}$ and an adjacent marker located at $\boldsymbol{X}_{ngbr}$ as a function of the Eulerian grid spacing, Δ, given in Eq. (2.20).

$$\frac{\Delta}{3} < \left|\boldsymbol{X} - \boldsymbol{X}_{ngbr}\right| < \Delta \tag{2.20}$$

For the solid interface, there is no transferred quantity between Eulerian and Lagrangian quantities, and coarse resolution is accepted if the computed indicator function is able to represent the physical geometry. Thus, two or three times of distance between markers can be utilized for the solid interfaces.

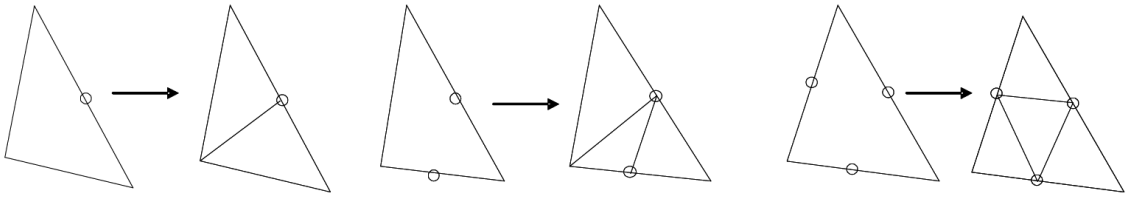

(a)

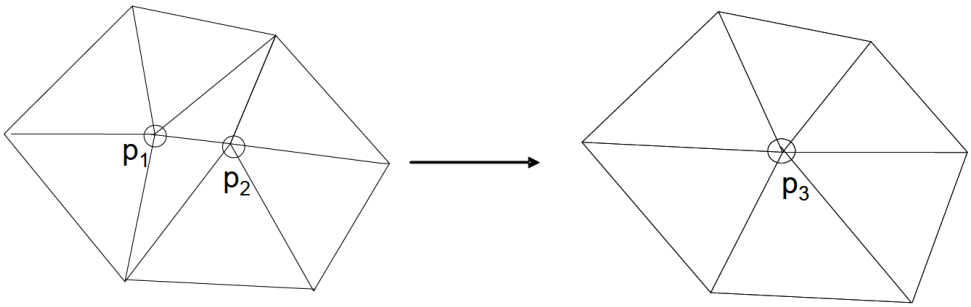

(b)

Figure 2.7: Examples of interface grid quality control for inner elements. (a) A long edge is divided into two edges by creating a marker at the midpoint (b) A small edge is collapsed to its midpoint, and neighboring edges are removed.

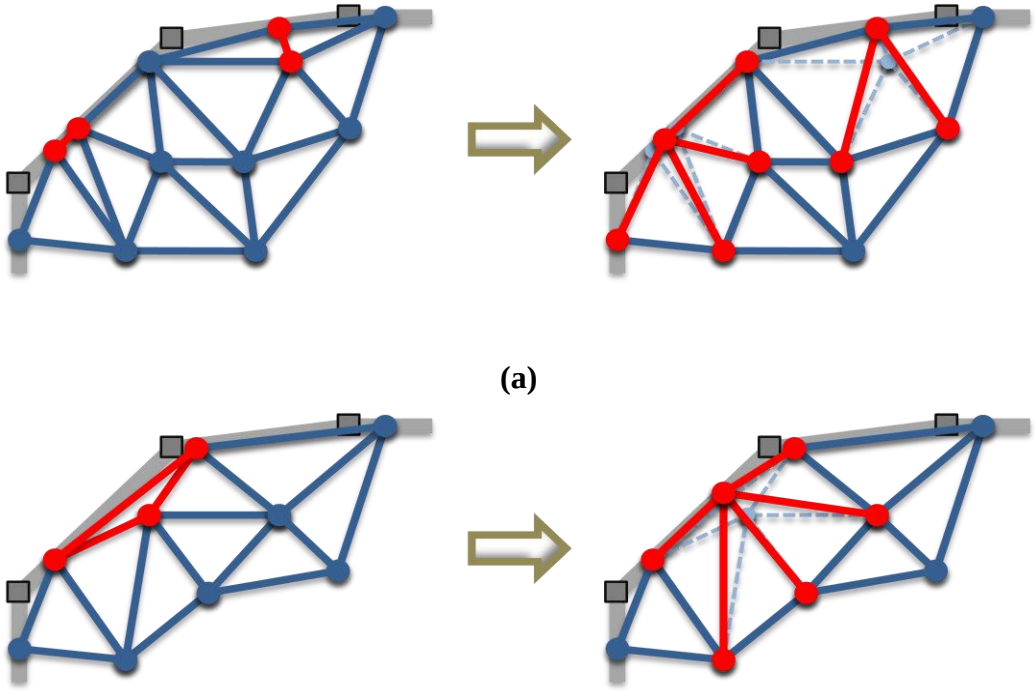

(a)

(b)

Figure 2.8: Examples of interface grid quality control for boundary elements and edges. (a) Short edges are collapsed to its midpoint and are snapped to the boundary. (b) A flat boundary edge is removed and inner elements are extended to the boundary.

Maintaining grid quality by adding or removing the marker can be done relatively easily when the element is located inside and is surrounded by other elements. Figure 2.7 Shows examples of interface grid quality control for inner elements. The new marker is created at the mid-point of a long edge and neighboring elements are divided into two creating edges. For the short edge, two markers of the edge collapse into its midpoint, and two neighboring elements are removed. However, it can be more complicated for the boundary elements. Examples of interface grid quality control for boundary elements are described in Figure 2.8. The volume errors during these processes can be recovered by

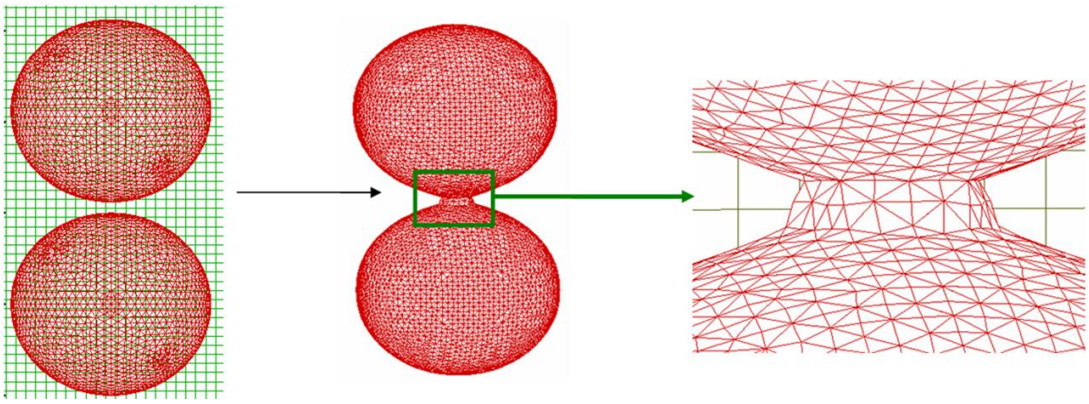

Figure 2.9: An example of topology change. Two spheres merge into one by level-contour-based reconstruction when they approach each other.

adjusting the location of the modified marker in its normal direction, as discussed by Singh and Shyy (Singh and Shyy 2007).

2.2.4 Topology Change: Interface Reconstruction

The level-contour-based interface reconstruction technique with connectivity information is implemented to handle topological changes such as merger or break-up. With connectivity information, the time-consuming reconstruction is facilitated only in the case of merger/break-up by examining the possibility of topological changes at prescribed time intervals. These reconstruction procedures can be done locally for a specific interface body, and the errors in the phase volume after reconstruction are explicitly corrected by perturbing the markers in the local normal direction. Figure 2.9 shows an example of an interface reconstruction between two spheres.

2.3 Fluid Interface: Continuous Interface Method

The continuous interface method is implemented for all fluid phases by a single fluid formulation due to its effectiveness in modeling highly deformable fluid interfaces. The surface tension and latent heat at the interface are smeared around Eulerian cells.

The surface force computation of Eq. (2.21), where σ is the surface tension and κ is the curvature of the interface, is applied as the source term in momentum Eq. (2.2).

$$\boldsymbol{F}_f = \int_{\Gamma} \sigma\kappa\delta(\boldsymbol{x} - \boldsymbol{X}) d\Gamma \tag{2.21}$$

The surface force of the interface is also transformed from Lagrangian quantity ($\boldsymbol{X}$) to Eulerian quantity ($\boldsymbol{x}$) via the approximate discrete Dirac delta function, $\delta_h(\boldsymbol{x} - \boldsymbol{X})$. Two popular methods exist in computing surface tension on a discretized interface element (line-segments in 2D and triangles in 3D). The first approach is a direct curvature computation, where the unit normal vector and curvature can be computed using curve fitting for two-dimensional interfaces (Francois and Shyy 2002, 2003; Ye *et al.* 1999) and surface fitting for three-dimensional interfaces (de Sousa et al. 2004) in Eq. (2.22). Another approach implements a line integral form shown in Eq. (2.23) with normal and tangent vectors from the given interface elements (Al-Rawahi and Tryggvason 2002; Tryggvason *et al.* 2001).

$$\boldsymbol{\delta f} = \int_{\delta\Gamma} \sigma\kappa d\Gamma \tag{2.22}$$

$$\boldsymbol{\delta f} = \int_{\delta\Gamma} \sigma(\boldsymbol{n} \times \boldsymbol{\nabla}) \times \boldsymbol{n} d\Gamma = \int_{s} \sigma(\boldsymbol{t} \otimes \boldsymbol{n}) ds \tag{2.23}$$

There are two important observations to be made here: the net surface tension force on a closed surface should be zero (conservation); and the curvature computation

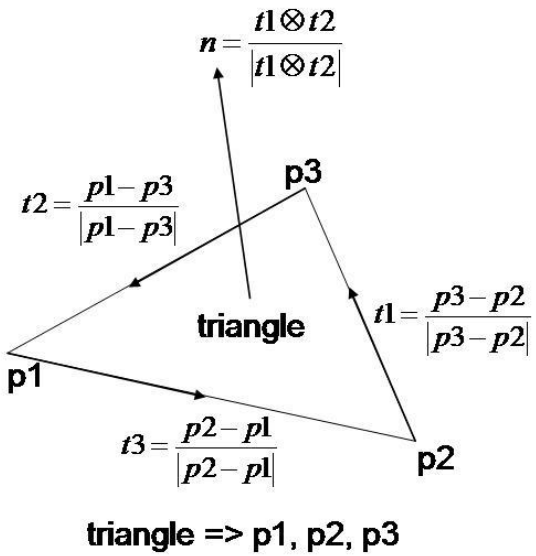

Figure 2.10: The definition of the unit normal and tangent vectors on the triangle element of fluid interface.

using interpolation based methods is numerically sensitive and often requires some form of data smoothing. (Al-Rawahi and Tryggvason 2004; de Sousa *et al.* 2004; Francois and Shyy 2002, 2003) The use of Eq. (2.22) does not enforce conservation whereas the line-integral form, Eq. (2.23), does not require explicit curvature computation and maintains the conservation.

In the present study, the line-integral form approach developed by Singh (Singh 2006) is implemented by computing the local normal and tangent vectors in Figure 2.10 along the triangle edges using the simple approach of Al-Rawahi (Al-Rawahi and Tryggvason 2002, 2004) shown in Eq. (2.24).

$$\boldsymbol{\delta f} = \int_s \sigma(\boldsymbol{t} \otimes \boldsymbol{n}) ds = \sum_{edges} \sigma(\boldsymbol{t} \otimes \boldsymbol{n})_{edge} \Delta s \qquad \textbf{(2.24)}$$

2.4 Solid Interface: Sharp Interface Method using Ghost Cells

Solid interfaces are modeled using the sharp interface method by reconstructing solution fields around an interface to incorporate the given boundary condition on the solid interface in an Eulerian Cartesian grid. Solution reconstruction can be conducted either on the fluid side or solid side in Figure 2.11. Both approaches work well for a single phase flow around solid surfaces. However, the fluid velocity reconstruction method ignores the influence of surface tension from the fluid interface by reconstructing fluid velocities directly and, thus, tends not to describe the moving phase boundary near the solid interface. Alternatively, the velocity reconstruction on the solid side can be implemented via ghost cells, which are defined as solid cells having at least one neighboring fluid cell. This approach works well even with the contact line where the fluid interface meets the solid interface without disturbing the fluid velocities.

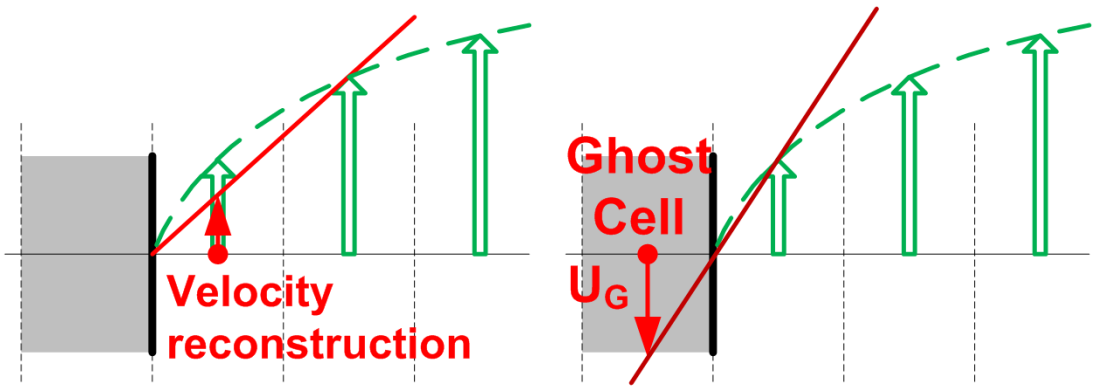

Figure 2.11: Two approaches for the solution reconstruction in the sharp interface method. (a) Fluid velocity reconstruction computes fluid velocities directly from interpolation and loses the influence of surface tension near contact line. (b) Solid velocity reconstruction via ghost cells keeps the influence of surface tension.

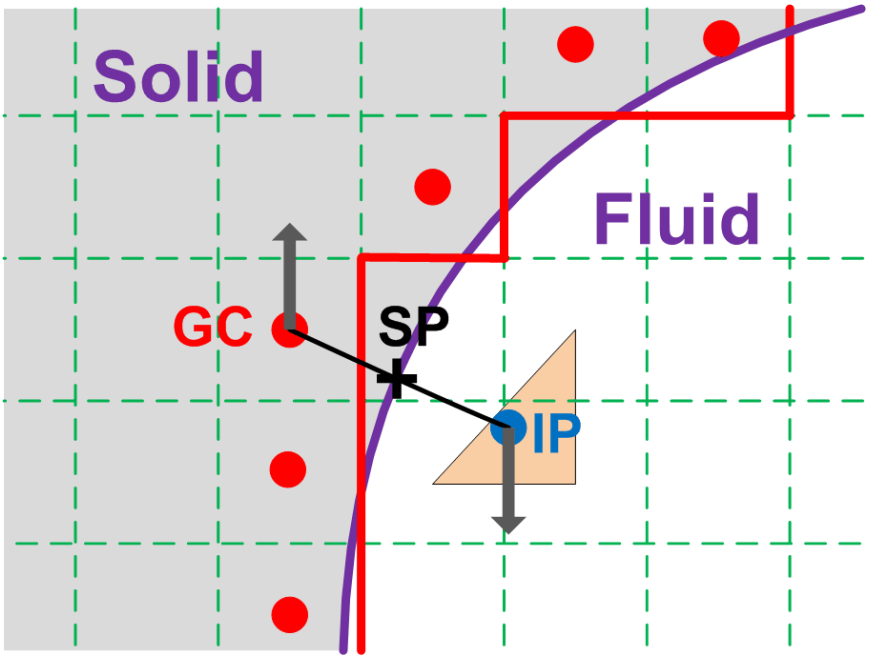

Figure 2.12: Identification of ghost cell (GC), solid point (SP), and imaginary point (IP). The interpolation of velocity is conducted on the imaginary point first, and then computed at the ghost cells based on the velocity of solid point.

The solution reconstruction on the ghost cell is conducted by a linear or bi/trilinear interpolation scheme using solutions at the solid surface and at the known fluid cells. Avoiding extrapolation due to the location of a ghost cell in the solid phase, the interpolation can be conducted first at an imaginary point in the fluid phase. Then, the solution of the ghost cells can be obtained from the interpolated value at the imaginary point and a known value at a solid surface in Figure 2.12.

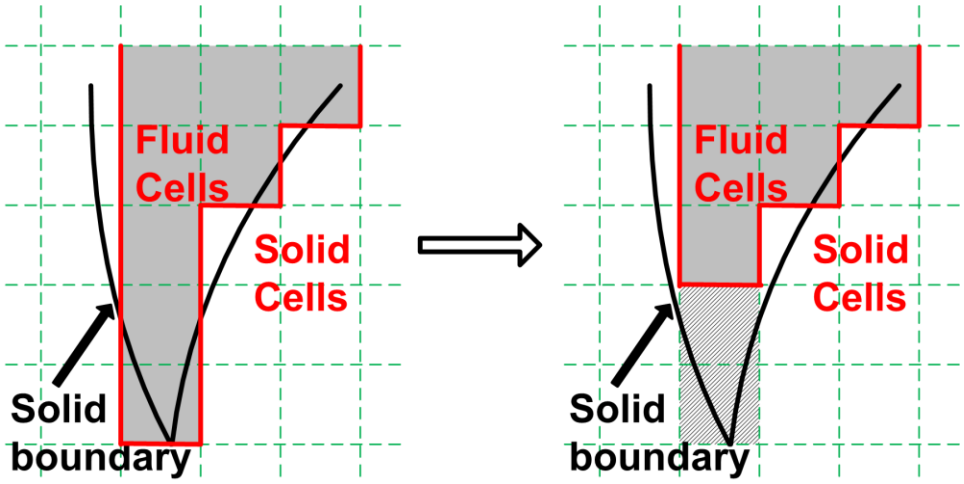

Figure 2.13: Identification of fluid and solid cells around sharp edge for the sharp interface method. The fluid cells should have enough neighboring fluid cells for defining appropriate ghost cells and interpolation scheme. The fluid cells in the sharp edge are treated solid cells.

In a complex solid geometry with sharp edge, the identification of ghost cells is challenging, and an incorrect definition of ghost cells results in an incorrect interpolation. In some cases, following the interpolation scheme results in large errors. Figure 2.13 shows an example of complex geometry, where fluid cells at the sharp tip cannot be solved since they don't have enough neighboring cells. Also, the ghost cell cannot get enough fluid cells for interpolation. For such an extreme case, the isolated fluid cells that do not have enough neighboring fluid cells are considered as solid cells in Figure 2.13. This treatment makes the present numerical method robust even with complex geometry.

2.5 Contact Line Treatment

When we consider a fluid-fluid interface intersecting a solid surface, treatment of the tri-junction locations, called the contact line, is required to account for the presence and interactions of all three phases, fluid-fluid-solid. One of the most discussed issues for modeling these contact lines with Navier-Stokes equations is that the imposed no-slip condition for velocity leads to a non-integrable singularity in stress. In the present research, the contact line force is imposed with local slip condition to overcome this singularity issue.

In Figure 2.14, the angle at the contact line can be used for representing the balance of forces resulting from intermolecular forces between solid, liquid and gas

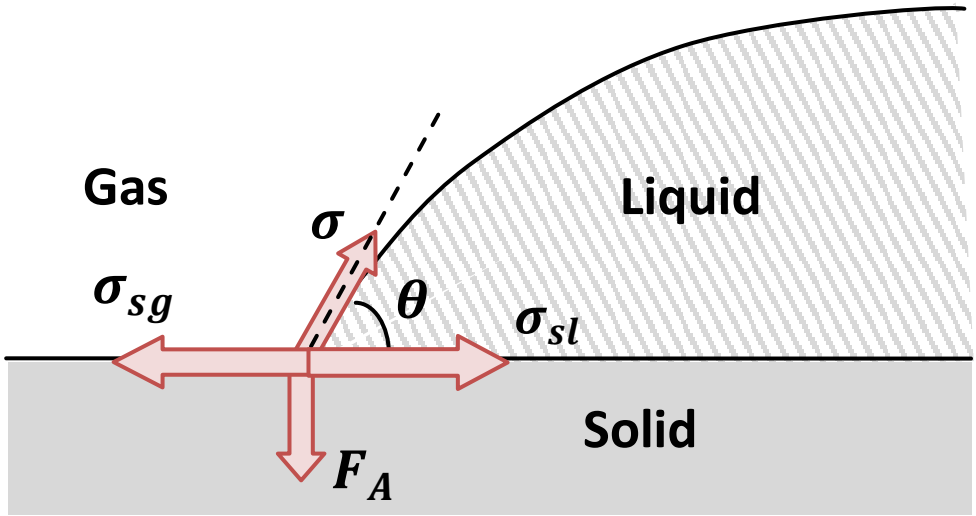

Figure 2.14: Forces at tri-junction (contact line) where, liquid, gas, and solid meets together at the same point in 2-D and at the same line in 3-D. F_A represents the adhesive forces.

phases. The tangential component of the resulting force at the contact line ($\mathbf{F}_R$) is shown in Eq. (2.25). In static equilibrium, Eq. (2.25) leads to the well-known Young-Laplace equation as given in Eq. (2.26).

$$\boldsymbol{F}_R = \sigma_{sg} - \sigma_{sl} - \sigma \cos\theta \tag{2.25}$$

$$\sigma_{sg} = \sigma_{sl} + \sigma \cos\theta_0 \tag{2.26}$$

In Eq. (2.26), σ_{sg} is the surface force due to the interaction of solid and gas; σ_{sl} is the surface force due to the interaction of solid and liquid; and σ is the surface tension defined between liquid and gas. The given static contact angle is represented by θ_0, and θ is the present contact angle at an instant. In this approach, the force at the contact line is obtained by plugging Eq. (2.26) into Eq. (2.25). This contact line force in Eq. (2.27) accelerates or decelerates flow fields, and makes the contact angle (θ) asymptotic towards a prescribed static contact angle (θ_0).

$$\boldsymbol{F}_R = \sigma(\cos\theta_0 - \cos\theta) \tag{2.27}$$

During the computation of the source term due to surface tension, the contact line region contributes as a recovery force in the tangential direction to the solid surface ($\mathbf{t_s}$) instead of the curvature effects given in Eq. (2.28). The contact angle is enforced on open edges where the element connects to either a computational boundary or a solid interface by modifying Eq. (2.24). The surface tension force from the interface curvature is applied to closed edges, and the contact line force is applied to open boundary edges.

$$\boldsymbol{\delta f} = \sum_{\substack{i=closed \\ edges}} \sigma\left(\boldsymbol{t}_f \otimes \boldsymbol{n}\right)_i \Delta s + \sum_{\substack{i=open \\ edges}} \sigma(cos\theta_0 - cos\theta)_i \boldsymbol{t}_s \Delta s \tag{2.28}$$

One of the difficulties in combining sharp interface methods with continuous interface methods in the same framework is lack of information during the transfer between Eulerian and Lagrangian quantities. The surface tension is smoothed into Eulerian fluid cells around the interface, and the fluid marker velocity is computed from around fluid cells via discrete Dirac delta function in Eqs. (2.19) and (2.21). The surface tension is computed easily in Eq. (2.28) by assuming an extended interface over the solid boundary, where the surface tension is zero since the curvature is also zero. For marker velocity computation in Eq. (2.19), we consider only the fluid region and conducted weighted averaging of Dirac delta function by Eq. (2.29).

$$\boldsymbol{U}(\boldsymbol{X}) = \frac{\sum_x \boldsymbol{u}(\boldsymbol{x})\, \boldsymbol{\delta}(\boldsymbol{X} - \boldsymbol{x})}{\sum_x \boldsymbol{\delta}\,(\boldsymbol{X} - \boldsymbol{x})} \tag{2.29}$$

In Eq. (2.29), the summation of the delta function in the denominator will yield unity (as a property of the delta function) further away from the contact line, whereas it is less than unity for markers in the proximity of a solid surface.

A local slip condition is applied around the contact line on solid boundary to simulate the moving contact line problems with better accuracy. The present model and solid boundary treatment work well with a no-slip condition for steady and/or slowly moving fluid interface problems. However, the no-slip condition imposed on the solid

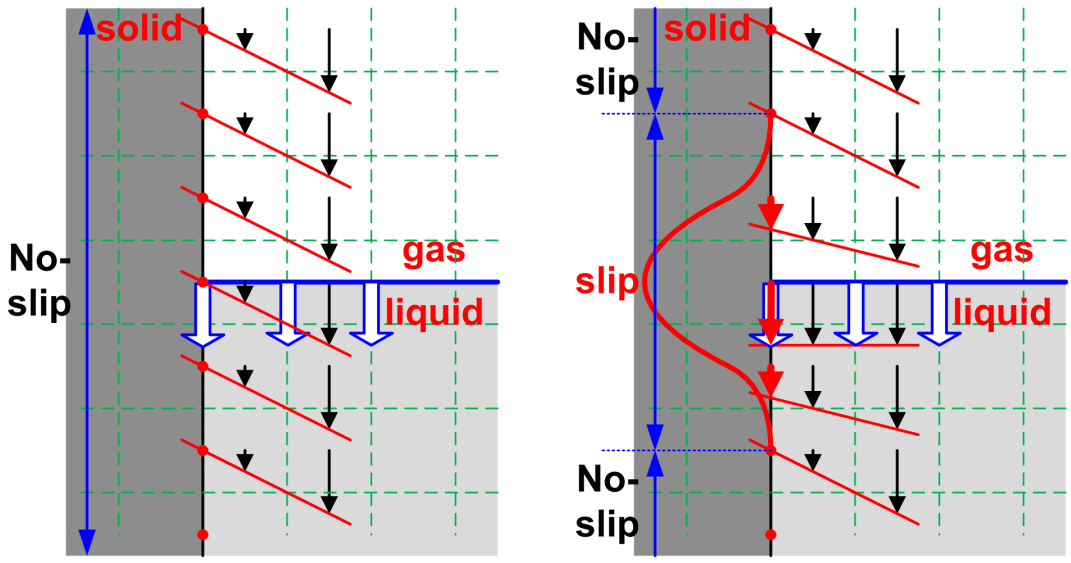

(a) **(b)**

Figure 2.15: The comparison of velocity fields between no-slip and local slip condition. (a) No-slip condition. (b) Local slip application around contact line.

leads to a non-integrable singularity in stress and retarded interface movement due to the discontinuous velocity fields in Figure 2.15(a). This singularity can be solved by applying a slip condition within a finite distance from the contact line using the Dirac-delta function in Figure 2.15. A perfect slip is applied exactly on the contact line, and a partial slip is within 2 cell distances as continuous fluid interface is diffused.

2.6 Mass Transfer Computation

Mass transfer computation is one of the key issues in the phase change process since it is related to the movement of the phase boundary and the amount of latent heat in the energy transfer process. In the energy equation Eq. (2.3), the latent heat is computed by Eq. (2.30), where $\dot{m}_f$ is mass transfer due to phase change and L is the latent heat.

$$Q_f = \int_\Gamma \dot{m}_f L \delta(\boldsymbol{x} - \boldsymbol{X}) d\Gamma \tag{2.30}$$

Similar to the transformation of surface tension, the latent heat of the interface due to phase change is also transformed from a Lagrangian quantity ($\boldsymbol{X}$) to an Eulerian quantity ($\boldsymbol{x}$) via the approximate discrete Dirac delta function, $\delta_h(\boldsymbol{x} - \boldsymbol{X})$.

In the present study, the mass transfer is computed in Eq. (2.31) based on the Stefan condition using the probe-based temperature gradient for simplicity in Figure 2.16.

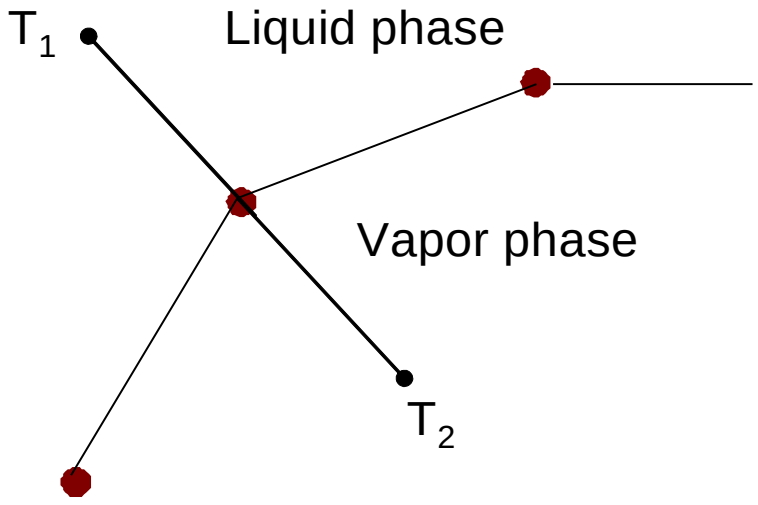

Figure 2.16: Probe-based temperature gradient computation for Stefan condition.

The interface temperature is assumed equal to the saturation temperature since it is an adequate assumption in macroscopic problems (Juric and Tryggvason 1998). The probe-length is the chosen cell distance (Δ), but 0.8Δ~1.3Δ gives no difference.

$$\dot{m}_f L = (q_2 - q_1) \cdot \boldsymbol{n} = -k_2 \frac{\partial T}{\partial n}\bigg|_2 + k_1 \frac{\partial T}{\partial n}\bigg|_1 \tag{2.31}$$

The energy equation of Eq. (2.3) is solved using continuous treatment with smoothed material properties in Eqs. (2.9)-(2.12), and the projection method in Eqs. (2.14)-(2.16) is applied to solve momentum equation. The mass conservation equation in Eq. (2.1) is coupled by assuming $\nabla \cdot \boldsymbol{u}^{n+1} = 0$ when we solve pressure Poisson equation in Eq. (2.17). However, the divergence of velocity is not zero around the interface if the phase change occurs and mass is transferred across the interface. Shin and Juric developed the conservation of mass in Eq. (2.32) (Shin and Juric 2002), and the modified Eq. (2.33) for the non-conservative form is implemented in the present work.

$$\nabla \cdot (\rho \boldsymbol{u}) = \boldsymbol{u} \cdot \nabla \rho + \frac{(\rho_2 - \rho_1)}{\rho_f} \int_{\Gamma(t)} \dot{m}_f \delta(\boldsymbol{x} - \boldsymbol{X}) d\Gamma \tag{2.32}$$

$$\nabla \cdot \boldsymbol{u} = \frac{1}{\rho}\left[(\rho_2 - \rho_1)\frac{\dot{m}_f}{\rho_f} \nabla I\right] = \frac{1}{\rho}\left[\frac{(\rho_2 - \rho_1)}{\rho_f} \int_{\Gamma(t)} \dot{m}_f \delta(\boldsymbol{x} - \boldsymbol{X}) d\Gamma\right] \tag{2.33}$$

2.7 Adaptive Grid

Multiphase flow problems involve multiple length scales. In order to effectively resolve the flow features in such cases, an adaptive grid based on isotropic refinement is implemented. The cells are split into four and eight equal sibling cells in two- and three-dimensions, respectively, in order to better handle regions that require higher resolution. The grid is represented using unstructured data that connects cells through cell faces. Figure 2.17 shows the implemented data structure for the storage of an isotropically refined Cartesian grid. For cell data structure, refinement *level* and *i, j, k* index are used cell-face lists. The level indicates how many times a cell has been split from the initial state. The *i, j, k* index provide the location and size of cells with the information of *level*. All faces forming a cell are stored to provide cell-to-face connectivity information. For each face, *orientation* indicates the normal direction of the face; 1, 2, and 3 are used for x-, y-, and z-direction, respectively. The *sidecell* information is also stored for referring cells sharing this face. The location and area of faces can be computed easily from sidecell information and face direction. The details of the data structure and algorithm can be found in many previous researches (Aftosmis 1997; Ham *et al.* 2002; Singh and Shyy 2007).

Adaptation is performed based on the flow solution quality for effective computation as well as the interface location. The geometry-based adaptation around interfaces allows better resolution in the near wall region and phase boundary. Near the fluid interfaces, for which discontinuous flow properties smear across two layers of cells, refinement is performed to improve the resolution and capture detailed flow structures more accurately. This fully resolved region around a fluid interface is further extended to

Cell Data
- Integer:: level
- Integer:: i, j, k
- Integer:: cell-face list

Face Data
- Integer:: orientation
- Integer:: sideCell1, sideCell2

(a)

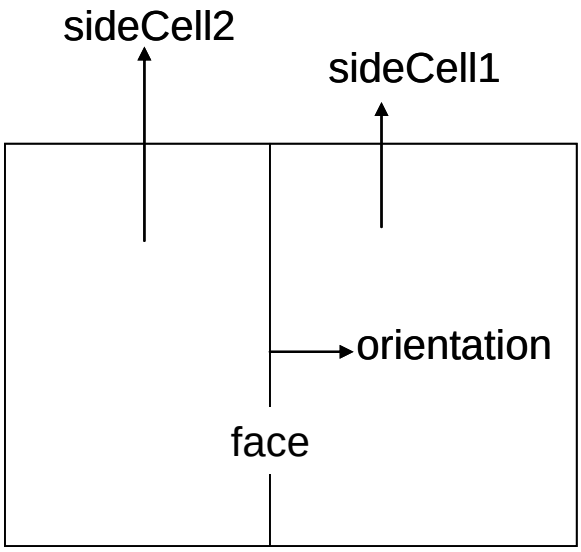

(b)

Figure 2.17: The unstructured data format for adaptive Cartesian grid. (a) The cell and the face data structure (b) An illustration of face data format.

six layers of cells to handle both the discrete Dirac function as well as a possibility for large deformation of the interface. On the other hand, solid interfaces, where interfacial dynamics are not smeared, triggers full refinement with two-cell layers from the wall. Figure 2.18 shows examples of geometry-based adaptation in a confined fuel tank and velocity- and temperature-solution based grid adaptation in a 2-D square natural convection case. The computational cells are dynamically refined based on the solution of the flow field. The present implementation uses a curl based adaptation criterion for velocity and gradient or divergence based criteria for temperature, comparing a cell value ξ_{cell} in Eq. (2.34) with a standard deviation of the whole domain (σ') in Eq. (2.35). The length scale l is estimated as the cubic root of cell volume. The decision to refine or coarsen a cell is defined in Eqs. (2.36) and (2.37).

$$\xi_{cell} \sim |\boldsymbol{\nabla} \otimes \boldsymbol{U}|^{l} \tag{2.34}$$

$$\sigma' = \frac{1}{N_{cell} \sum_i \xi_i^2} \tag{2.35}$$

$$\xi_{cell} > \sigma' \rightarrow Refine\ cell \tag{2.36}$$

$$\xi_{cell} < 0.1\sigma' \rightarrow coarsen\ the\ cell \tag{2.37}$$

During the adaptation procedure, the flow field variables at the Cartesian cell-center and face-center should be reconstructed for the newly created cells and faces. The cell-centered values such as pressure and temperature are reconstructed linearly while the face-normal velocities are reconstructed using divergence-free reconstruction (Balsara 2001). Flow variable reconstruction during cell and face coarsening is performed simply by averaging of the corresponding cell-centered or face-centered values.

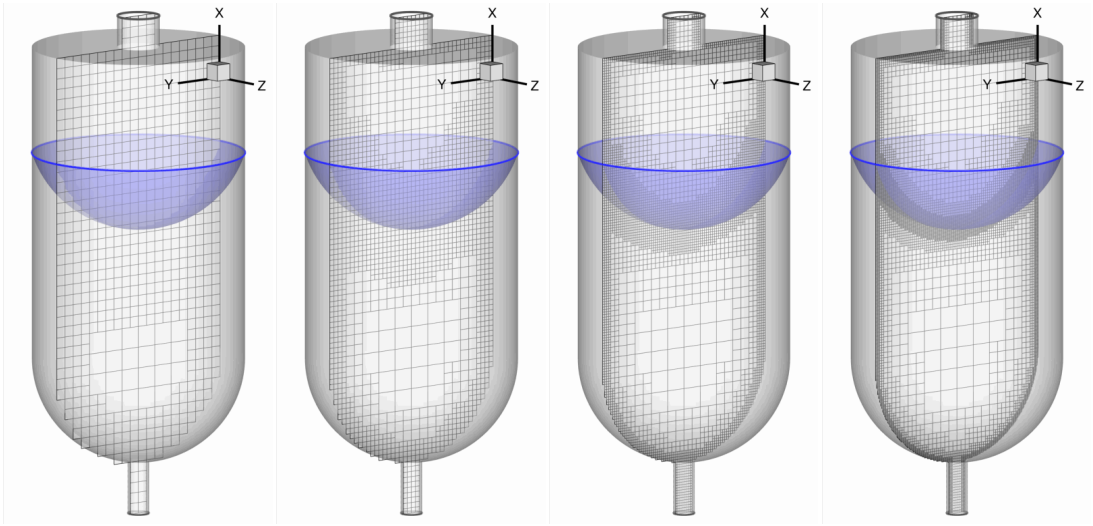

(a)

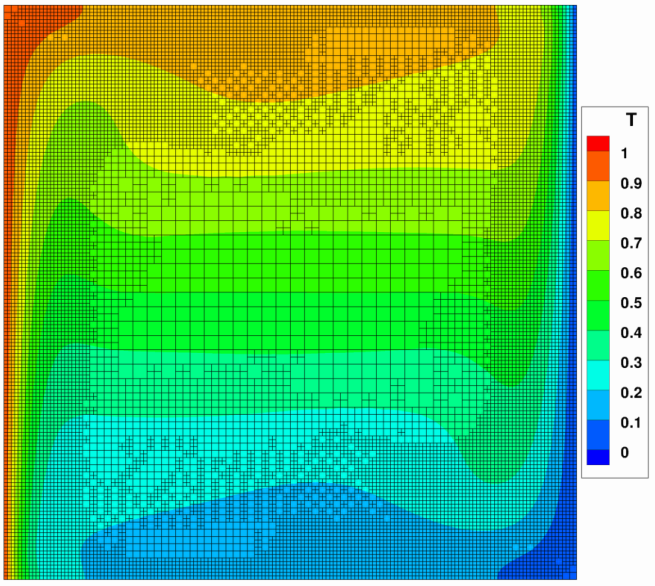

(b)

Figure 2.18: Examples of adaptive grids. (a) Geometry-based adaptation around liquid/vapor interface and solid fuel tank wall. (b) Velocity and temperature solution-based adaptation in a 2-D natural convection case.

2.8 Summary

In this chapter, the marker-based 3-D adaptive Eulerian-Lagrangian method has been described and further developed to perform incompressible interfacial flow computations, including phase change. The bulk flow variables are solved on the stationary (Eulerian) background grid, whereas interface variables are handled by moving (Lagrangian) surface meshes. A single fluid formulation for all fluid phases is implemented via smoothed material properties with the help of an indicator function. Interface is represented by massless markers and triangular surface meshes with connectivity information. The fluid interface is treated continuously for large-deformable phase boundary simulation, and the solid interface is treated sharply via ghost cell method for better accuracy. The contact line force model is proposed in order to enforce the moving contact angle. Geometry- and solution-based Cartesian grid adaptation is utilized for effective computation. The components of the numerical algorithm and their interactions are summarized in Figure 2.19.

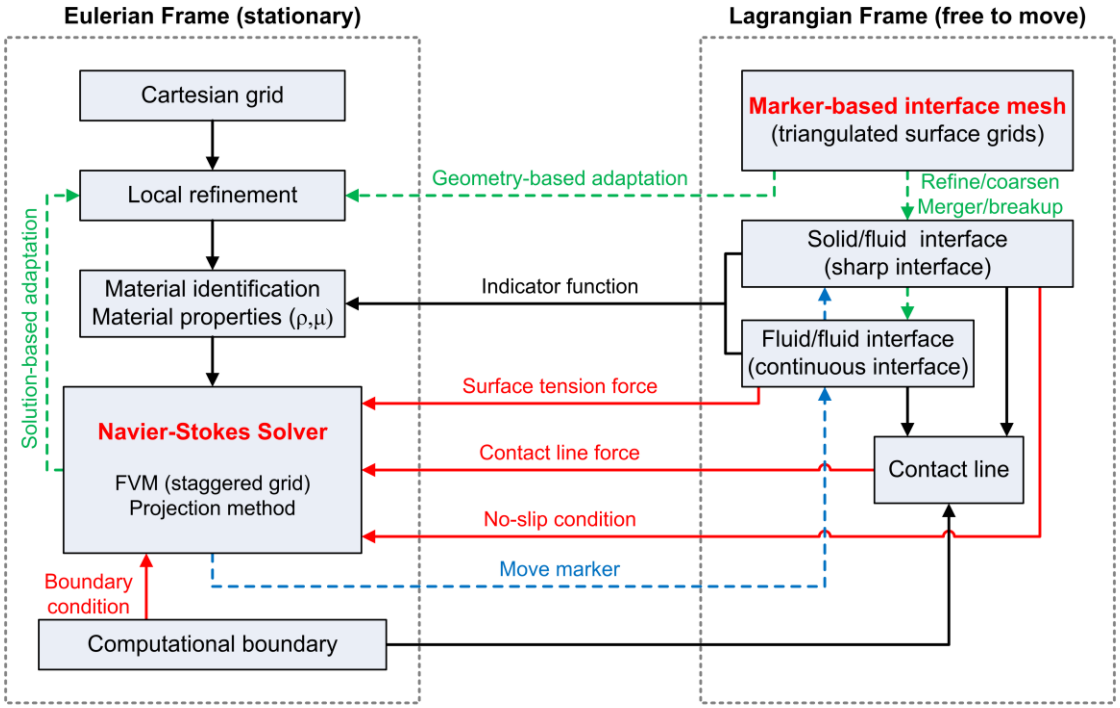

Figure 2.19: The summary of the present numerical method and the interactions between Eulerian and Lagrangian descriptions.

CHAPTER 3

ISOTHERMAL COMPUTATIONS

This chapter presents the results of the isothermal computation. In section 3.1, the implemented contact line force model is validated using a capillary tube computation with various contact angles. Section 3.2 discusses the liquid fuel draining dynamics of a spacecraft with different draining flow regimes under micro-gravity conditions. In order to simulate the influence of the engine shutdown within earth's orbit, section 0 examines the computation of the liquid sloshing motion under a sudden reduction of acceleration. Finally, section 3.4 examines the surface stability of liquid fuel under vertically oscillating gravitational accelerations, like rocket thrust oscillation.

3.1 Validation of Contact Line Force Model: Capillary Tube

For the purpose of this validation study of the implemented contact line force model, a capillary tube with an initially flat interface is simulated at zero-gravity condition, varying contact angles and non-dimensional parameters. The initial flat interface between gas and liquid is deformed into the curved steady interface shape with the given contact angle as the contact line force is applied to the tri-junction point between gas, liquid, and solid wall. The grid convergence and accuracy of various contact angles were first studied in axisymmetric domain. Then, 3-D simulations were conducted by representing the circular tube wall using solid interfaces with triangular elements in

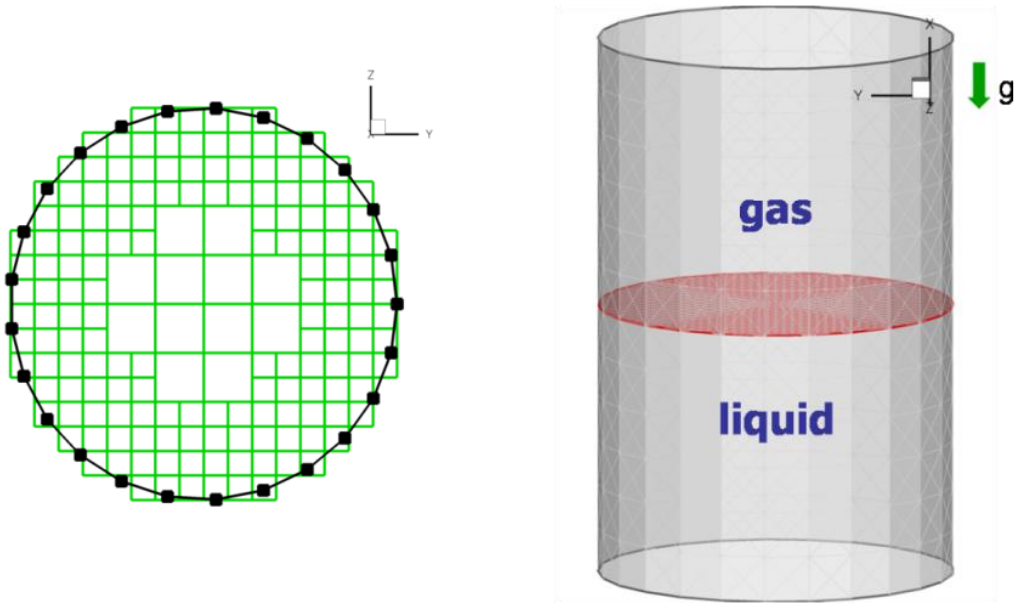

(a) **(b)**

Figure 3.1: The computational configuration for 3-D capillary tube simulations. (a) The tube wall is represented by sharp solid interface method, and the computational grids are adapted locally around solid boundary. (b) The fluid interface is assumed initially flat for validating the present contact line force model.

the adaptive Cartesian background grids. These configurations and initial flat interfaces in a capillary tube are shown in Figure 3.1. The density ratio and viscosity ratio are 1000 and 100 respectively. The Bond number, Bo $= \rho g L^2/\sigma$, is zero for the zero-gravity condition, and the Laplace number, La $= \rho\sigma L/\mu^2$, is varied from 10^2 to 10^5.

The height of a liquid column (ΔH), defined as the difference between a wall attachment point and a centerline location, is normalized by the radius of tube (R) and chosen for verifying the performance of the present contact angle model. Figure 3.2 shows the comparison between the analytical solution (Shyy 1994) and the present axisymmetric computation results with various contact angles from 0° to 180° at La =

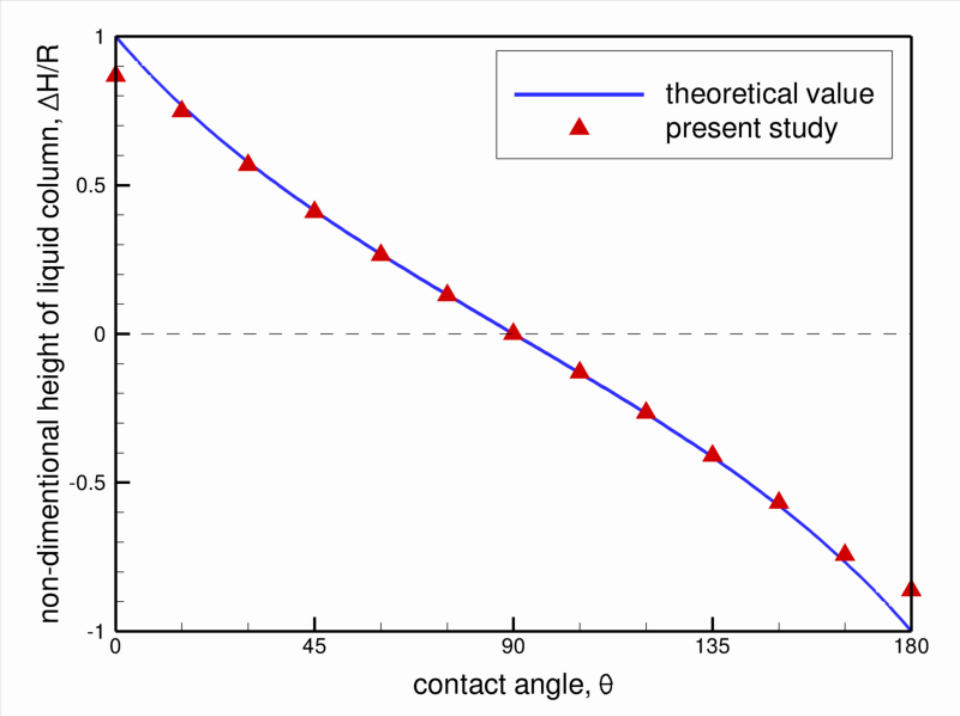

Figure 3.2: The comparison of the non-dimensional height of liquid column between theoretical values and the present numerical computation. The Laplace number La=10^4, and a maximum of 129 grid points are used along the radial direction.

10^4. A maximum of 129 grid points are used along the tank radius based on the grid convergence test. The current contact angle model works very well with various contact angles, and it demonstrates consistency with theoretical values, especially from 15° to 165°, where the difference is less than one cell distance.

In order to validate the 3-D performance of the contact angle and the solid interface, the 3-D capillary tube geometry in Figure 3.1 was tested with various Laplace numbers. At the same grid resolution, the 3-D computation has the same accuracy as the 2-D, where the interface location is tracked with an accuracy of one cell distance. The change in the wall attachment point at 30° contact angle is tracked in time from the initial

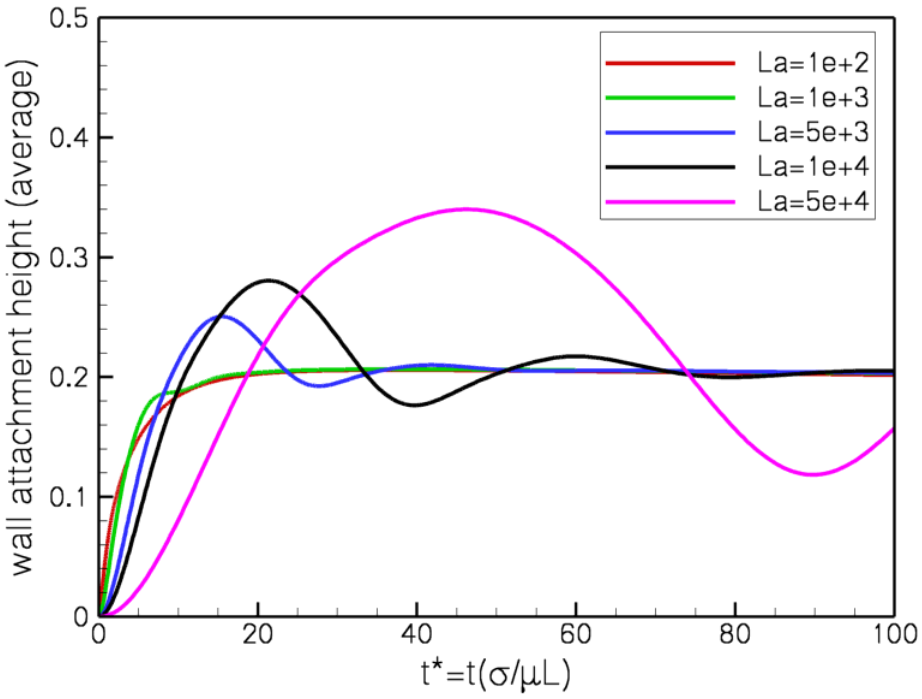

Figure 3.3: The wall attachment point of 3D Capillary tube with 30^{o} contact angle. The Laplace number varies from 100 to 50,000.

flat interface shape to the final steady state in Figure 3.3. With a modest Laplace number, for example, $La = 100$, the interface shape evolves smoothly without overshooting, but a large Laplace number can cause oscillations in interface shapes before it reaches the steady state solution because the relatively large surface tension and small viscosity create a larger contact line force, and thus movement. Figure 3.4 shows the 3-D sample snapshot of the deformed interface shape for the given contact angles 30, 90, and 150°. The Cartesian grid is adapted locally and dynamically in order to resolve interfacial dynamics and track the interface effectively.

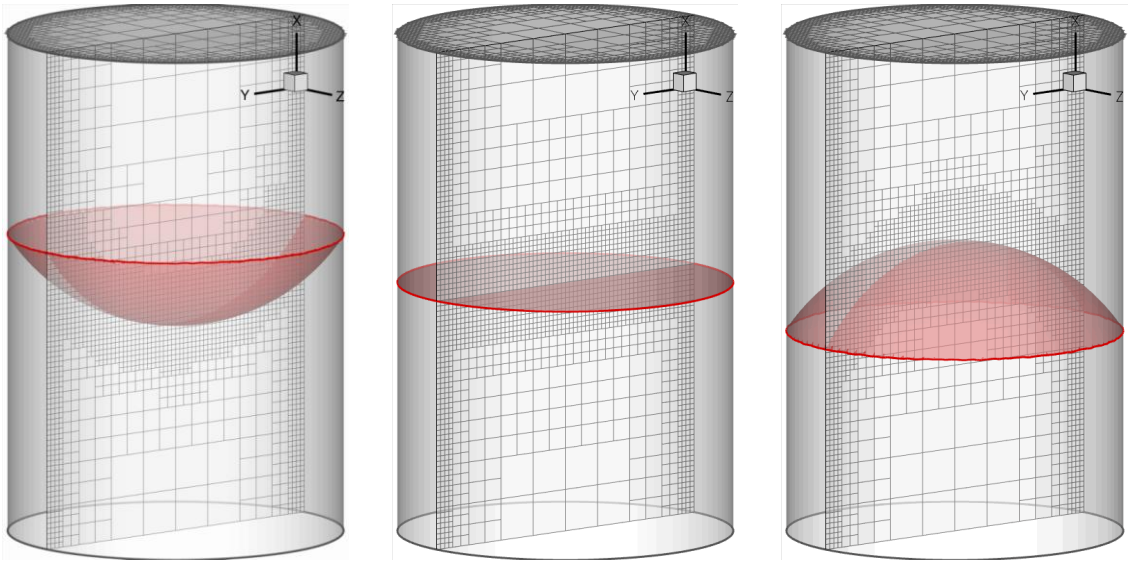

(a) θ = 30° **(b) θ = 90°** **(c) θ = 150°**

Figure 3.4: The steady interface shape of 3D capillary tube for different contact angles. (a) θ = 30° (b) θ = 90° (c) θ = 150°

3.2 Liquid Fuel Draining Dynamics in a Spacecraft

The dynamics of the fuel delivery under microgravity are studied numerically and compared with an experimental study conducted by Symons at the zero-gravity facility of the NASA Lewis research center (Symons 1978). Figure 3.5 shows the experimental and numerical configuration. The tank with hemispherical bottom and a small draining hole is represented by a solid interface treatment on the stationary Cartesian grid. In the experiment, the inlet baffle (or pressurizing gas diffuser) of 1/2 the tank radius is installed to prevent direct impingement of the pressurizing gas onto the liquid fuel surface. It is known that the inlet baffle minimizes the interface distortion (Nussle et al. 1965). This

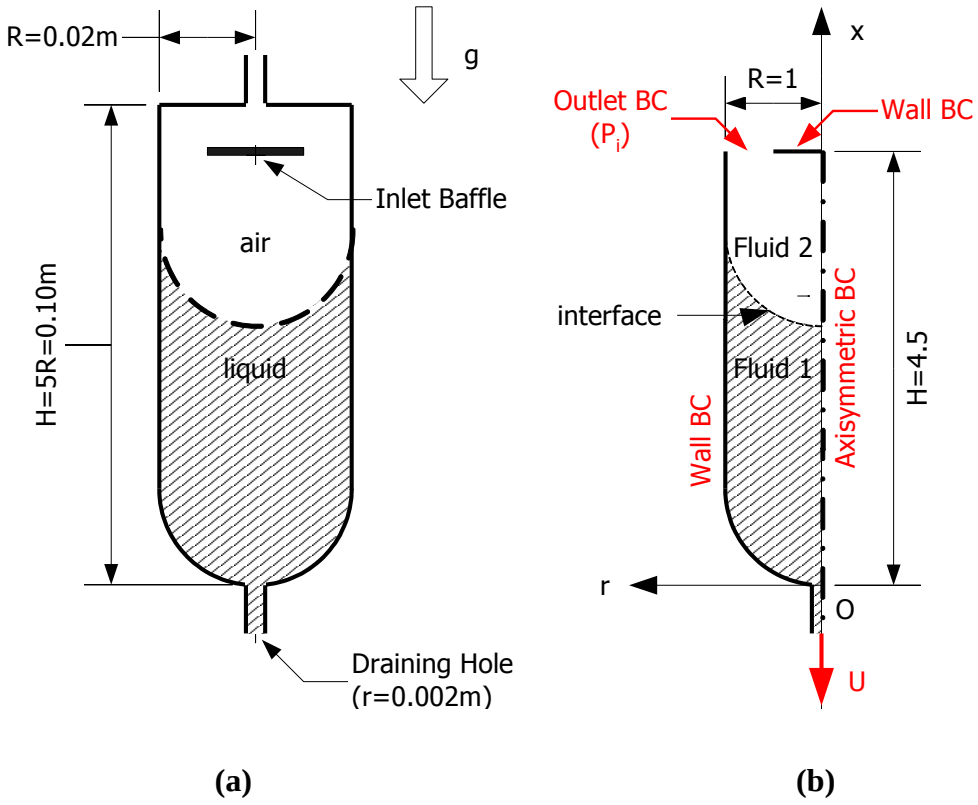

Figure 3.5: The geometry configuration of liquid fuel tank draining simulation. (a) Experimental setup. (b) The present numerical study.

Table 3.1: The material properties of trichlorotrifluoroehhane and air at 20°C (Symons 1978).

material properties at 20°C	trichlorotrifluoroehhane (liquid)	air (gas)
density [kg/m^3]	1.58×10^3	1.205
viscosity [kg/m·s]	0.70×10^{-3}	1.821×10^{-5}
surface tension [N/m]	0.0186	

equipment is modeled numerically by a mixed wall and an outlet boundary condition at the height of the inlet baffle. The non-dimensional initial liquid height, based on tank radius (R), is set to $2R$ or $3R$.

In Symons' experimental study, the draining phenomena was measured after some transition time from normal gravity (g_0) to the required microgravity ($0.015g_0$) condition with an equilibrium interface surface. The simulation is started from the end of the transition time, using the initial equilibrium ellipsoidal interface shape. The specified mass flow rate is used except in one case, which is used for a more accurate comparison with the experimental data. As is done in the experiments, trichlorotrifluoroehhane is utilized as a substitute for liquid fuel, and air is employed as a pressurizing gas. The material properties at 20°C are given in Table 3.1.

The non-dimensional parameters, the Weber number (We), the Bond number (Bo), and the draining parameter (λ), are defined with non-dimensional time (t^*) to compare the results with the experiment and to distinguish the flow regime under microgravity in equations (3.1)-(3.4).

$$We = \frac{\rho_l V_{ref}^2 L_{ref}}{\sigma_l} = \frac{\rho_l Q^2}{\pi^2 \sigma R^3} \quad \textbf{(3.1)}$$

$$Bo = \frac{We}{Fr} = \frac{\rho_l g R^2}{\sigma} \quad \textbf{(3.2)}$$

$$\lambda = \frac{We}{Bo + 1} \quad \textbf{(3.3)}$$

$$t^* = \frac{tQ}{\pi R^3} \quad \textbf{(3.4)}$$

where t is dimensional time, Q is the volume flow rate of the fuel draining, and R is the characteristic length of the fuel tank. In this study, the radius of tank is taken for the characteristic length, as presented in Figure 3.5. According to Symons, the flow characteristics of the draining process can be classified into three main categories: inertia-dominated, transition, and capillary-dominated regimes. In the present study, the Bond number is fixed at 5 with $g = 0.015g_0$, and various Weber numbers are chosen from 0.1 to 80 for characterizing each regime in terms of sloshing waves and residual volume. They correspond to draining parameters λ of 0.01667 to 13.33.

Direct simulation is conducted for a transition regime case corresponding to the draining parameter $\lambda = 0.16$, for which the experimental results are available. It should be noted that Symons quantified the draining parameter based on the mass flow rate measured under normal gravity (Symons 1978). However, these measured flow rates will be acceptable only if the pressurizing air pressure is much higher than the hydrostatic pressure of the liquid. This occurs in the inertia-dominated regime, where large flow rates require high air pressurizing. The difference of hydrostatic pressure between normal and

micro gravity conditions cannot be ignored in capillary-dominated or transition regimes with small air pressurizing; it can cause errors in the measured flow rate. In order to establish an exact basis for comparison, a procedure similar to the experiment is conducted by measuring the air pressure numerically for a given mass flow rate under normal gravity. Then, the obtained air pressure is used in a fuel draining simulation under microgravity.

In this preliminary test, the reported draining parameter $\lambda = 0.18$ in the experiment practically corresponds to 0.16 with 10% errors due to hydrostatic pressure differences. Thus, Figure 3.6 compares the simulation, which has a draining parameter of 0.16, with the experimental data, which has a draining parameter of 0.18. The figure also shows the non-dimensional height variation at the centerline and at the tank wall. Contrary to the draining phenomenon under normal gravity, the fuel surface goes down with different velocity at the centerline and wall with varying downward speeds. This results in a jellyfish-like sloshing motion that repeats flat and elongated surfaces. The present study consistently agrees with Symons' experimental study (Symons 1978). The sloshing motion and sudden vapor ingestion phenomena are captured in detail, whereas the wall contact point location is slightly different in the beginning of the draining process, possibly as a result of differences in the initial conditions.

Under normal gravity, the liquid fuel in a tank goes down and maintains a flat interface shape during the draining process. Thus, the fuel can be used efficiently with little left over. However, the liquid fuel interface shows a very large distortion under microgravity conditions, since the small gravitational force does not flatten the liquid

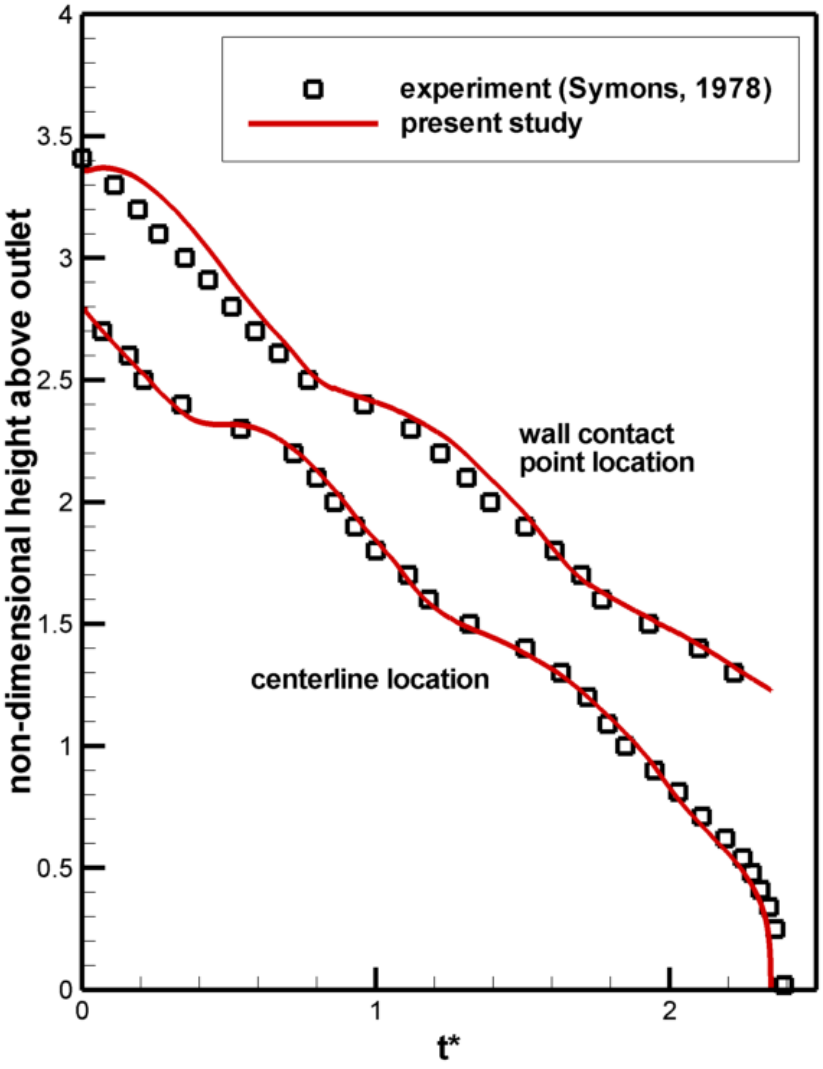

Figure 3.6: The comparison of the present simulation results with experimental data by Symons (Symons 1978).

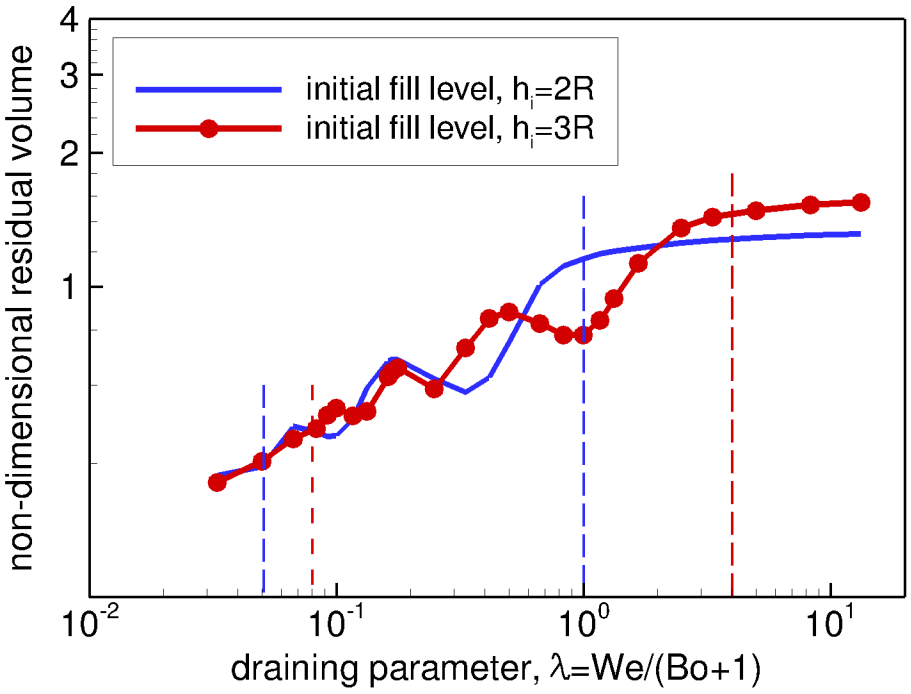

Figure 3.7: The present numerical measurement of non-dimensional residual volume in draining parameter.

surface. Rather, the balance of interfacial force and gravitational force determines the fuel surface shape. In this condition, the amount of usable fuel depends on the interface surface shape. Residual volume is defined as the remaining liquid volume in a tank at vapor ingestion, and thus, it informs us how much fuel can be used at the given condition. Figure 3.7 shows the non-dimensional residual volume V_r^* normalized by the hemispherical bottom volume for two different initial fill levels: 2 tank radii and 3 tank radii. The residual volume increases with the draining parameter until it reaches a certain value. At that point, it becomes insensitive to any changes in the draining parameter. With intermediate draining parameters, the residual volume shows oscillations due to the

influence of sloshing waves. If a slosh wave is at its highest point at the incipience of vapor ingestion, the vapor ingestion is postponed, and this results in a decreased residual volume. The phase of the slosh waves determines the time of vapor ingestion, which in turn determines the remaining liquid residual volume. Thus, a higher initial fill level does not guarantee longer engine operation since vapor ingestion can occur earlier than with a lower initial fill level. The existence of three regimes can also be shown: a linear part with a small draining parameter, an oscillation part in the middle range, and the flat residual volume part with a high draining parameter.

The time history of the non-dimensional height at the centerline and at the wall attachment point is shown in Figure 3.8 for the mentioned regime conditions. A capillary-dominated regime is characterized by many slosh waves with small magnitudes. In this regime, the fluid level decreases with the same velocity, both on the centerline and wall; simultaneously, it maintains its initial interface shape due to dominating capillary forces. The transition regime shows a few slosh waves with large amplitudes. The only sloshing wave observed in Figure 3.8 for the transition regime may not even be observed for smaller initial fill levels due to the short draining time. In the inertia-dominated regime, the wall attachment point rarely moves; however, the interface at the centerline moves down with a constant velocity until vapor ingestion occurs. This regime is observed for large draining parameters and causes a larger residual volume at the time of vapor ingestion because of the almost stationary wall attachment point.

Detailed interface shapes at different time steps are presented in Figure 3.9 for each regime. Figure 3.9(a) represents capillary-dominated regime for which the interface maintains its initial shape and moves with an almost-constant velocity until vapor

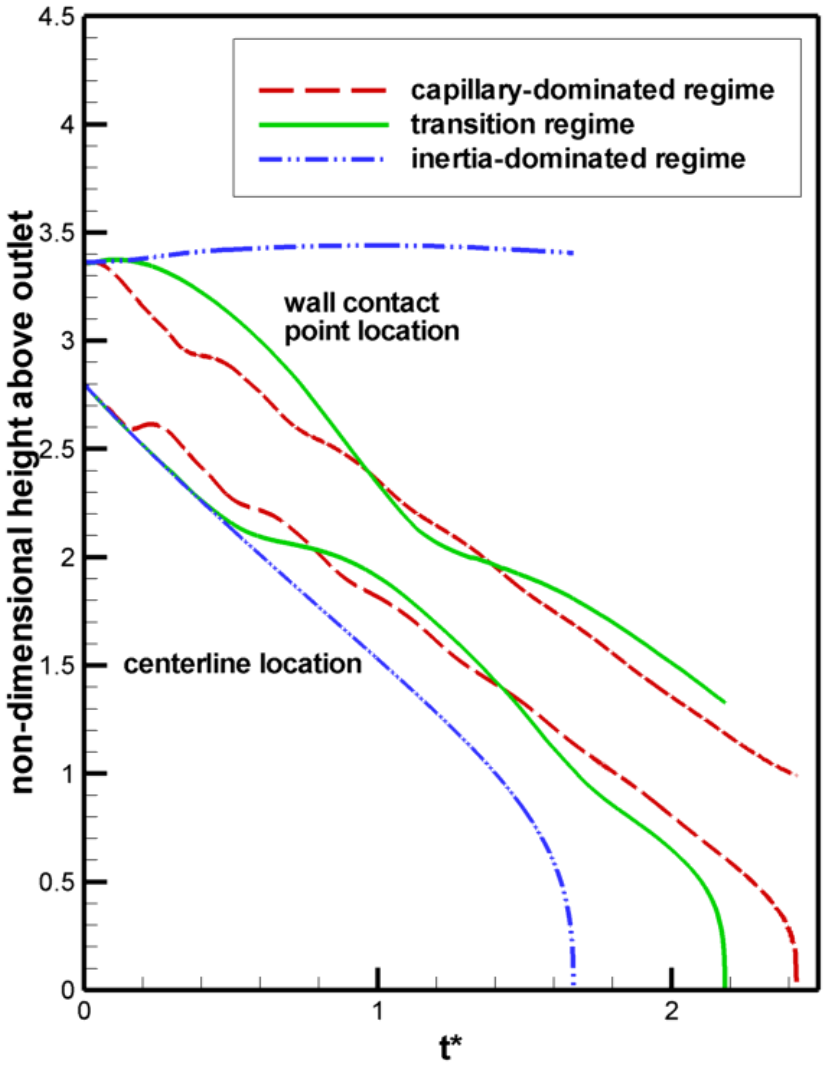

Figure 3.8: The present numerical measurement of non-dimensional height at the centerline and on the tank wall at capillary-dominated (We/(Bo+1) = 0.03), transition (We/(Bo+1) = 0.3), and inertia-dominated regime (We/(Bo+1) = 13.3). Initial fill level is 3 tank radii.

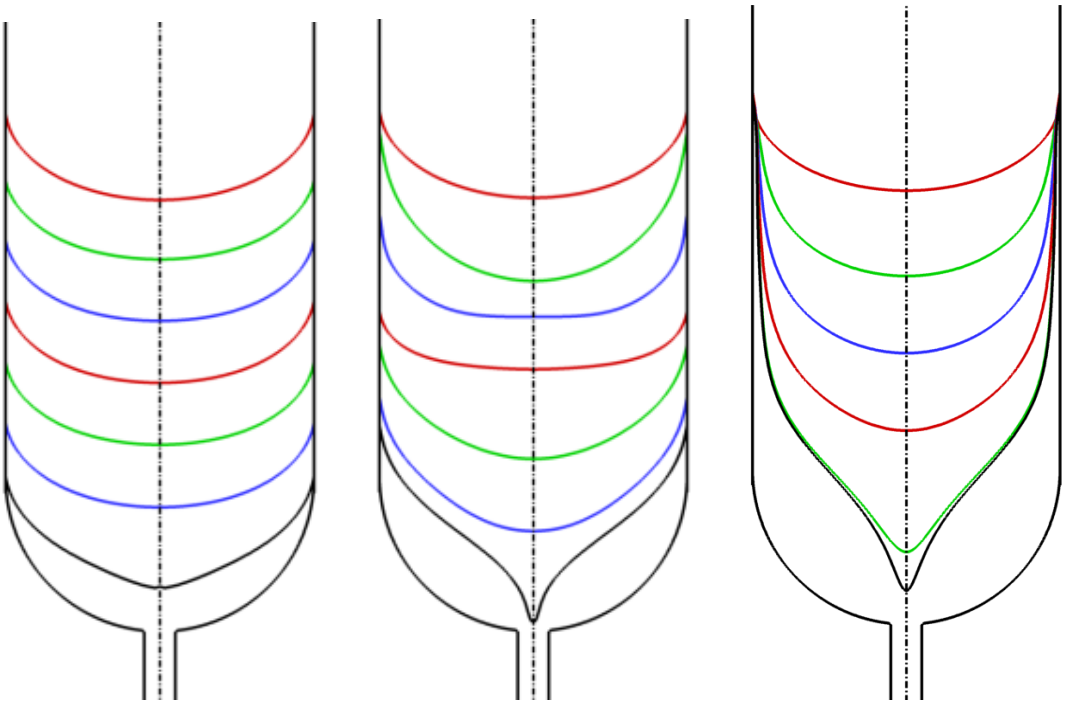

(a) **(b)** **(c)**

Figure 3.9: The snapshots of the interface shape for each regime during the draining process. (a) Capillary-dominated regime (We/(Bo+1) = 0.03), (b) Transition regime (We/(Bo+1) = 0.33), (c) Inertia-dominated regime (We/(Bo+1) = 13.33)

ingestion occurs. The transition regime with large-amplitude slosh waves is shown in Figure 3.9(b). The interface heights at the centerline and at the wall attachment point move at different speeds when compared with the capillary-dominated regime. Consequently, the interface tends to vary between curving up and flattening out as illustrated in Figure 3.9(b). In an inertia-dominated regime, the draining happens significantly around the center of the tank, yielding a constant velocity at the centerline as a result of weak capillary forces being unable to pull up/down the other regions of the surface. As a result, an elongated interface shape with an almost fixed wall attachment point is observed, as shown in Figure 3.9(c).

The non-dimensional period of slosh waves, T^*, is investigated for various draining parameters in Figure 3.10, where the inertia-dominated regime is omitted since waves do not exist for that regime. The wave period increases with the draining parameters from the capillary-dominated regime to the transition regime. In a capillary-dominated regime, waves have a small period and magnitude. The amplitude of waves becomes bigger as the draining parameter increases yielding large, noticeable waves with larger wave periods in the transition regime. As shown in Figure 3.10, such behavior is consistent with the single data point obtained by the experimental study of Symons (Symons 1978). Due to present experimental limitations of operation time under microgravity facility, no additional experimental data relevant to the wave period are available for further comparison. The present numerical study shows an almost linear correlation between the non-dimensional wave period and the draining parameter.

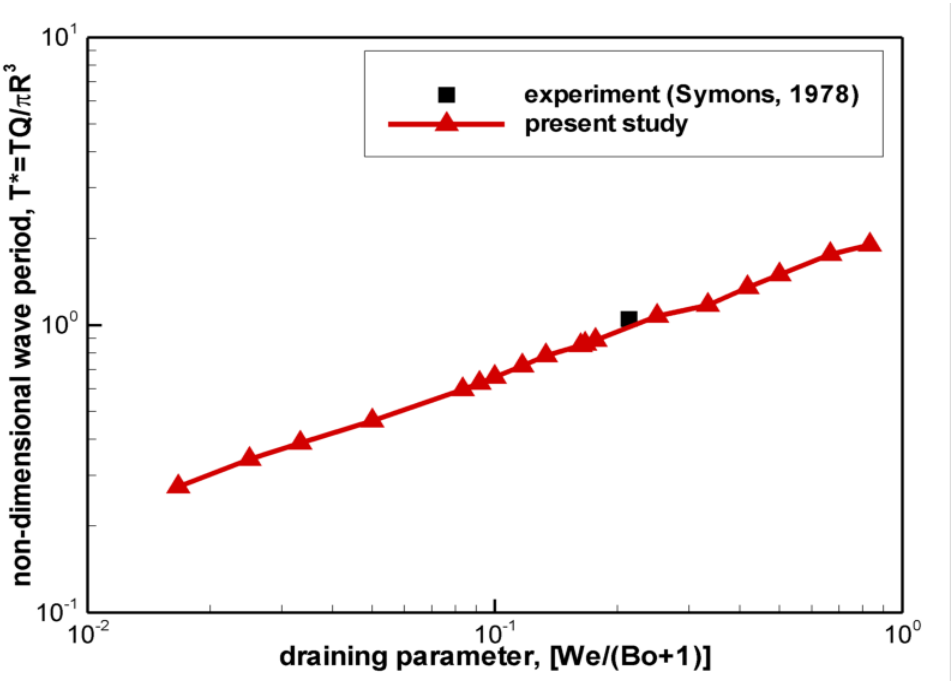

Figure 3.10: The present numerical measurement of non-dimensional wave period in a fuel tank with draining parameter.

3.3 Liquid Fuel Sloshing under Varying Acceleration

Figure 3.11(a) shows the configuration of the scale model of the Saturn V/S-IVB liquid hydrogen tank experimented by Toole *et al*. (Toole and Hastings 1968). To conduct 3-D flow computations in a concave-shaped tank on stationary Cartesian grids, triangular surface meshes are used for representing solid tank walls and fluid phase boundary in Figure 3.11(b). Petroleum ether and air are utilized as a substitute of liquid fuel and pressurizing gas respectively as is done in the experiment. The properties of petroleum ether at 21℃ are given in Table 3.2.

Table 3.2: Material properties of petroleum ether at 21℃ (Toole and Hastings 1968).

density	6.382×10^{2} kg/m^3
viscosity	2.489×10^{-4} kg/m·s
surface tension	1.490×10^{-2} N/m

Based on this experimental investigation, a test case with Bo=24 and Fr=14.6 is chosen to assess our computational modeling performance. These values correspond to an acceleration level of $0.01g_0$ and maximum fluid velocity of 0.33m/s. The acceleration history is shown in Figure 3.12. The key non-dimensional parameters are the Bond number and the Froude number, defined in Eqs. (3.5) and (3.6), which are related to the parameters in Eq. (2.2).

$$\text{Bond Number, } Bo = \frac{\rho a R^2}{\sigma} \tag{3.5}$$

$$Froude\ Number, \text{Fr} = \frac{V_{max}^2}{aR} \tag{3.6}$$

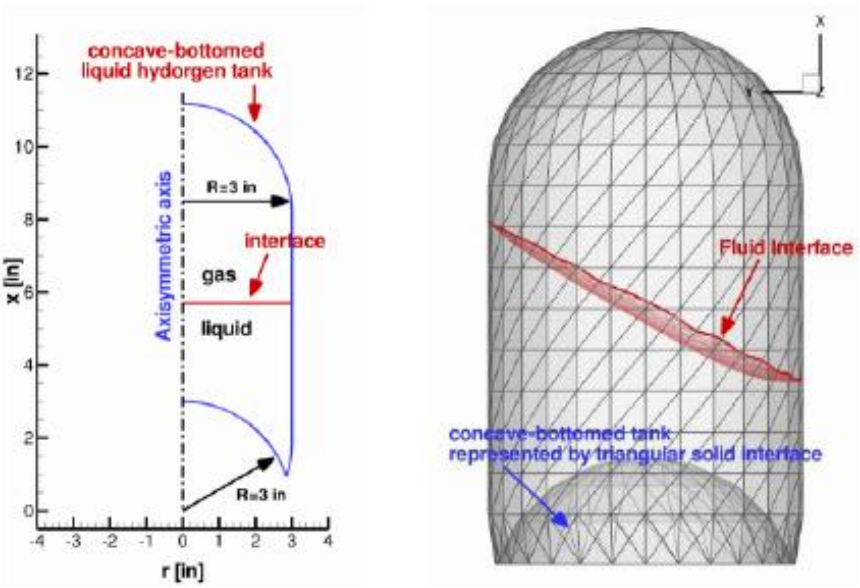

Figure 3.11: The geometry configuration of a liquid sloshing in a fuel tank with a hemispherical bottom. (a) Fuel tank geometry. (b) 3-D computational setup.

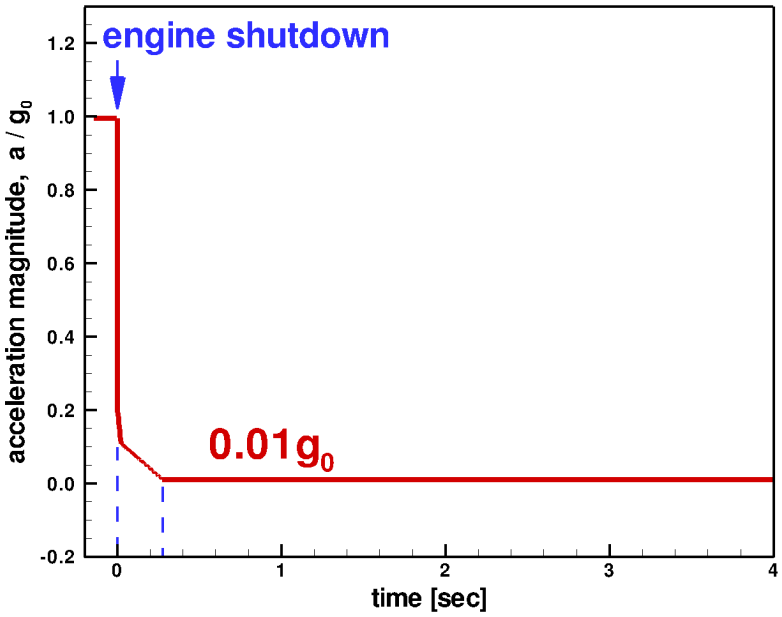

Figure 3.12: The acceleration history for simulation with engine shutdown at t=0. The acceleration decreases from normal gravity to micro-gravity ($0.01g_0$).

Because we do not have any information on the kinetic energy at a given interface shape, it is difficult to match the Froude number of the simulation with the experiment. There is no record that indicates the applied impacting force to make the initial sloshing motion. Therefore, drawing from the snapshot, we pick a free surface shape that has the highest wall attachment point. Then we adjust the acceleration time to match the Froude number and measure the maximum velocity of a wall attachment point by trial and error.

Figure 3.13 shows a comparison between the present computational results and the experimental results. Although Toole' snapshot started at t=-0.14sec, the simulation started at t=-0.12sec in order to match the given Froude number. The fluid motion is accelerated from the initial stationary position as the potential energy is converted into kinetic energy by the acceleration of normal gravity. At t=0.00sec, the acceleration suddenly reduced to $0.01g_0$ as described in Figure 3.12, and the high kinetic energy obtained at normal gravity is converted back into potential energy at micro-gravity. Smaller acceleration results in higher liquid fuel position to get the same potential energy level. The liquid fuel reaches and stays at the top of the tank for the time being, and then, it retracts and makes the second sloshing motion. The numerical study is not perfectly identical with the experimental study because the kinetic energy distribution is different due to different mechanisms that make the sloshing wave. However, the overall liquid fuel motion and wave period are nearly identical and demonstrate substantial agreement with the experimental results.

Figure 3.14 shows the change of the center of mass in time. The axial location plot indicates that the center of mass moves by 22% of the tank radius, and the sloshing waves damp very fast. In Figure 3.14(b), the z-directional change can be negligible as

expected, and the y-directional change is up to 46% of the tank radius. The large change in the center of mass requires excessive demand on the entire vehicle dynamics and control systems.

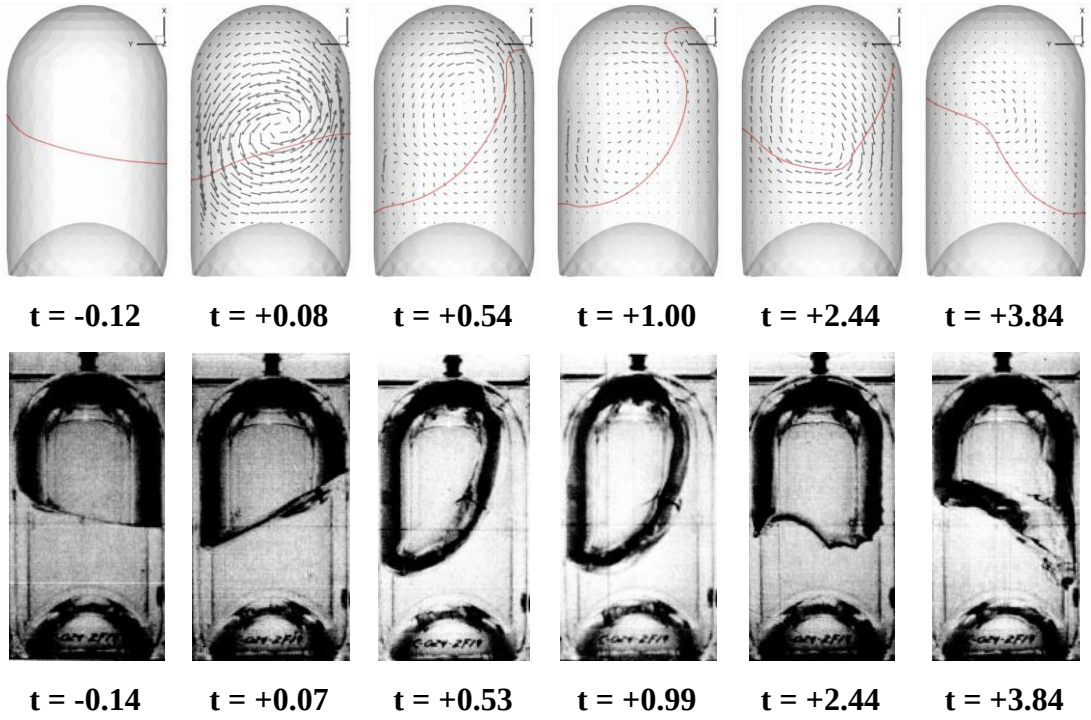

Figure 3.13: The comparison of the present sloshing fuel tank simulation (top) with experiment by Toole (bottom). The velocity vector and fluid surface are represented on a center-cut plane.

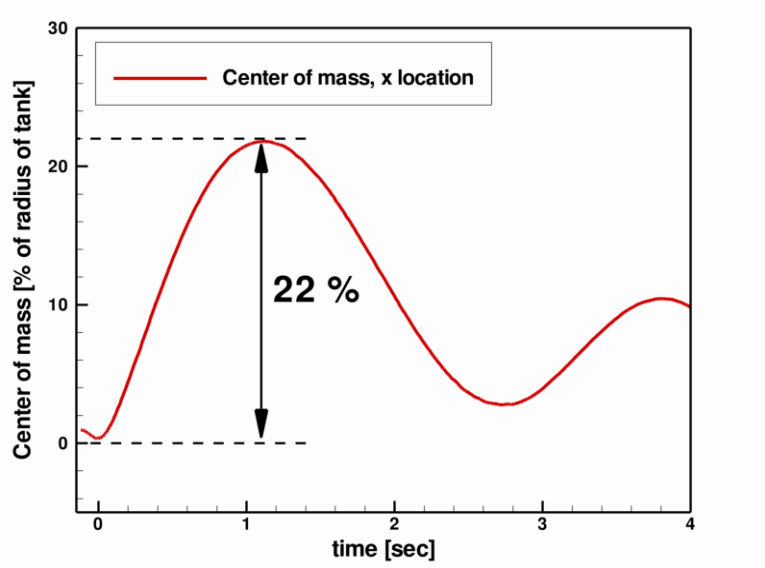

(a)

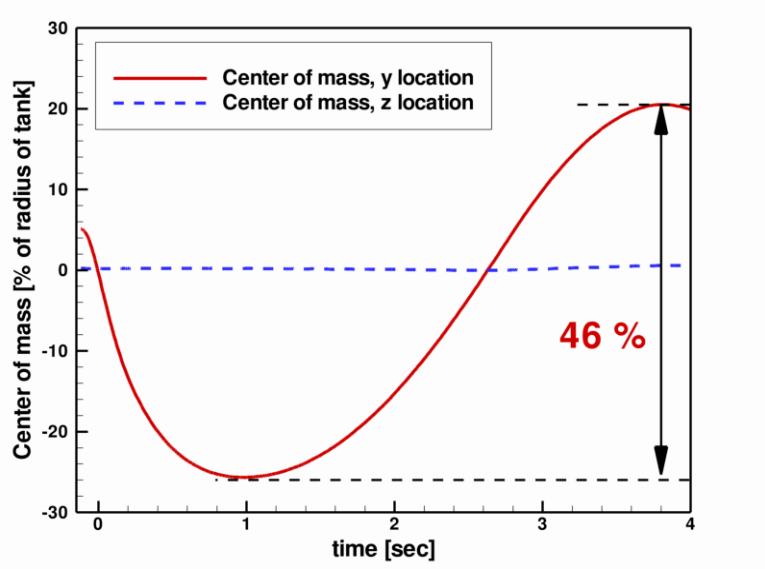

(b)

Figure 3.14: The numerical measurement of the center of mass of sloshing cryogenic fuel tank (a) Axial x-location. (b) Radial y and z-location.

3.4 Liquid Fuel Surface Stability under Thrust Oscillation

The influence of thrust oscillation on the liquid fuel tank is investigated. In a practical rocket system, thrust oscillation is composed of many different frequencies and magnitudes produced by different parts of the rocket (Yang and Andersen 1995). The present study focused on the parametrically excited liquid fuel surface wave, namely the Faraday wave where the vertical sinusoidal oscillation in Eq. (3.7) is applied to liquid/air in an open container, as depicted in Figure 3.15.

$$a = g_0(1 + \alpha \cdot sin(2\pi f t)) \tag{3.7}$$

where, g_0 is standard gravity, α is oscillation magnitude ratio, and f is forcing frequency.

According to the dispersion relation for infinite depth periodic waves in Eq. (3.8), the surface waves become unstable by restoring forces of either gravitational effects or surface tension effects (Landau and Lifshitz 1987).

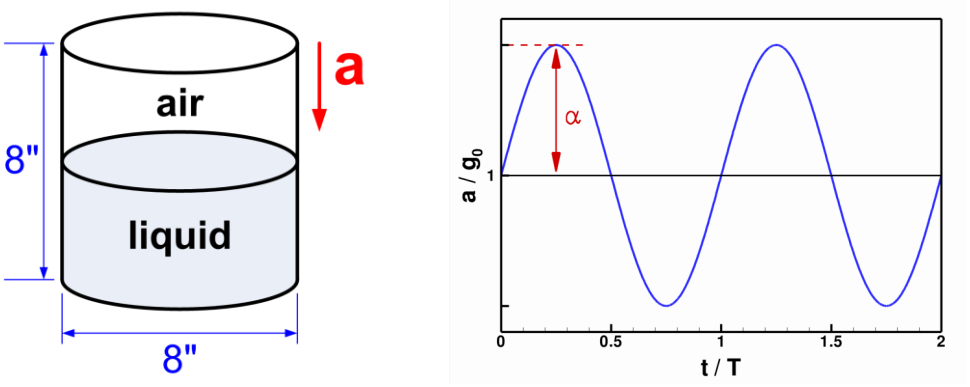

(a) **(b)**

Figure 3.15: The numerical configuration of parametrically excited Faraday waves. (a) 3-D geometric configuration of liquid/air in an open container. (b) Vertical sinusoidal acceleration.

$$\omega^2 = gk + \left(\frac{\sigma}{\rho}\right)k^3 \quad \textbf{(3.8)}$$

where ω is the angular frequency of the surface waves, g is the local acceleration, and k is the wave number. At a low wave number, the gravitational effect dominates; the surface tension effect dominates at a high wave number. The crossover wave frequency, $w_c = (4g^3\rho/\sigma)^{1/4}$, is determined from the crossover wave number, $k_c = \sqrt{g\rho/\sigma}$, where the effects are equal. When the liquid fuel tank is parametrically excited with forcing angular frequency $\omega_f = 2\pi f$, the energy is pumped into waves of angular frequency ω = $\omega_f/2$, ω_f , $3\omega_f/2$,… The non-dimensionalized forcing frequency and forcing acceleration are defined from the dimensional study in Eqs. (3.9) and (3.10).

$$\omega^* = \frac{\omega_0}{(\sigma/\rho)^2/\nu^3} \quad \textbf{(3.9)}$$

$$a^* = \frac{a}{(\sigma/\rho)^3/\nu^4} \quad \textbf{(3.10)}$$

Depicted in Figure 3.15, an open container with a depth of 8" and a diameter (or width in 2-D) of 8" is simulated to compare the present study with the experimental results conducted by Goodridge (Goodridge *et al.* 1996; Goodridge *et al.* 1997; Goodridge *et al.* 1999). Water and water-glycerin solutions with different viscosities are used to investigate the liquid surface stability. As is done in the experimental study, the contact angle between liquid and solid is assumed 0°. 2-D simulations are first conducted to check the overall tendency of stability due to their computational efficiency, and then 3-D cases are simulated for scaling analysis and comparison with the experiment.

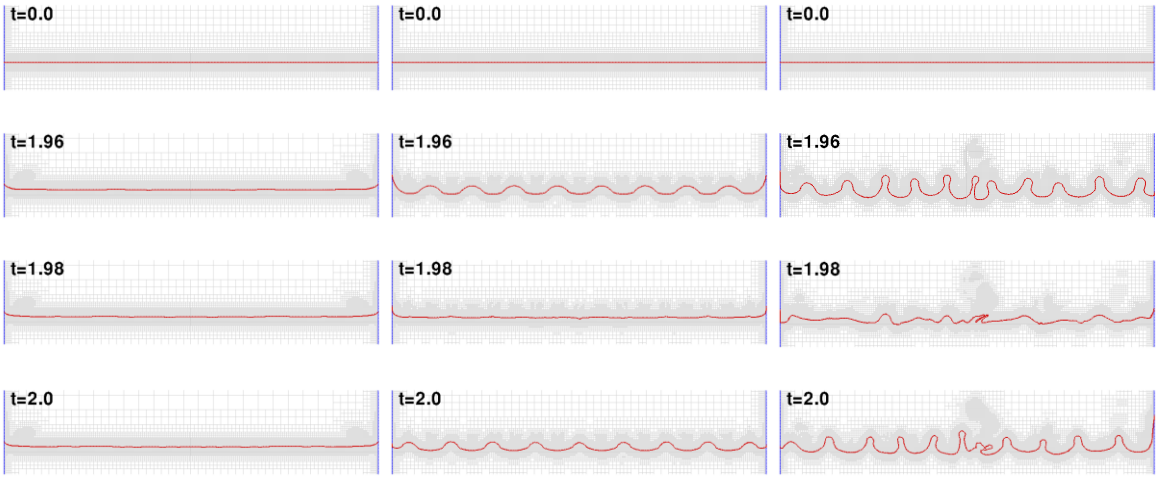

(a) **(b)** **(c)**

Figure 3.16: The features of surface wave stability as oscillation magnitude increases. Water/air fluids are vertically oscillated at a forcing frequency *f*=20 Hz. The flat liquid surface waves becomes periodic standing waves as oscillation magnitude increases, and shows the transition to unsteady aperiodic states with upward jets and droplets when the acceleration exceeds a certain threshold acceleration. (a) α=0.1 (b) α=0.5 (c) α=1.3

Figure 3.16 shows the 2D liquid surface wave evolution in time for water/air fluids as oscillation magnitude increases at a given forcing frequency $f = 20\,Hz$. With low acceleration, it shows a flat surface wave in Figure 3.16(a), but it becomes a periodic standing wave in Figure 3.16(b) as forcing acceleration increases. When the acceleration exceeds a certain threshold level, referred to threshold acceleration, the stable periodic surface waves are transformed to an unstable aperiodic state and show some upward jets in Figure 3.16(c). Goodridge (Goodridge et al. 1997) defined the threshold acceleration as the acceleration level where two droplets are detected within ten seconds. Das (Das and Hopfinger 2008), however, defined it as a jet forming or wave crest pinching off, followed by irregular motion. In this study, droplets or long filament-like jet formations are assumed as criteria for threshold acceleration because droplet formation itself in numerical studies may result in different criteria according to the grid resolution.

The influence of a fluid's viscosity on the threshold acceleration is investigated. Both water and 80% glycerin-water solution, which has a kinematic viscosity (ν) fifty times larger than water's, are considered. A higher kinematic viscosity makes the liquid surface waves more stable. This results in a higher threshold acceleration before aperiodic wave states appear with upward jets. Another feature of higher viscosity is creation of longer filament-like jets, as shown in Figure 3.17.

According to the dispersion relation for infinite depth periodic waves in Eq. (3.8), as the forcing frequency increases, the gravity effect is less important, and the capillary effect becomes more dominant. Figure 3.18(a) shows gravity waves at forcing frequency $f = 10Hz$, which is lower than the crossover forcing frequency ($f_c = 2\omega_c/(2\pi) = 27Hz$ in water/air case). It shows unsteady aperiodic states with a very large upward jet on the

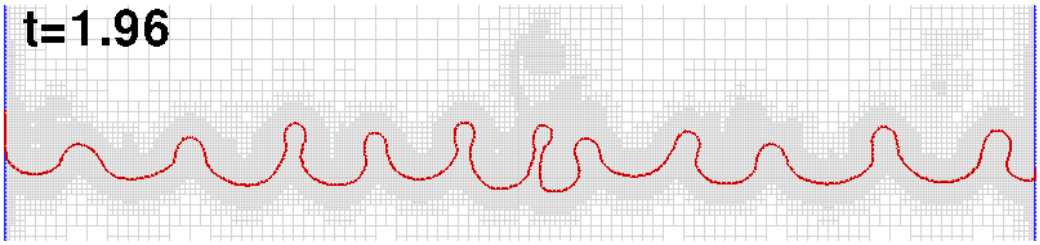

(a)

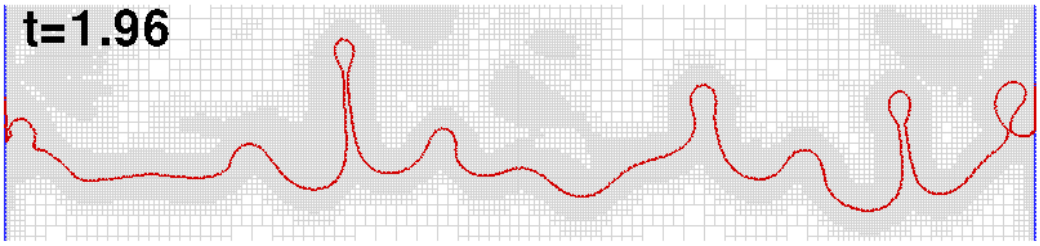

(b)

Figure 3.17: The effect of fluid viscosity at forcing frequency *f*=20 Hz. Higher viscosity of fluid shows longer filament-like jets with higher threshold acceleration. (a) Water with α=1.3 (b) 80% glycerin-water ($\nu = 50 \times \nu_{water}$) with α=2.3

centerline of the container. The transition from the gravity wave into the capillary wave is observed in Figure 3.18(b), where the large upward jet in the center of the axis does not exist, and smaller multiple jets are shown in multiple locations. It is noted that a higher forcing frequency results in a smaller wave length, and consequently smaller multiple jets. The grids are adapted dynamically, up to 200 grid points along the tank diameter, in order to capture the complex surface wave motions. We can find that 3-D computation capability with a fine grid is required to capture the capillary wave motions with multiple jets as shown in Figure 3.18(b).

The non-dimensional threshold acceleration ($a^* = a\nu^4/(\sigma/\rho)^3$) is plotted with non-dimensional angular forcing frequency ($\omega^* = \omega_f \nu^3/(\sigma/\rho)^2$) in Figure 3.19. Both 2-D and 3-D computations are in agreement with Goodridge's experiment. However, the 2-D simulation shows a slightly higher threshold acceleration than the 3-D simulation. The 2-D planar case requires more forcing energy to form upward jets since it needs to push up more mass than the 3-D. These result in higher threshold acceleration in 2-D. However, the overall trend matches very well. The non-dimensionalized threshold acceleration shows $(\omega^*)^{4/3}$ dependence for the lower-viscosity region ($\omega^* < 10^{-5}$), and $(\omega^*)^{3/2}$ dependence for the higher-viscosity region ($\omega^* > 10^{-5}$). This indicates that each region is dominated by different parameters. The correlation study on the dimensional parameters shows it clearly. For the low viscosity region, the threshold acceleration can be correlated by $a \sim (\sigma/\rho)^{1/3}\omega_0^{4/3}$ correlation, and thus the flow is dominated by surface tension and forcing frequency. For the high viscosity flow region, the viscosity itself and the forcing frequency dominate the surface stability by $a \sim \nu^{1/2}\omega_0^{3/2}$ dependence.

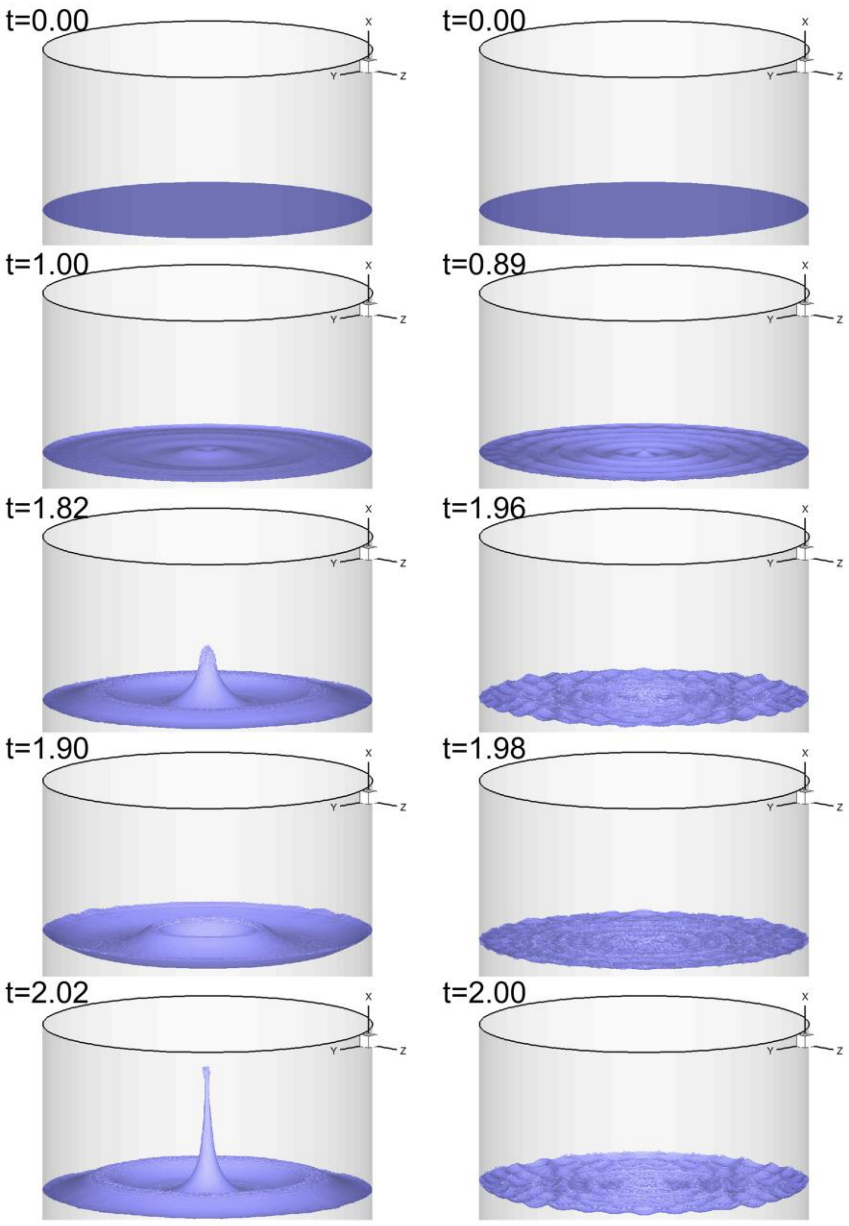

Figure 3.18: The comparison between gravity waves and capillary-transition waves in aperiodic surface states for water/air case. (a) *f*=10 Hz and *α*=0.3 (b) *f*=20 Hz and *α*=0.6

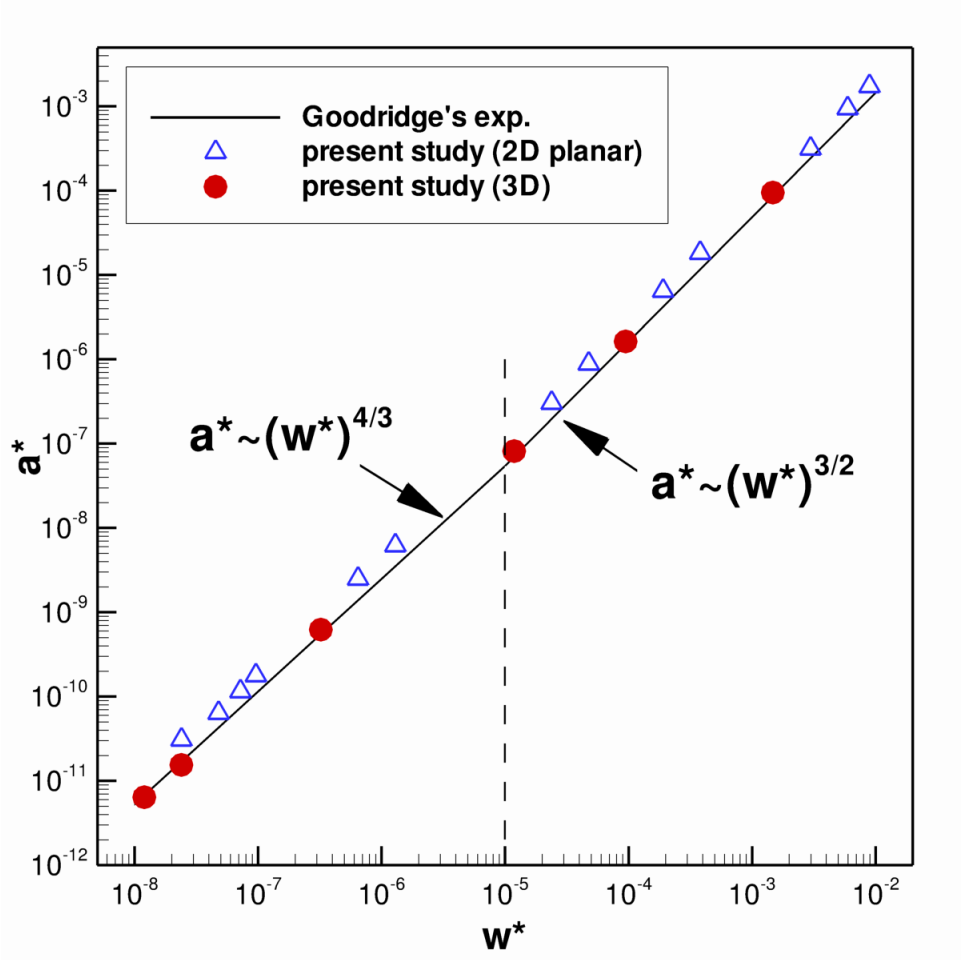

Figure 3.19: The non-dimensionalized threshold acceleration as a function of non-dimensionalized angular forcing frequency. Lower-viscosity region ($\omega^* < 10^{-5}$) and higher-viscosity region ($\omega^* > 10^{-5}$) show different correlation between a threshold acceleration and a forcing frequency.

3.5 Summary

In this chapter, isothermal multiphase flow computations are conducted using the 3-D adaptive Eulerian-Lagrangian method investigated in Chapter 2. The contact line force model is validated through a capillary tube simulation with various contact angles and Laplace numbers. This simulation is consistent with theoretical values especially from 15^o to 165^o. Three isothermal computations related to the draining, sloshing, and surface stability of liquid fuel in a spacecraft fuel tank are numerically performed, and the results agree well with the experimental observations. Specifically, the following are observed.

(i) Liquid fuel draining dynamics under microgravity

- Three different flow regimes are observed in the draining process under microgravity condition: a capillary-dominated regime, a transition regime, and an inertia-dominated regime.
- The liquid residual increases with oscillation as the draining parameter increases, and it remains almost constant at a large draining parameter.
- The non-dimensional slosh wave period increases with the draining parameter.

(ii) Liquid fuel sloshing under varying acceleration

- The reduction of acceleration transforms large potential energy at high acceleration into large kinetic energy because the potential energy is small at low acceleration and this results in a large sloshing motion in the fuel tank.
- The sloshing motions make large shifts in its center of mass, which can show significant influence on the vehicle dynamics.

(iii) Liquid fuel surface stability under vertical sinusoidal oscillation of acceleration

- As the forcing oscillation magnitude increases, the surface wave exhibits periodic standing waves, and reaches aperiodic unstable states with upward jets and droplets when the forcing magnitude exceeds a certain threshold value, namely the threshold acceleration.
- The threshold acceleration increases with the forcing frequency.
- As the kinematic viscosity of a fluid increases, the threshold acceleration increases with longer filament-like upward jets.
- As expected from the dispersion relation for infinite depth periodic wave, the gravity wave is observed when the forcing frequency is lower than the crossover wave frequency. The capillary-transition wave is observed as the forcing frequency increases.
- For lower viscosity fluids, the surface tension dominates the surface stability, and $a^* \sim (\omega^*)^{4/3}$ scaling is observed from both Goodridge's experiment and the present simulations.
- For higher viscosity fluids, the viscosity becomes an important parameter, and $a^* \sim (\omega^*)^{3/2}$ scaling is observed from both Goodridge's experiment and the present simulations.

CHAPTER 4

THERMO-FLUID TRANSPORT COMPUTATIONS

In this chapter, the present approach to thermo-fluid transport and the phase change model are validated along with the sharp solid interface method. In section 4.1, the implemented energy equation is tested using laminar natural convection flow, which is driven by the buoyancy force, varying Rayleigh number and the solid interface configuration. Section 4.2 illustrates the validation of the phase change model using 1-D two-phase Stefan problems with various material properties and density effects. A 2-D melting case by convection/diffusion flow follows in section 4.3.

4.1 Validation of Thermo-Fluid Computations: Natural Convection

In order to validate the present numerical approaches to the thermal effects, laminar natural convection flow driven by buoyancy force in a cavity is studied and compared with a benchmark solution. Figure 4.1 shows the numerical configuration, where the enclosed cavity is heated differentially at T_h and T_c on the vertical walls, and the horizontal walls are thermally insulated. The Prandtl number ($\mathrm{Pr} = \nu/\alpha$) is fixed to be 0.71, where ν is kinematic viscosity and α is thermal diffusivity. The simulation is conducted for the Rayleigh numbers of 10^3, 10^4, 10^5 and 10^6, and it is compared with the benchmark solution by de Vahl Davis (Davis 1983; Davis and Jones 1983). The Rayleigh number is defined as $\mathrm{Ra} = g\beta\Delta T L^3/(\alpha\nu)$, where g is gravitational acceleration, β is

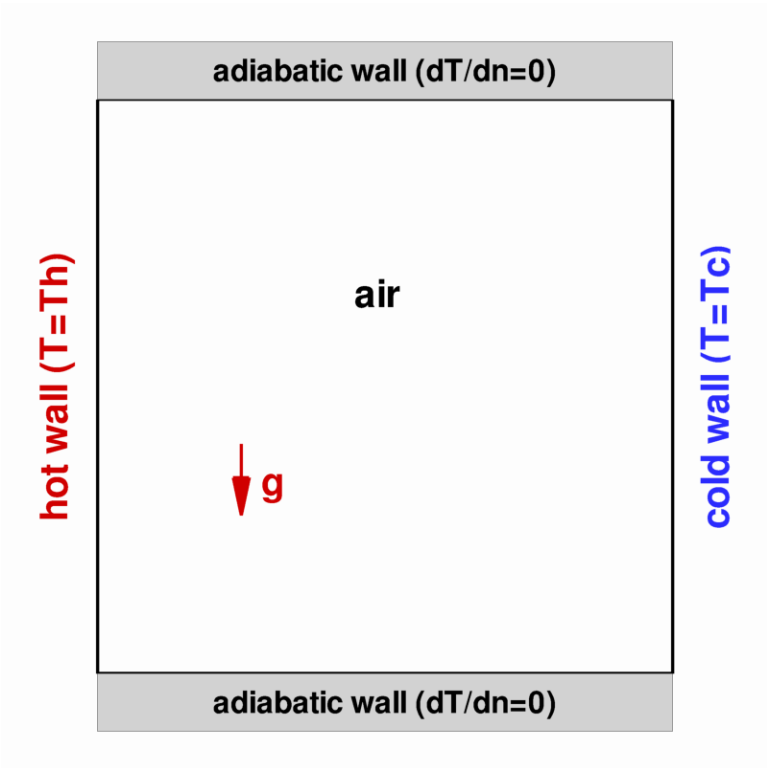

Figure 4.1: The numerical configuration of natural convection flow driven by buoyancy forces.

thermal expansion, ΔT is the difference of temperature between the hot and cold walls, and L is the width of the cavity.

An example of the buoyancy-driven natural convection flow at $Ra=10^5$ is shown in Figure 4.2. The flow moves up along the hot wall on the left side, and it moves down along the cold wall on the right side due to buoyancy force. These buoyancy effects make two counter-rotating eddies on the center of the cavity. To validate the implemented sharp solid interface treatment for the thermo-fluid transport computation, various cases with different tilted angles are simulated. Figure 4.3 shows the temperature contours and grid adaptation in 0^o- and 45^o-tilted cavities in the stationary Cartesian grids. In Figure

4.4, the velocity profiles along the mid-vertical and horizontal planes show identical results for different tilted angles and different grid adaptations. Because the present study used second-order central difference schemes, it shows second-order accuracy. This results in less than 0.1% errors at 81x81 grids when compared with the benchmark solution in Figure 4.5. Table 4.1 summarizes the errors for various variables at Rayleigh numbers of 10^3 to 10^6. For Rayleigh numbers less than 10^5, the error is less than 1% at 81x81 grids, and it is in agreement with the benchmark solution. However, the errors tend to increase as the Rayleigh number increases. The Nusselt number usually shows larger errors due to the effect of post-processing methods.

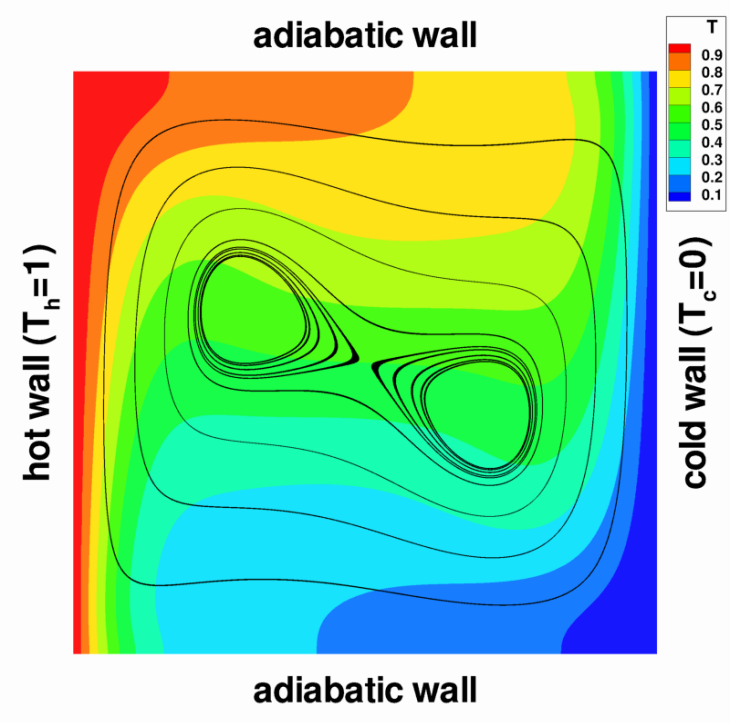

Figure 4.2: Temperature contour and streamlines in a natural convection flow driven by buoyancy forces at Ra=10^5.

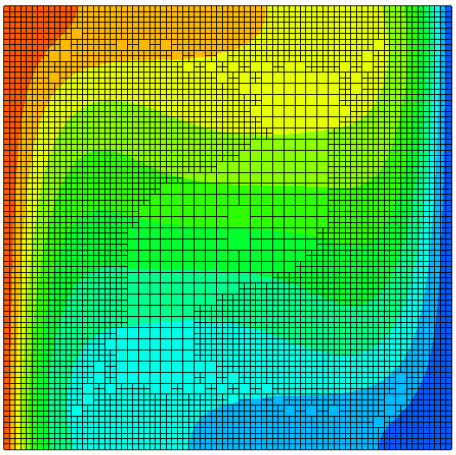

(a)

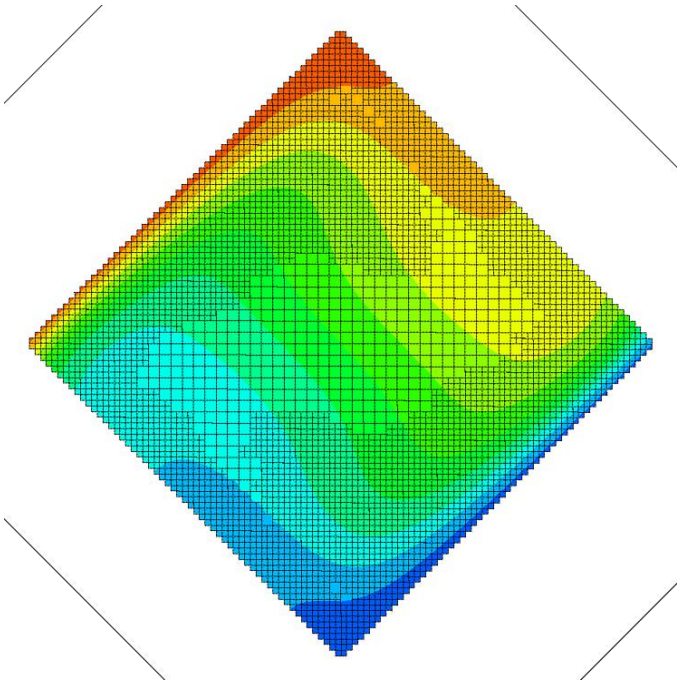

(b)

Figure 4.3: Examples of temperature contours and grid adaptation of a natural convection flow driven by buoyancy forces at $Ra=10^5$. The cavity is tilted with different angles on a Cartesian grid. (a) Non-tiled case. (b) 45^o-tilted case.

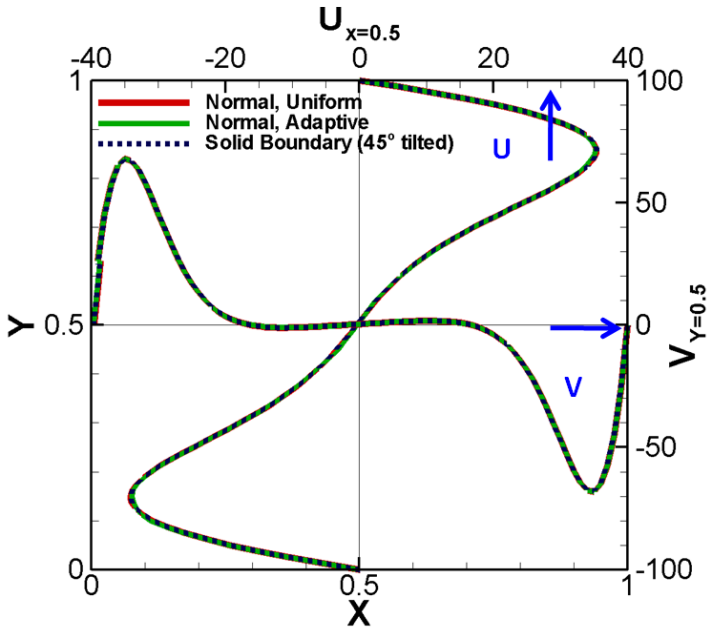

Figure 4.4: The comparison of velocity profiles at Ra=10^5 along the mid-plane. Different tilted angles and grid adaptation show good agreement.

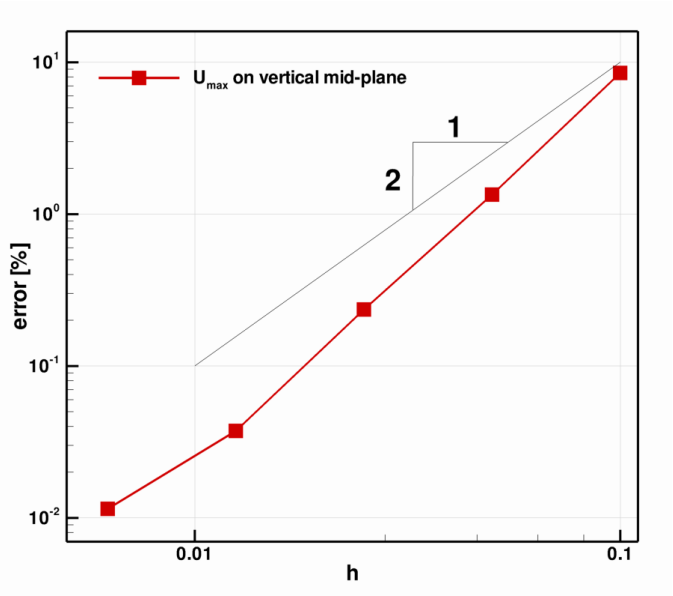

Figure 4.5: Grid convergence test for U_{max} on the vertical mid-plane based on the benchmark solution by de Vahl Davis (Davis 1983).

Table 4.1: The comparison between the present study and the benchmark solution by de Vahl Davis (Davis 1983) in a natural convection flow driven by buoyancy forces.

Φ	Error = (Φ - Φ_{ref})/Φ_{ref} [%] on 81x81 grids			
Ra	10^3	10^4	10^5	10^6
U_{max}	0.06	0.09	0.04	0.79
V_{max}	0.08	0.14	0.46	0.81
Nu	0.00	0.09	0.27	1.40
$Nu_{1/2}$	0.00	0.00	0.35	1.08
Nu_0	0.09	0.45	0.71	1.62
Nu_{max}	0.20	0.43	1.34	1.19
Nu_{min}	0.15	0.34	0.69	2.63

In Figure 4.6, the flow features of natural convection in a 2-D square cavity are investigated. The boundary layer grows along the wall, and the flow fields become more asymmetric as the Rayleigh number increases. For Ra=10^3 and 10^4, one large recirculation zone is created at the center of the enclosed cavity as the flow moves up the left side of the hot wall and down the right side of the cold wall. The one recirculation zone is divided into two counter-rotating smaller eddies at Ra=10^5. These counter-rotating eddies move to the corners of the top-left and bottom-right, and another eddie is created between them as the Rayleigh number reaches 10^6.

The detailed profiles of velocities, temperature, and the Nusselt number distribution are plotted in Figure 4.7. The temperature distribution shows rapid changes on the hot and cold vertical walls as the Rayleigh number increases, which, in turn, results in the corresponding velocity profiles. The Nusselt number distribution along the vertical walls shows this more clearly. The Nusselt number, and thus heat transfer, increase, as the Rayleigh number increases, and it displays an asymmetric heat transfer.

Most of the heat is transferred from the bottom of the hot wall on the left side and from the top of the cold wall on right side.

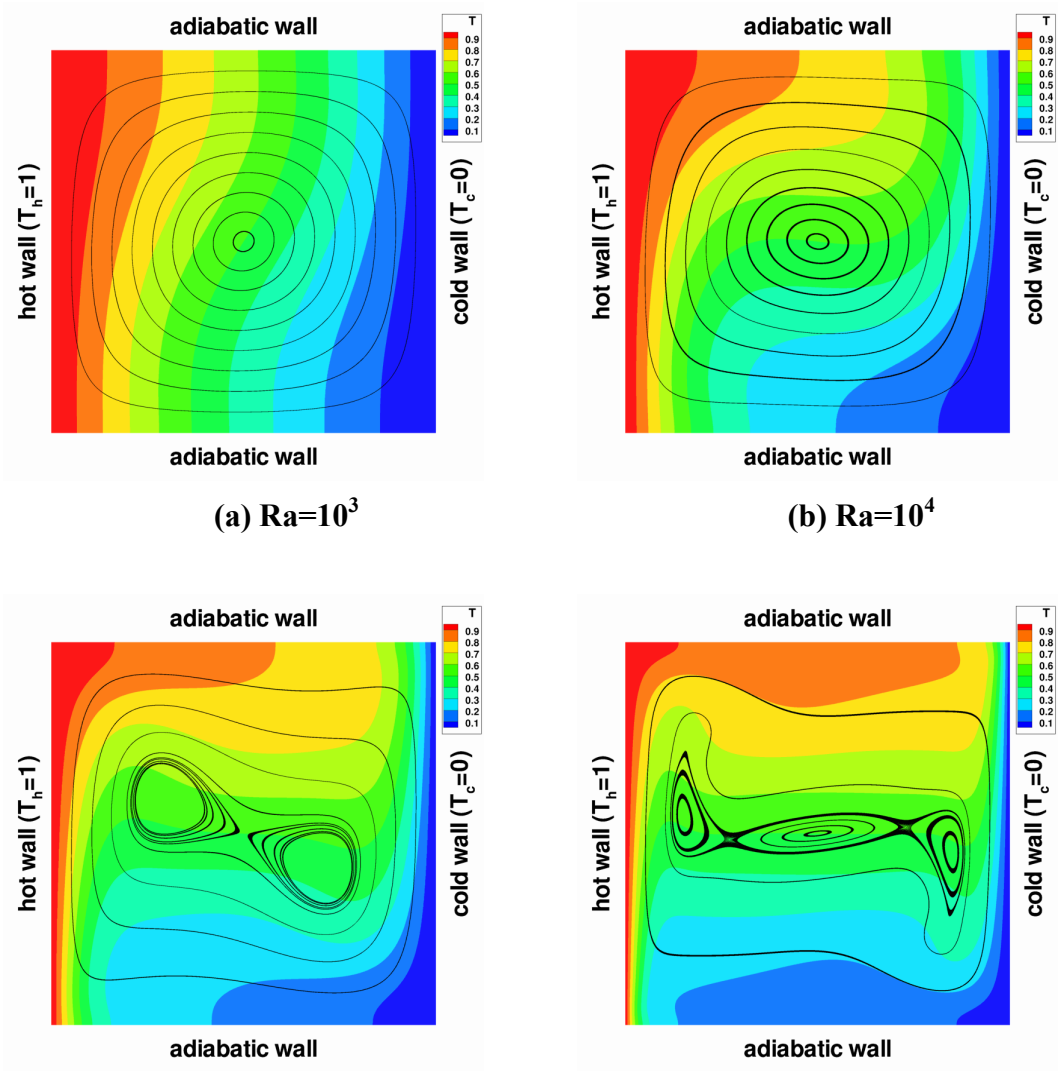

Figure 4.6: The effect of Rayleigh number in natural convection of a 2-D square cavity; temperature contour and streamlines (a) Ra=10^3 (b) Ra=10^4 (c) Ra=10^5 (d) Ra=10^6

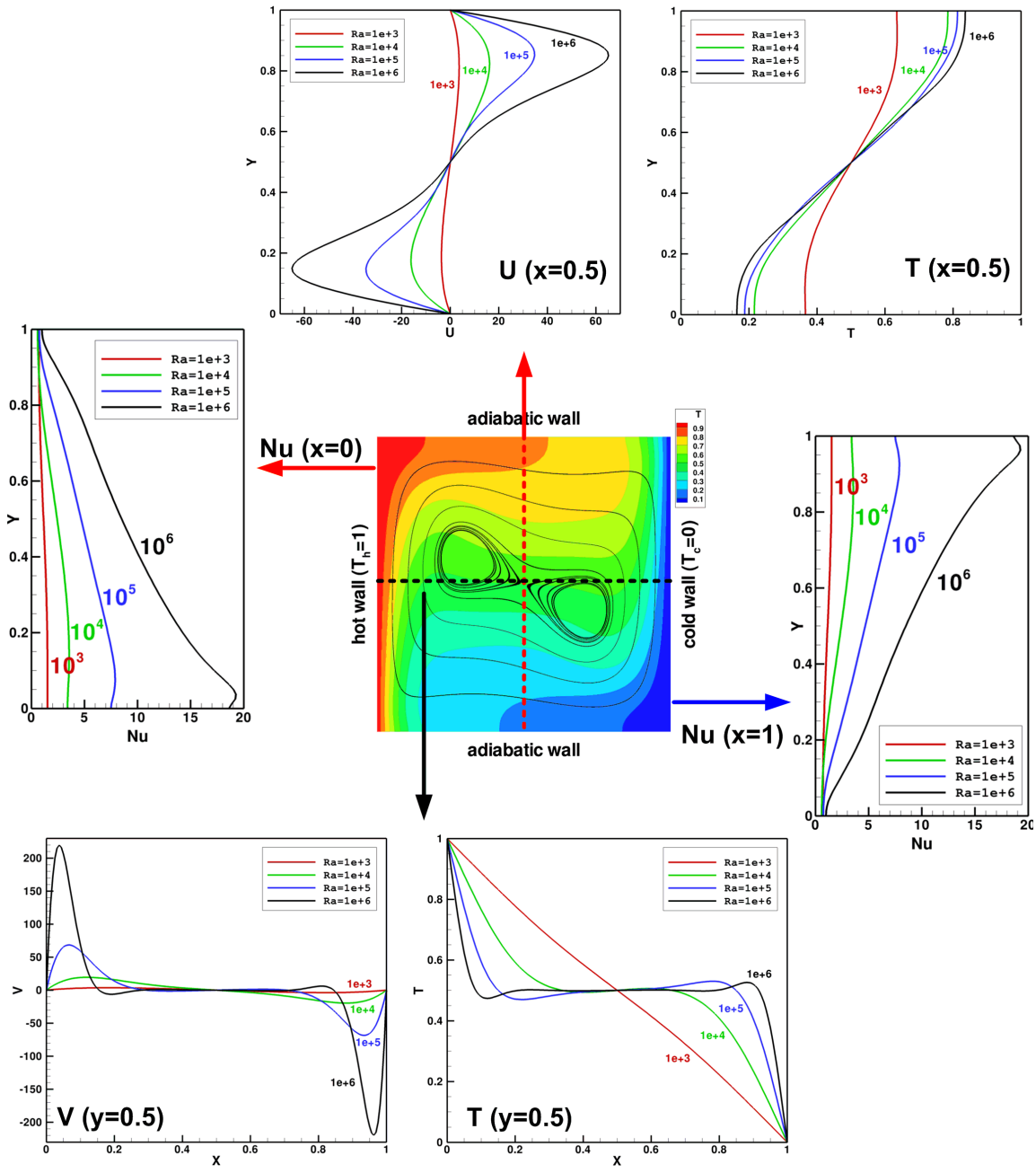

Figure 4.7: The effect of Rayleigh number in natural convection of a 2-D square cavity from Ra=10^3 to 10^6; velocity, temperature and Nusselt number.

4.2 Validation of phase change model: 1-D Stefan problem

A one-dimensional phase change test problem is performed to evaluate the present computational approach for phase change. One-phase and two-phase Stefan problems with no density effect are first validated and compared with the theoretical solution (Alexiades and Solomon 1993). The phase change with density effect is further simulated for open and closed containers, and self-pressurization in a closed container is measured in a closed container case.

4.2.1 1-D one- and two-phase Stefan Problem

Figure 4.8 shows the numerical configuration for these Stefan problems with the same density on a semi-infinite slab, where the left wall was maintained at a constant temperature T_0 with the interface location, $X(t)$, denoted by separating the vapor and liquid phases on the left and right sides respectively. The one-phase Stefan problem in Figure 4.8(a) is the simplest explicitly solvable phase change problem, where the phase 2 is assumed to stay at the saturation temperature and the temperature at the interface location; thus, the solution is independent of the phase 2. However, this assumption is an unrealistic scenario in the real world. In the two-phase Stefan problem of Figure 4.8 (b), the initial temperature of phase 2 is a certain value, T_∞, but it varies in time due to the heat transfer from phase 1. These one- and two-phase Stefan problems are summarized in Table 4.2.

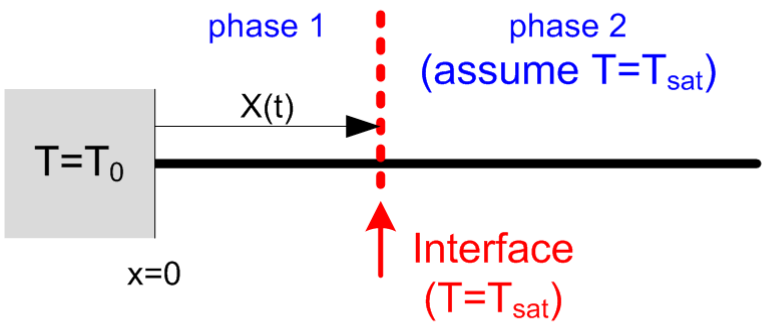

(a)

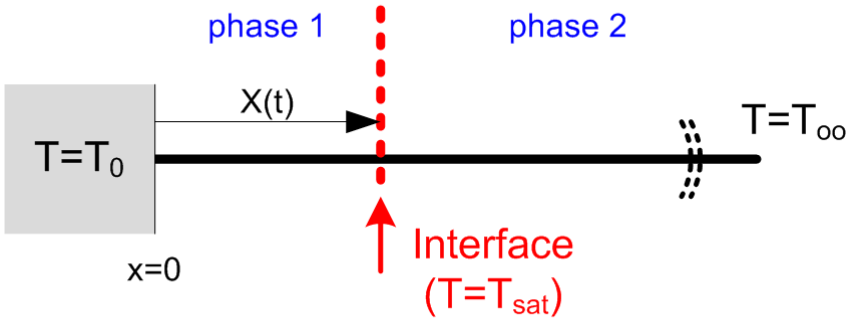

(b)

Figure 4.8: The numerical configuration of one dimensional phase change test problem. (a) One-phase Stefan problem. (b) Two-phase Stefan problem.

Table 4.2: The summary of one-dimensional Stefan problem.

	One-phase Stefan problem	Two-phase Stefan problem
Interface temperature	$T(X(t),t) = T_{sat}, \quad (t > 0)$	$T(X(t),t) = T_{sat}, \quad (t > 0)$
Stefan condition	$\rho L X'(t) = -k_1 T_x(X(t),t), (t > 0)$	$\rho L X'(t) = -k_1 T_x(X(t)^-,t) + k_2 T_x(X(t)^+,t)$
Initial condition	$T(x,0) = T_{sat}, \quad (x > 0)$	$T(x,0) = T_\infty < T_{sat}, \quad (x > 0)$
	$X(0) = 0$	$X(0) = 0$
Boundary condition	$T(0,t) = T_0 > T_{sat}, \quad (t > 0)$	$T(0,t) = T_0 > T_{sat}, \quad (t > 0)$
	$T(x,t) = T_{sat}, \quad (x \geq X(t), t > 0)$	$\lim_{x\to\infty} T(x,t) = T_\infty, \quad (t > 0)$

The theoretical interface location and temperature distribution for the one-phase Stefan problem are given by Eqs. (4.1)-(4.3), where α and C are thermal diffusivity and heat capacity of the phase 1 and L is the latent heat of the phase change, such as evaporation or melting. Parameter λ is obtained by solving the transcendental Eq. (4.3).

$$X(t) = 2\lambda\sqrt{\alpha t} \tag{4.1}$$

$$T(x,t) = T_0 - \left(\frac{T_0 - T_{sat}}{erf(\lambda)}\right) erf\left(\frac{x}{2\sqrt{\alpha t}}\right), \quad (for\ phase\ 1) \tag{4.2}$$

$$\lambda\, exp(\lambda^2)\, erf(\lambda) = C\left(\frac{T_0 - T_{sat}}{L\sqrt{\pi}}\right) \tag{4.3}$$

The computations are started with the initial interface location at $X(t) = 0.1$, assuming $T_0 = 1$ at the left end and the saturation temperature $T_{sat} = 0$. The parameter λ = 0.62006263 is based on the solution of the transcendental equation for the chosen fluid properties. The theoretical temperature distribution at the time that corresponds to the initial interface location is imposed as the initial condition of the present numerical study, with the computational domain from x=0 to x=1 using 100 grid cells. The interface location in time due to phase change is shown in Figure 4.9(a), where the interface moves fast in the beginning and slows down as time goes on because the temperature gradient becomes smaller as the interface goes far from the hot temperature at x=0. The present study agrees with the analytical solution in the interface location and temperature distribution at t=0.2.

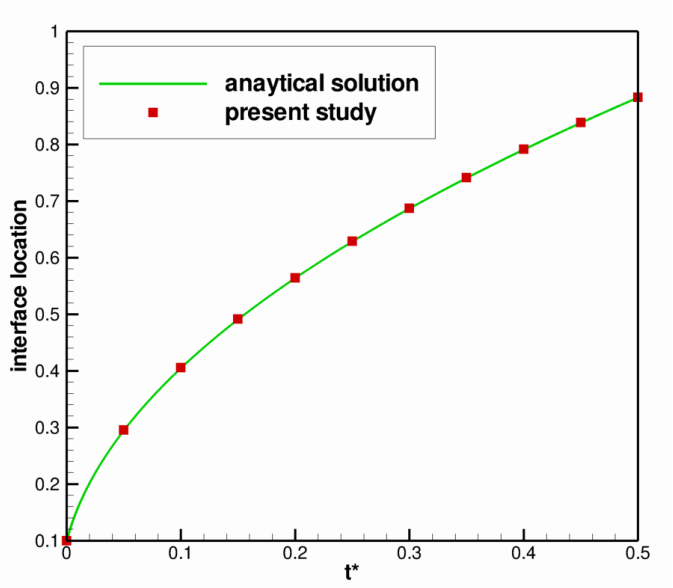

(a)

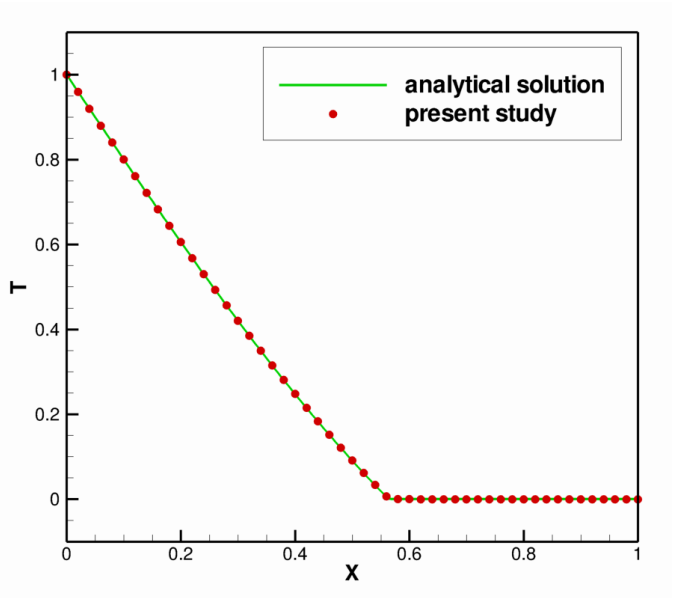

(b)

Figure 4.9: The comparison of the present numerical study and analytical solution for one-phase Stefan problem. (a) Interface location (b) Temperature profile at time = 0.2.

In the two-phase Stefan problem, the temperature of phase 2 is different from the saturation temperature, and it varies in time due to heat transfer from phase 1. Therefore, the solution is dependent on both phase 1 and 2 in Eqs. (4.4)-(4.7).

$$X(t) = 2\lambda\sqrt{\alpha t} \tag{4.4}$$

$$T(x,t) = T_0 - \left(\frac{T_0 - T_{sat}}{erf(\lambda)}\right) erf\left(\frac{x}{2\sqrt{\alpha_1 t}}\right), \quad (for\ phase\ 1) \tag{4.5}$$

$$T(x,t) = T_\infty + \left(\frac{T_{sat} - T_\infty}{erfc(\lambda\sqrt{\alpha_1/\alpha_2})}\right) erfc\left(\frac{x}{2\sqrt{\alpha_2 t}}\right), \quad (for\ phase\ 2) \tag{4.6}$$

$$\lambda = \frac{C_1(T_0 - T_{sat})}{L\sqrt{\pi}\, exp(\lambda^2)\, erf(\lambda)} - \frac{C_2(T_{sat} - T_\infty)}{L\sqrt{\pi}\, exp\left((\lambda\sqrt{\alpha_1/\alpha_2})^2\right) erfc(\lambda\sqrt{\alpha_1/\alpha_2})} \tag{4.7}$$

The two-phase Stefan problem is simulated using a varying thermal conductivity ratio from 0.1 to 10. It is known that the continuous interface treatment has some errors in simulating the thermal effect. However, Ferziger demonstrated that the error is due to an incorrect smoothed averaging of the material properties in the stationary heat conduction problem with no phase change (Ferziger 2003). In the present study, the thermal conductivity is averaged using in Eqs. (2.9)-(2.12), and it demonstrates substantial agreement with analytical solution, even for phase change cases. Figure 4.10 shows the interface location and the temperature distribution for the different thermal conductivity ratios from 0.1 to 10, and it matches very well with the analytical solution. The different temperature profile for each case is shown in Figure 4.10(b), where small thermal conductivity in phase 2 produces a large temperature gradient, and it results in fast movement of the interface due to a large mass transfer.

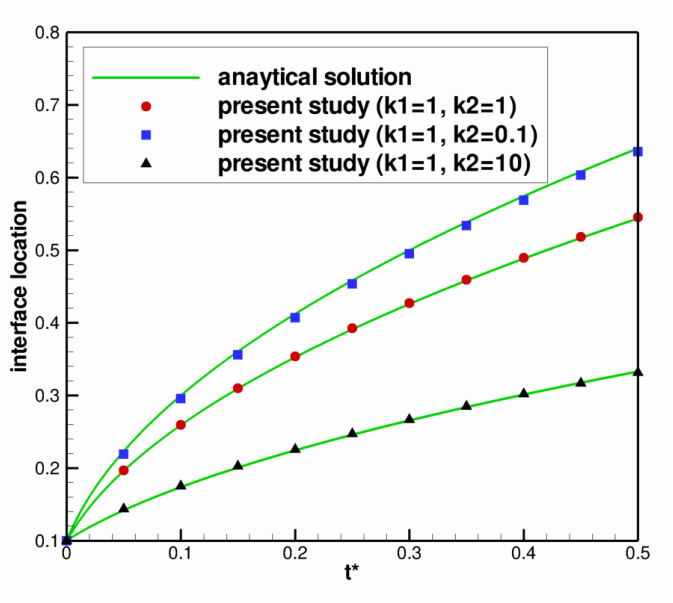

(a)

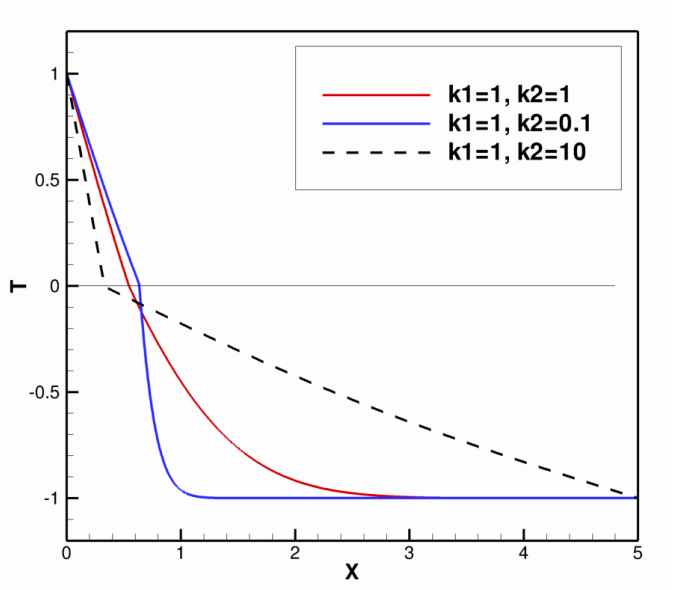

(b)

Figure 4.10: The comparison of the present numerical study and analytical solution for two-phase Stefan problem. (a) Interface location. (b) Temperature profile at time = 0.2.

4.2.2 1-D two-phase Stefan Problem: Density Effect

The density effect in a phase change is studied in the open and closed container system. The liquid density is assumed to be twice that of the gas density, and the given material properties and boundary conditions are shown in Table 4.3. When the liquid phase is transferred into the gas phase, the mass of the liquid phase is conserved during the phase change according to the rule of mass conservation. However, the volume of the transferred phase is not conserved. Because the density ratio of liquid to gas is twice from the beginning, the volume of the transferred gas is initially twice that of the volume of the corresponding liquid. The difference of volume may result in a rise of density and pressure in the gas phase and/or a volume expansion of the gas phase. In Figure 4.11(a), a container open at the right end is considered, where the gas phase will expand and the liquid phase will move to the right during the phase change process. If we assume there is no mechanical drag, the bulk of the liquid will move with no mechanical force, and the density of the gas will be maintained, as will the original density because the right end is open.

Figure 4.12(a) shows the interface location change in the phase change process, and the open container simulation is identical with the analytical solution. The closed container case is shown in Figure 4.11(b), where both ends are closed, and the liquid cannot move to the right; therefore, the gas cannot be expanded. This causes the pressure to rise in the gas phase as the self-pressurization occurs in a closed spacecraft fuel tank system. Figure 4.12(a) shows that the interface moves slowly in a closed system because the liquid phase cannot move, and the interface movement is completely dominated by the amount of phase change. Figure 4.12(b) compares the pressure between the two

Table 4.3: Parameters for 1-D two-phase Stefan problem with density effect.

Parameter	Phase 1 (gas)	Phase 2 (liquid)
Temperature at end	$T_0 = 1.0$	$T_\infty = -1.0$
Saturation temperature	$T_{sat} = 0.0$	
density (ρ)	1.0	2.0
heat capacity (C)	1.0	1.0
thermal conductivity (K)	1.0	1.0

systems. In the open container, the liquid moves freely, so the pressure of the gas is maintained. This is the same as it is in the beginning because the expanded gas pushes the liquid up and into the right side. When the phase change occurs in the closed system, the pressure of the gas phase rises when density increases. However, the speed of the pressure rise decreases in time, and it reaches asymptotic values.

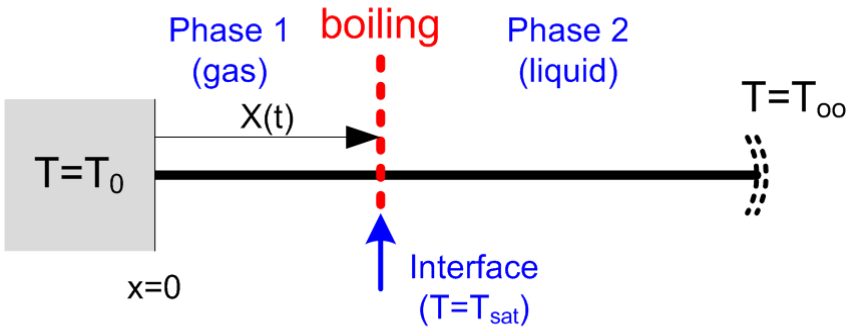

(a)

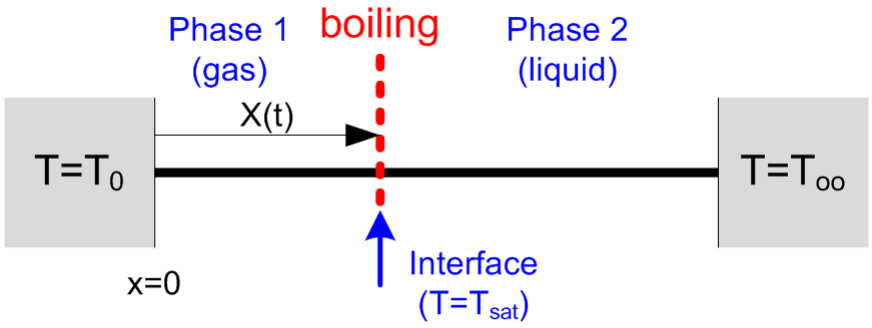

(b)

Figure 4.11: The numerical configuration of one-dimensional Stefan problems with density effect. (a) Open container system with gas expansion and no density change. (b) Closed container with pressure rise

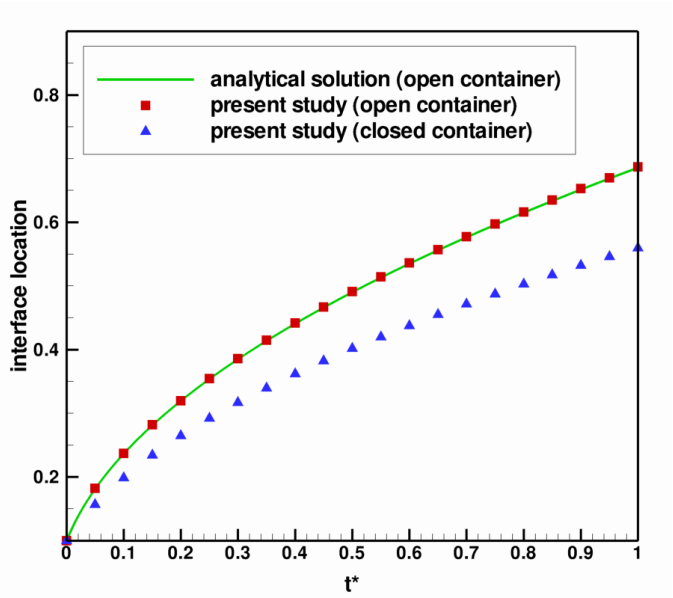

(a)

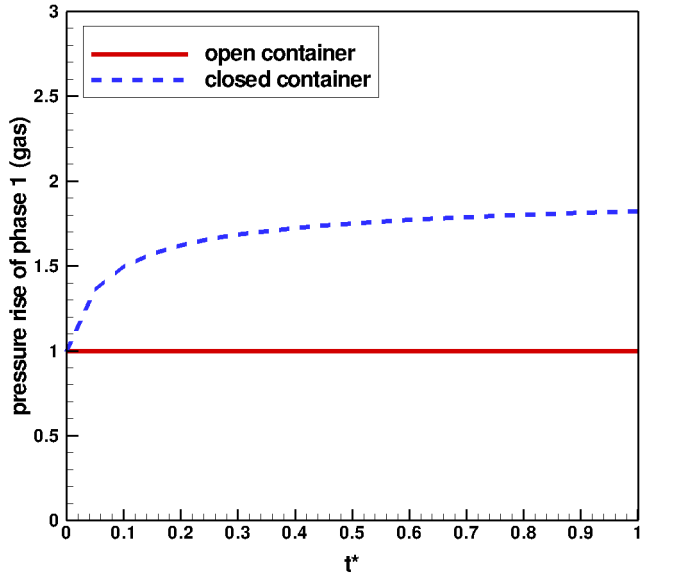

(b)

Figure 4.12: The comparison of the interface location and the pressure rise between open and closed container system. (a) Interface location. (b) Pressure rise of gas phase.

4.3 2-D Melting in a Square Cavity by Convection/Diffusion

Two-dimensional melting driven by natural convection in a square cavity is considered to present the fidelity of the phase-change approach implemented. The case is performed in a rectangular tank half-filled with a pure substance in solid phase suddenly exposed to high isothermal surface at left vertical wall and thermally insulated at top and bottom walls. The initial temperature of the material in this cavity is uniformly T_M as the temperature of right vertical wall, and gravity is parallel to the vertical wall. Constant thermodynamic properties are assumed through the melting process. Figure 4.13 shows the configuration of 2-D melting in a square cavity by convection/diffusion flow. The liquid/solid interface is initially located at the mid-vertical plane, and moves to right by melting process since the heat is transferred by convection and diffusion flows from hot wall at left side to solid surface. The isothermal temperature is assumed in the solid phase.

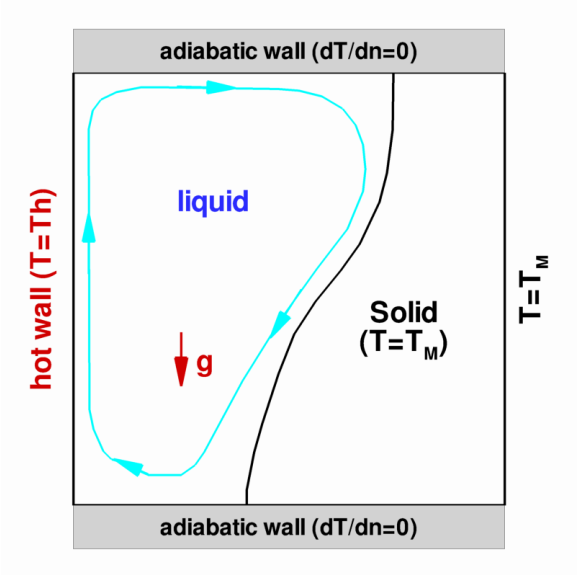

Figure 4.13: The configuration of a 2-D melting by convection/diffusion.

In the case of melting driven by natural convection in a square cavity, dimensional analysis shows the heat transfer rate can be expressed in terms power laws of Rayleigh number ($\mathrm{Ra} = g\beta\Delta T L^3/\alpha\nu$) at high Prandtl number ($\mathrm{Pr} = \nu/\alpha$) range while it is function of Ra times Pr at low Prandtl number range (Bertrand *et al.* 1999; Jany and Bejan 1988). Here, g is gravitational acceleration, β is thermal expansion, ΔT is the difference of temperature between hot wall and interface, and L is the height of cavity. ν and α are the kinematic viscosity and the thermal diffusivity, respectively. In this study, the Prandtl number is fixed at $Pr = 0.71$ and two different Rayleigh number cases ($\mathrm{Ra} = 10$ and 10^5) are computed for simulating diffusion-dominated and convection-dominated phase change flow. Figure 4.14 shows the location of interface between liquid and solid phase with temperature contours and velocity vectors plot. In a small Rayleigh number with $Ra = 10$ of Figure 4.14(a), thermal diffusion dominates the natural convection flow, and is the primary source of heat transfer. Thus, the interface moves to the right with the same melting speed, since the heat transfer is almost the same along the interface. However, at the high Rayleigh number case of Figure 4.14(b), the convection effect dominates the natural convection, and transfers heat from the left hot wall to the right solid side. The solid is melted from the top side due to large heat transfer by the convection flow. This is shown clearly from the temperature contour plot. Figure 4.15 shows the comparison of liquid phase fraction between low and high Rayleigh number cases, and we can find that the heat transfer at $\mathrm{Pr} = 0.71$ increases with the Rayleigh number as already known.

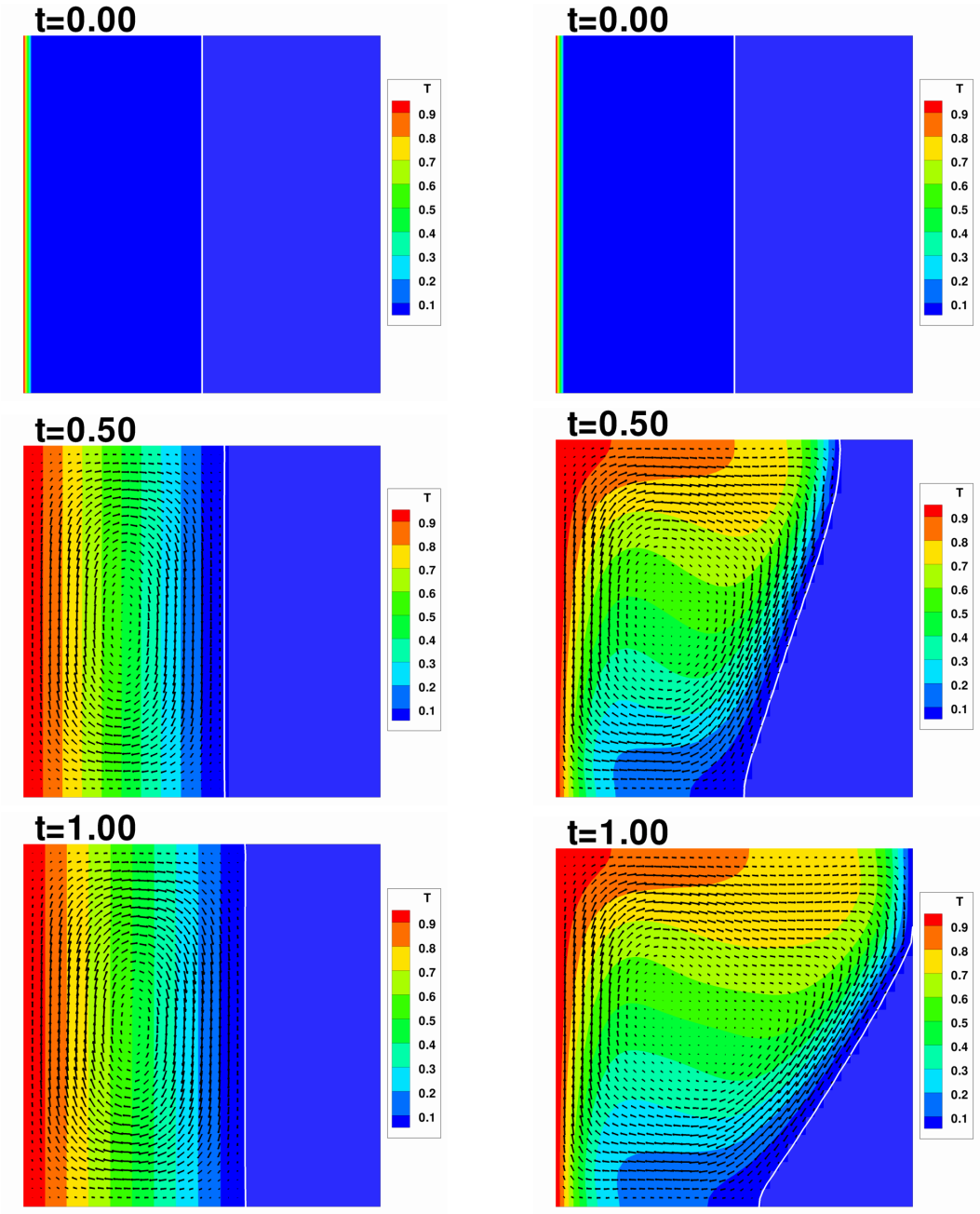

Figure 4.14: The snapshots of the temperature contours and velocity fields during melting process in a square cavity by natural convection flow. (a) Diffusion-dominated melting case at Ra=10. (b) Convection-dominated melting case at Ra=10^5.

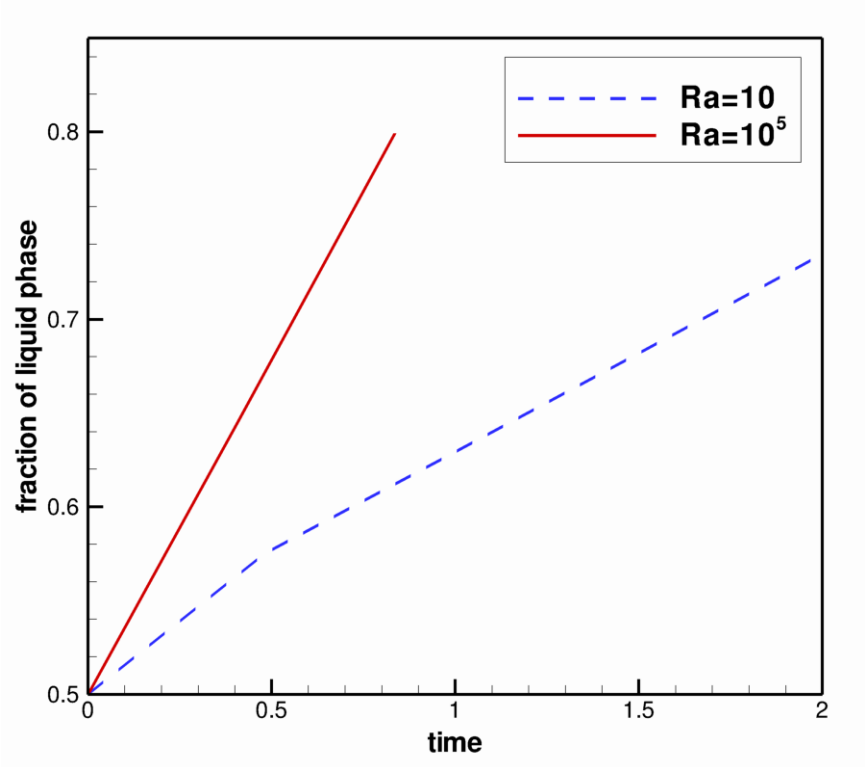

Figure 4.15: The comparison of the liquid phase fraction in a melting process by convection/diffusion flow.

4.4 Summary

In this chapter, thermo-fluid transport computations including phase change between different phases (fluid/fluid or fluid/solid) are conducted. The implemented incompressible flow solver with Boussinesq approximation is validated using natural convection flow in an enclosed cavity driven by buoyancy force, and the developed sharp solid interface treatment and adaptive grids method works well in these thermo-fluid problems with 2^{nd} order accuracy. The phase change model is validated using 1-D one- and two-phase Stefan problems, and the results match very well with the analytical solution. The density effects during phase change are tested for two-phase Stefan problem with different density ratios in a closed and open container. 2-D melting simulation by convection/diffusion flow is investigated to understand phase change across a solid surface. The implemented phase change model works well with both continuous fluid and sharp solid interface models.

CHAPTER 5

CONCLUSIONS AND FUTURE WORK

This chapter summarizes the accomplishments and key contributions of this dissertation, and proposes improvements and future work for the present research.

5.1 Conclusions

In this dissertation, the marker-based 3-D adaptive Eulerian-Lagrangian method is investigated and further developed for an integrated 3-D computational capability for multiphase flows, including spacecraft applications. The bulk flow variables are solved on the stationary (Eulerian) background grid, whereas the interface variables are handled by moving (Lagrangian) surface meshes. A single fluid formulation for all fluid phases is implemented via smoothed material properties with the help of the indicator function. The interface is represented by massless markers and triangular surface meshes with connectivity information. The fluid interface is treated continuously for large-deformable phase boundary simulation. In addition, the solid interface is treated sharply via ghost cell method for better accuracy. The contact line force model is proposed in order to enforce the moving contact angle. The phase change model is implemented using a probe-based temperature gradient technique. The geometry- and solution-based Cartesian grid adaptation is utilized for effective computation.

For isothermal computations and thermo-fluid transport computations with phase change, validation studies and spacecraft fuel delivery applications, including liquid fuel draining, sloshing, and surface stability, are conducted and assessed with analytical solution and experimental measurements.

In summary, the following key contributions are achieved in this dissertation.

(i) The marker-based adaptive Eulerian-Lagrangian method is developed for complex multiphase flow computations having both fluid and solid interfaces:

- Both sharp and continuous interface methods are implemented with contact line force model in a unified framework in order to simulate practical engineering problems having fluid interface around irregular solid geometries. The contact line force model is validated with capillary tube simulation with various contact angles and Laplace numbers, and it shows good consistency with theoretical values especially from 15^o to 165^o of contact angles.
- The phase change model using a probe-based temperature gradient computation is implemented with both sharp solid interfaces and continuous fluid interfaces. 1-D one- and two-phase Stefan problems with density effects are solved for validation study, and the results match very well with the analytical solution. 2-D melting by convection/diffusion flows is simulated to test phase changes across the fluid/solid interface. The implemented phase change model works well with both continuous fluid and sharp solid interface models.

(ii) Numerical studies on the spacecraft fuel delivery system are conducted and accessed with experimental measurements and scaling analysis:

- In a liquid fuel draining process under microgravity, a capillary-dominated regime, transition regime, and inertia-dominated regimes are observed depending on the relative influence between capillary force and inertia force. The liquid residual increases with oscillation as the draining parameter, defined by Symons (Symons 1978), increases, and it remains almost constant in the inertia-dominated regime with a large draining parameter.
- Engine shutdown in earth's orbit results in large sloshing motions due to the sudden reduction in acceleration, and it has significant influence on the vehicle dynamics with large shift in its center of mass.
- Liquid fuel surface stability under thrust oscillation is studied. The surface wave exhibits aperiodic unstable states when the forcing oscillation magnitude exceeds a certain threshold value, which is referred threshold acceleration. The threshold acceleration increases with forcing frequency and viscosity, and it is correlated with forcing frequency, surface tension, and viscosity by scaling analysis.

5.2 Future Work

Future work is proposed in the following areas:

- In this study, the implemented contact line force model presents reliable results for various stationary and moderately moving boundary problems such as capillary tube and liquid fuel dynamics. However, it is required to investigate the applicable limitations to this contact line force model, especially with validation study for dynamic contact angle.
- The present approach implemented laminar flow computation. However, many engineering problems require turbulent flow computation with high Reynolds

number or high Rayleigh number. For single phase flow computations, the sharp interface method has been extended to turbulent flows by several researchers (Iaccarino and Verzicco 2003; Yang and Balaras 2006). A turbulent model can be added to the present multiphase flow solver, and wall boundary treatment should be considered along with the present sharp solid interface method with local slip contact line model.

- Even with the present adaptive grid technique, multiphase flow applications require large amount of computer memory and long computational time due to fine grid for multiple length scale. Parallel computing techniques can be implemented for effective computation. However, it is difficult to distribute overall computational load evenly on a number of processors especially on the present adaptive grid since the grid is changing dynamically and locally with moving interfaces. Effective partitioning algorithm such as the space filling curve (SFC) (Aftosmis *et al.* 2004) should be implemented with the dynamic load balancing for the present adaptive grid method.
- Further studies related to thermal effects in a spacecraft should be conducted for overall understanding of fuel tank dynamics. The phase change due to heat absorption results in a self-pressurization and a fuel loss in a spacecraft fuel tank. These effects should be investigated for designing spacecraft fuel tank and planning missions.

REFERENCES

Aftosmis, M. J. Solution adaptive cartesian grid methods for aerodynamic flows with complex geometries. *Lecture notes, von Karman Institute for Fluid Dynamics, Series 2*. 1997.

Aftosmis, M. J., Berger, M. J., andMurman, S. M. Applications of space-filling-curves to cartesian methods for cfd. *Lecture notes, von Karman Institute for Fluid Dynamics, Series* 2004; **1232**: 2003-1237.

Al-Rawahi, N. and Tryggvason, G. Numerical simulation of dendritic solidification with convection: Two-dimensional geometry. *Journal of Computational Physics* 2002; **180**(2): 471-496.

Al-Rawahi, N. and Tryggvason, G. Numerical simulation of dendritic solidification with convection: Three-dimensional flow. *Journal of Computational Physics* 2004; **194**(2): 677-696.

Alexiades, V. and Solomon, A. D. *Mathematical modeling of melting and freezing processes*. Taylor & Francis, 1993.

Antaki, J. F., Blelloch, G. E., Ghattas, O., Malcevic, I., Miller, G. L., andWalkington, N. J. A parallel dynamic-mesh lagrangian method for simulation of flows with dynamic interfaces. *Proceedings of the 2000 ACM/IEEE Conference on Supercomputing* 2000.

Aulisa, E., Manservisi, S., andScardovelli, R. A mixed markers and volume-of-fluid method for the reconstruction and advection of interfaces in two-phase and free-boundary flows. *Journal of Computational Physics* 2003; **188**(2): 611-639.

Aulisa, E., Manservisi, S., andScardovelli, R. A surface marker algorithm coupled to an area-preserving marker redistribution method for three-dimensional interface tracking. *Journal of Computational Physics* 2004; **197**(2): 555-584.

Balsara, D. Divergence-free adaptive mesh refinement for magnetohydrodynamics. *Journal of Computational Physics* 2001; **174**(2): 614-648.

Berenyi, S. G. and Abdalla, K. L. Vapor ingestion phenomenon in hemispherically bottomed tanks in normal gravity and in weightlessness. NASA TN D-5704, 1970.

Bertrand, O., Binet, B., Combeau, H., Couturier, S., Delannoy, Y., Gobin, D., Lacroix, M., Quere, P. L., Medale, M., Mencinger, J., Sadat, H., andVieira, G. Melting driven by natural convection a comparison exercise: First results. *International Journal of Thermal Sciences* 1999; **38**: 5-26(22).

Das, S. P. and Hopfinger, E. J. Parametrically forced gravity waves in a circular cylinder and finite-time singularity. *Journal of Fluid Mechanics* 2008; **599**: 205-228.

Davis, G. D. V. Natural convection of air in a square cavity: A bench mark numerical solution. *International Journal for Numerical Methods in Fluids* 1983; **3**(3): 249-264.

Davis, G. D. V. and Jones, I. P. Natural convection in a square cavity: A comparison exercise. *International Journal for Numerical Methods in Fluids* 1983; **3**(3): 227-248.

de Sousa, F. S., Mangiavacchi, N., Nonato, L. G., Castelo, A., Tomé, M. F., Ferreira, V. G., Cuminato, J. A., andMcKee, S. A front-tracking/front-capturing method for the simulation of 3d multi-fluid flows with free surfaces. *Journal of Computational Physics* 2004; **198**(2): 469-499.

Derdul, J. D., Grubb, L. S., andPetrash, D. A. Experimental investigation of liquid outflow from cylindrical tanks during weightlessness. NASA TN D-3746, 1966.

Engquist, B., Tornberg, A. K., andTsai, R. Discretization of dirac delta functions in level set methods. *Journal of Computational Physics* 2005; **207**(1): 28-51.

Enright, D., Fedkiw, R., Ferziger, J., andMitchell, I. A hybrid particle level set method for improved interface capturing. *Journal of Computational Physics* 2002; **183**(1): 83-116.

Enright, D., Losasso, F., andFedkiw, R. A fast and accurate semi-lagrangian particle level set method. *Computers and Structures* 2005; **83**(6-7): 479-490.

Faraday, M. On a peculiar class of acoustical figures; and on certain forms assumed by groups of particles upon vibrating elastic surfaces. *Philosophical Transactions of the Royal Society of London* 1831; **121**: 299-340.

Ferziger, J. H. Interfacial transfer in tryggvason's method. *International Journal for Numerical Methods in Fluids* 2003; **41**(5): 551-560.

Francois, M. and Shyy, W. Micro-scale drop dynamics for heat transfer enhancement. *Progress in Aerospace Sciences* 2002; **38**(4): 275-304.

Francois, M. and Shyy, W. Computations of drop dynamics with the immersed boundary method, part 1: Numerical algoritm and buoyancy-induced effect. *Numerical Heat Transfer: Part B: Fundamentals* 2003; **44**(2): 101-118.

Glimm, J., Graham, M. J., Grove, J., Li, X. L., Smith, T. M., Tan, D., Tangerman, F., andZhang, Q. Front tracking in two and three dimensions. *Comput. Math. Appl* 1998; **35**(1).

Goodridge, C. L., Shi, W. T., andLathrop, D. P. Threshold dynamics of singular gravity-capillary waves. *Physical Review Letters* 1996; **77**(22): 4692.

Goodridge, C. L., Shi, W. T., Hentschel, H. G. E., andLathrop, D. P. Viscous effects in droplet-ejecting capillary waves. *Physical Review E* 1997; **56**(1): 472.

Goodridge, C. L., Hentschel, H. G. E., andLathrop, D. P. Breaking faraday waves: Critical slowing of droplet ejection rates. *Physical Review Letters* 1999; **82**(15): 3062.

Ham, F. E., Lien, F. S., andStrong, A. B. A cartesian grid method with transient anisotropic adaptation. *Journal of Computational Physics* 2002; **179**(2): 469--494.

Harlow, F. H. and Welch, J. E. Numerical calculation of time-dependent viscous incompressible flow. *Phys. Fluids* 1965; **8**(12): 2182-2189.

Iaccarino, G. and Verzicco, R. Immersed boundary technique for turbulent flow simulations. *Applied Mechanics Reviews* 2003; **56**(3): 331-347.

Ingram, D. M., Causon, D. M., andMingham, C. G. Developments in cartesian cut cell methods. *Mathematics and Computers in Simulation* 2003; **61**(3-6): 561-572.

Jany, P. and Bejan, A. Scaling theory of melting with natural convection in an enclosure. *International Journal of Heat and Mass Transfer* 1988; **31**(6): 1221-1235.

Johansen, H. and Colella, P. A cartesian grid embedded boundary method for poisson's equation on irregular domains. *Journal of Computational Physics* 1998; **147**(1): 60-85.

Juric, D. and Tryggvason, G. Computations of boiling flows. *Int. J. Multiphase Flow* 1998; **24**(3): 387-410.

Kang, M., Fedkiw, R. P., andLiu, X. D. A boundary condition capturing method for multiphase incompressible flow. *Journal of Scientific Computing* 2000; **15**(3): 323-360.

Landau, L. D. and Lifshitz, E. M. *Fluid mechanics*. Pergamon Press: New York, 1987.

Leveque, R. J. and Li, Z. The immersed interface method for elliptic equations with discontinuous coefficients and singular sources. *SIAM Journal on Numerical Analysis* 1994; **31**(4): 1019-1044.

Li, Z. and Lai, M. C. The immersed interface method for the navier-stokes equations with singular forces. *Journal of Computational Physics* 2001; **171**(2): 822-842.

Liu, H., Krishnan, S., Marella, S., andUdaykumar, H. S. Sharp interface cartesian grid method ii: A technique for simulating droplet interactions with surfaces of arbitrary shape. *Journal of Computational Physics* 2005; **210**(1): 32-54.

Luo, X.-Y., Ni, M.-J., Ying, A., andAbdou, M. A. Numerical modeling for multiphase incompressible flow with phase change. *Numerical Heat Transfer, Part B: Fundamentals* 2005; **48**(5): 425-444.

Miles, J. and Henderson, D. Parametrically forced surface waves. *Annual Review of Fluid Mechanics* 1990; **22**: 143-165.

Mittal, R. and Iaccarino, G. Immersed boundary methods. *Annual Review of Fluid Mechanics* 2005; **37**(1): 239-261.

Nussle, R. C., Derdul, J. D., andPetrash, D. A. Photographic study of propellant outflow from a cylindrical tank during weightlessness. NASA TN D-2572, 1965.

Osher, S. and Fedkiw, R. Level set methods- an overview and some recent results. *Journal of Computational Physics* 2001; **169**(2): 463-502.

Osher, S. and Fedkiw, R. *Level set methods and dynamic implicit surfaces*. Springer: New York, 2002.

Perlin, M. and Schultz, W. W. Capillary effects on surface waves. *Annual Review of Fluid Mechanics* 2000; **32**: 241-274.

Perot, B. and Nallapati, R. A moving unstructured staggered mesh method for the simulation of incompressible free-surface flows. *Journal of Computational Physics* 2003; **184**(1): 192-214.

Peskin, C. S. Numerical analysis of blood flow in the heart. *J. Comput. Phys* 1977; **25**(3): 220.

Peskin, C. S. and McQueen, D. M. A three-dimensional computational method for blood flow in the heart. I. Immersed elastic fibers in a viscous incompressible fluid. *J. Comput. Phys* 1989; **81**(2): 372-405.

Peskin, C. S. The immersed boundary method. *Acta Numerica* 2003; **11**: 479-517.

Petrash, D. A., Zappa, R. F., andOtto, E. W. Experimental study of the effects of weightlessness on the configuration of mercury and alcohol in spherical tanks. NASA TN D-1197, 1962.

Petrash, D. A., Nussle, R. C., andOtto, E. W. Effect of the acceleration disturbances encountered in the ma-7 spacecraft on the liquid-vapor interface in a baffled tank during weightlessness. NASA TN D-1577, 1963.

Prins, J. J. M. Sloshsat-flevo (facility for liquid experimentation and verification in orbit). IAF-00-J.2.05, 2000.

Prosperetti, A. and Tryggvason, G. *Computational methods for multiphase flow*. Cambridge University Press: New York, 2007.

Renardy, Y. and Renardy, M. Prost- a parabolic reconstruction of surface tension for the volume-of-fluid method. *Journal of Computational Physics* 2002; **183**(2): 400-421.

Ryskin, G. and Leal, L. G. Numerical solution of free-boundary problems in fluid mechanics. Part 1. The finite-difference technique'. *J Fluid Mechanics* 1984; **148**: 1-17.

Scardovelli, R. and Zaleski, S. Direct numerical simulation of free-surface and interfacial flow. *Annual Review of Fluid Mechanics* 1999; **31**(1): 567-603.

Sethian, J. A. and Smereka, P. Levet set methods for fluid interfaces. *Annual Review of Fluid Mechanics* 2003; **35**(1): 341-372.

Shin, S. and Juric, D. Modeling three-dimensional multiphase flow using a level contour reconstruction method for front tracking without connectivity. *Journal of Computational Physics* 2002; **180**(2): 427-470.

Shyy, W. *Computational modeling for fluid flow and interfacial transport*. Elsevier: New York, 1994.

Shyy, W., Udaykumar, H. S., Rao, M. M., andSmith, R. W. *Computational fluid dynamics with moving boundaries*. Taylor & Francis: Philadelphia, 1996.

Shyy, W. Multiphase computations using sharp and continuous interface techniques for micro-gravity applications. *Comptes rendus. Mecanique* 2004; **332**(5-6): 375--386.

Simonelli, F. and Gollub, J. P. Surface wave mode interactions: Effects of symmetry and degeneracy. *Journal of Fluid Mechanics* 1989; **199**: 471-494.

Singh, R. Three-dimensional marker-based multiphase flow computation using adaptive cartesian grid techniques*Mechanical and Aerospace Engineering*. University of Florida: Gainesville, 2006;144.

Singh, R. and Shyy, W. Three-dimensional adaptive cartesian grid method with conservative interface restructuring and reconstruction. *Journal of Computational Physics* 2007; **224**(1): 150-167.

Son, G. and Dhir, V. K. Numerical simulation of film boiling near critical pressures with a level set method. *Journal of Heat Transfer* 1998; **120**(1): 183-192.

Stockie, J. M. Analysis and computation of immersed boundaries, with application to pulp fibres*Institute of Applied Mathematics*. University of British Columbia, 1997.

Sussman, M. A second order coupled level set and volume-of-fluid method for computing growth and collapse of vapor bubbles. *Journal of Computational Physics* 2003; **187**(1): 110-136.

Symons, E. P. Draining characteristics of hemispherically bottomed cylinders in a low-gravity environment. NASA TP-1297, 1978.

Toole, L. E. and Hastings, L. J. An experimental study of the behavior of a sloshing liquid subjected to a sudden reduction in acceleration. NASA TM X-53755, 1968.

Torres, D. J. and Brackbill, J. U. The point-set method- front-tracking without connectivity. *Journal of Computational Physics* 2000; **165**(2): 620-644.

Tryggvason, G., Bunner, B., Esmaeeli, A., Al-Rawahi, N., Tauber, W., Han, J., Jan, Y. J., Juric, D., andNas, S. A front-tracking method for the computations of multiphase flow. *Journal of Computational Physics* 2001; **169**(2): 708-759.

Tryggvason, G., Esmaeeli, A., andAl-Rawahi, N. Direct numerical simulations of flows with phase change. *Computers and Structures* 2005; **83**(6-7): 445-453.

Udaykumar, H. S., Shyy, W., andRao, M. M. Elafint: A mixed eulerian-lagrangian method for fluid flows with complex and moving boundaries. *International Journal for Numerical Methods in Fluids* 1996; **22**(8): 691-712.

Uzgoren, E., Sim, J., andShyy, W. Marker-based, 3-d adaptive cartesian grid method for multiphase flow around irregular geometries. *Communications in Computational Physics* 2009; **5**(1): 1-41.

Veldman, A. E. P., Gerrits, J., Luppes, R., Helder, J. A., andVreeburg, J. P. B. The numerical simulation of liquid sloshing on board spacecraft. *Journal of Computational Physics* 2007; **224**(1): 82-99.

Ward, W. D., Toole, L. E., Ponder, C. A., Meadows, M. E., Simmons, C. W., Lytle, J. H., McDonald, J. M., andKavanaugh, B. M. Evaluation of as-203 low gravity orbital experiment. Technical Report HSM-R421-67, 1967.

Welch, S. W. J. and Wilson, J. A volume of fluid based method for fluid flows with phase change. *Journal of Computational Physics* 2000; **160**(2): 662-682.

Xu, S. and Wang, Z. J. An immersed interface method for simulating the interaction of a fluid with moving boundaries. *Journal of Computational Physics* 2006; **216**(2): 454-493.

Yang, J. and Balaras, E. An embedded-boundary formulation for large-eddy simulation of turbulent flows interacting with moving boundaries. *Journal of Computational Physics* 2006; **215**(1): 12-40.

Yang, V. and Andersen, W. E. Liquid rocket engine combustion instability. AIAA, 1995.

Ye, T., Mittal, R., Udaykumar, H. S., andShyy, W. An accurate cartesian grid method for viscous incompressible flows with complex immersed boundaries. *Journal of Computational Physics* 1999; **156**(2): 209-240.

Ye, T., Shyy, W., Tai, C.-F., andChung, J. N. Assessment of sharp- and continuous-interface methods for drop in static equilibrium. *Computers & Fluids* 2004; **33**(7): 917-926.